

# Analysis of Selected Models for Inelastic Electron Scattering in the KATRIN Gaseous Tritium Source

Master's thesis of

Fabian Leven

at the Institute of Experimental Particle Physics (ETP)  
of the Department of Physics  
at the Karlsruhe Institute of Technology

Reviewer: Prof. Dr. G. Drexlin  
Institute of Experimental Particle Physics, KIT  
Second Reviewer: Dr. K. Valerius  
Institute for Nuclear Physics, KIT  
Advisor: M. Sc. M. Machatschek  
Institute of Experimental Particle Physics, KIT

July 15th, 2018 – July 14th, 2019



# **Erklärung der Selbstständigkeit**

Ich versichere, dass ich diese Arbeit selbstständig verfasst habe und keine anderen als die angegebenen Quellen und Hilfsmittel benutzt habe, die wörtlich oder inhaltlich übernommenen Stellen als solche kenntlich gemacht und die Satzung des KIT zur Sicherung guter wissenschaftlicher Praxis in der gültigen Fassung vom 24.05.2018 beachtet habe.

Karlsruhe, den 14.07.2019, \_\_\_\_\_  
Fabian Leven

Als Prüfungsexemplar genehmigt von

Karlsruhe, den 14.07.2019, \_\_\_\_\_  
Prof. Dr. G. Drexlin



# Introduction

To our current knowledge, neutrinos are at the same time the most elusive and most abundant massive particles in the Universe. Their detection is challenging and pushes experiments at the edge of technical frontiers. Yet, their understanding might shed light on long-standing open questions of modern physics: What is dark matter? Do Majorana particles exist? Why does matter predominate over antimatter? What happened in the earliest stages of our Universe just after the Big Bang? And in all these regards, the yet unknown mass of neutrinos is a key physics parameter.

The KArlsruhe TRItium Neutrino (KATRIN) experiment aims to measure the effective mass of the electron antineutrino with an unprecedented sensitivity of 200 meV (90 % C.L.) based on tritium- $\beta$  decay. In order to provide this outstanding sensitivity KATRIN features i. a. a gaseous tritium source. Its special characteristics must be well controlled and understood. This thesis focuses on selected effects stemming from electrons scattering in said gaseous source. The effects were included in a high level analysis, meaning their impact on KATRIN's neutrino mass sensitivity was studied where possible.

## Outline

**[Do not forget to update this.]** Chapter 1 is a brief introduction to neutrino physics **ToDo** with special emphasis on the neutrino mass.

Chapter 2 focuses on the setup of the KATRIN experiment.

Chapter 3 introduces a mathematical model of a KATRIN neutrino mass measurement that can be used in parameter inference.

Chapter 4 integrates the mathematical model into a statistical framework for a high level analysis, especially for neutrino mass inference.

Chapter ?? investigates a refinement of the mathematical model with regard to electrons scattering off gas molecules within KATRIN's gaseous source. In particulars, the dependence of the inelastic scattering cross section on the energy of the incident electrons is studied.

Chapter 6 focuses on a preliminary model for the energy loss of electrons scattering inelastically off deuterium molecules. The model was established by a dedicated subgroup of the KATRIN collaboration based on KARIN data from October 2018. Its relation to KATRIN's sensitivity on the neutrino mass is investigated.

Chapter 7 summarizes the results, draws conclusions and offers an outlook.



# Contents

<b>Introduction</b>	<b>v</b>
<b>List of Figures</b>	<b>xi</b>
<b>List of Tables</b>	<b>xiii</b>
<b>1. Neutrino Physics</b>	<b>1</b>
1.1. Neutrinos until the 1960s . . . . .	1
1.2. Neutrinos in the Standard Model of Particle Physics . . . . .	2
1.2.1. General Particle Properties . . . . .	3
1.2.2. Neutrino Properties . . . . .	3
1.3. Mechanisms to generate Neutrino Masses . . . . .	3
1.3.1. Neutrino Mass Terms . . . . .	4
1.3.2. Neutrino Mixing . . . . .	5
1.4. Neutrino Oscillations . . . . .	5
1.4.1. Relation to Neutrino Masses . . . . .	6
1.4.2. Experimental Considerations . . . . .	7
1.4.3. Experimental Case Study: The Solar Neutrino Problem . . . . .	7
1.4.4. Summary of Experimental Results . . . . .	8
1.5. Absolute Neutrino Mass Measurements . . . . .	8
1.5.1. Observational Cosmology . . . . .	8
1.5.2. Search for Neutrinoless Double- $\beta$ Decay . . . . .	10
1.5.3. Kinematic Measurements of Weak Decays . . . . .	10
<b>2. The KATRIN Experiment</b>	<b>13</b>
2.1. Overview . . . . .	13
2.2. Windowless Gaseous Tritium Source . . . . .	14
2.3. Rear Section . . . . .	15
2.4. Differential Pumping Section . . . . .	16
2.5. Cryogenic Pumping Section . . . . .	16
2.6. Pre and Main Spectrometer . . . . .	18
2.6.1. MAC-E-filter principle . . . . .	18
2.6.2. Background Mitigation Strategies . . . . .	21
2.7. Detector Section . . . . .	21
<b>3. Mathematical Formalism of a KATRIN Measurement</b>	<b>23</b>
3.1. Differential Tritium- $\beta$ -Decay Spectrum . . . . .	23
3.2. Response Function . . . . .	25
3.2.1. Concepts and Nomenclature . . . . .	25
3.2.2. Gas Dynamics . . . . .	26
3.2.3. Transmission Function . . . . .	27
3.2.4. Probability of Electron Scattering within the WGTS . . . . .	28
3.2.5. Energy Loss of Electrons due to Scattering . . . . .	29

3.2.6. Assembly of the KATRIN Response Function . . . . .	30
3.3. Integral Rate . . . . .	32
3.4. Detector Counts . . . . .	33
3.5. Model Amendments . . . . .	33
3.6. Measurement Time Distribution . . . . .	33
3.7. A Simulated KATRIN Neutrino Mass Measurement . . . . .	34
<b>4. Statistical Methods and Neutrino Mass Inference at KATRIN</b>	<b>37</b>
4.1. Maximum Likelihood Estimation . . . . .	37
4.2. The Likelihood of a KATRIN Measurement . . . . .	37
4.3. A Nominal KATRIN Neutrino-Mass Fit . . . . .	38
4.4. Uncertainty Intervals . . . . .	38
4.4.1. Bayesian Credible Intervals . . . . .	38
4.4.2. Frequentist Confidence Intervals . . . . .	38
4.5. The KaFit and SSC Software Frameworks . . . . .	39
4.6. KATRIN's Sensitivity to the Electron Antineutrino Mass . . . . .	40
4.6.1. Definition and Construction of KATRIN's Sensitivity . . . . .	40
4.6.2. Sensitivity from Simulated Ensembles . . . . .	41
4.6.3. Sensitivity from the Profile-Likelihood Method . . . . .	41
<b>5. Energy-Dependence of the Cross Section for Inelastic Electron Scattering within the WGTS</b>	<b>43</b>
5.1. Cross Section for Electrons Scattering off Molecules of Hydrogen Isotopologues . . . . .	43
5.1.1. Theoretical Formulae . . . . .	44
5.1.2. Relation to Former Works . . . . .	44
5.2. An Energy-Dependent Scattering Model within the KATRIN Formalism . . . . .	45
5.2.1. Model Description . . . . .	46
5.2.2. Model Discussion . . . . .	47
5.3. Effect on the Inferred Neutrino Mass . . . . .	50
5.4. Conclusion and Outlook . . . . .	54
<b>6. Sensitivity Study using an Empirical Energy Loss Model Derived from KATRIN Data for Electrons Scattering Inelastically off Deuterium</b>	<b>55</b>
6.1. Motivation and Introduction . . . . .	55
6.2. The Empirical KATRIN Energy Loss Model . . . . .	56
6.2.1. Description . . . . .	56
6.2.2. Parametrization . . . . .	56
6.2.3. Nuisance Parameters . . . . .	57
6.3. Scope of the Presented Analysis . . . . .	57
6.4. Statistical Prerequisites . . . . .	60
6.4.1. Combination of a Calibration and a Neutrino Mass Measurements . . . . .	60
6.4.2. Nuisance Parameters and the Profile-Likelihood Method . . . . .	61
6.4.3. Ensemble Tests in Relation to an Asimov Data Set in Sensitivity Studies . . . . .	63
6.5. Results . . . . .	63
6.5.1. Sensitivity from an Asimov Data Set . . . . .	64
6.5.2. Cross-Check and Extension of the Asimov Data Set via Ensemble Testing . . . . .	65
6.6. Conclusion and Outlook . . . . .	69
<b>7. Conclusions and Outlook</b>	<b>71</b>

<b>Appendix</b>	<b>73</b>
A. Energy-Dependent Model of the Probability for Electron Scattering within the windowless gaseous tritium source (WGTS) . . . . .	73
A.1. Modeling . . . . .	73
A.2. Numerical Evaluation and Cross-Check . . . . .	74
B. Documentation of KaFit-Likelihood Extensions . . . . .	77
C. Parameter Values of the Preliminary KATRIN Energy Loss Model . . . . .	78
D. Configuration of the Sensitivity Study using the Empirical KATRIN Energy Loss Model . . . . .	79
<b>Bibliography</b>	<b>83</b>
Published . . . . .	83
Preliminary . . . . .	90
Software . . . . .	90



# List of Figures

1.1.	The Standard Model of Particle Physics . . . . .	4
1.2.	Neutrino mixing parameters and mass ordering . . . . .	9
1.3.	Feynman graph of neutrinoless double-beta decay . . . . .	11
2.1.	KATRIN beamline . . . . .	14
2.2.	KATRIN windowless gaseous tritium source (WGTS) . . . . .	15
2.3.	KATRIN rear section (RS) . . . . .	16
2.4.	KATRIN differential pumping section (DPS) . . . . .	17
2.5.	KATRIN cryogenic pumping section (CPS) . . . . .	18
2.6.	Scheme of the KATRIN main spectrometer and the MAC-E filter principle. . . . .	19
2.7.	KATRIN detector section . . . . .	22
3.1.	Tritium- $\beta$ spectrum for a vanishing and non-vanishing neutrino mass . . . . .	24
3.2.	The KATRIN transmission function . . . . .	27
3.3.	The energy loss probability density due to electron scattering in the WGTS	29
3.4.	The KATRIN response function . . . . .	32
3.5.	Simulated KATRIN measurement for a non-vanishing neutrino mass. . . . .	35
4.1.	Illustration of KATRIN's sensitivity to the neutrino mass . . . . .	40
5.1.	Inelastic cross section for non-relativistic incident electrons scattering off molecular hydrogen isotopologues . . . . .	45
5.2.	Energy-dependent probabilities for electron scattering within the WGTS . .	49
5.3.	Shift of an inferred squared neutrino mass induced by a neglected energy-dependence of the inelastic scattering cross section . . . . .	51
5.4.	Shift of an inferred squared neutrino mass induced by a neglected offset of the inelastic scattering cross section . . . . .	52
5.5.	Simulated integral $\beta$ -electron rate using different models of the cross section for inelastic electron scattering . . . . .	53
6.1.	The preliminary KATRIN energy loss model for electrons scattering off deuterium molecules . . . . .	59

6.2. Illustration of the profile-likelihood method . . . . .	62
6.3. Profile-likelihood ratio from an Asimov data set . . . . .	64
6.4. Test of coverage for the ensemble of confidence intervals obtained in the sensitivity study using the KATRIN energy loss model . . . . .	67
6.5. Chis-square distribution for the simulated ensemble of neutrino mass measurements obtained in the sensitivity study using the KATRIN energy loss model . . . . .	68
A.1. Numerical accuracy of the extended model for the probability of electron scattering within the WGTS . . . . .	76

# List of Tables

1.1.	Neutrino source classes for neutrino oscillation experiments . . . . .	7
1.2.	Overview of neutrino oscillation parameters . . . . .	10
1.3.	Constraining the neutrino mass by double- $\beta$ decay experiments . . . . .	10
1.4.	Neutrino mass constraints from kinematic measurements . . . . .	11
3.1.	Probability for electron scattering within the WGTS averaged over starting positions and pitch angles . . . . .	29
4.1.	KATRIN's sensitivity to the neutrino mass from ensemble tests . . . . .	41
5.1.	Probabilities for severalfold scattering of electrons in the WGTS . . . . .	46
6.1.	Confidence intervals and sensitivities obtained from an Asimov data set . .	65



# 1. Neutrino Physics

This chapter is an introduction to neutrino physics. The primary aim is to give an experimentally-rooted definition of a neutrino. Therefore, in section 1.1 selected experimental milestones are outlined that led to today’s description of a neutrino within the established Standard Model of Particle Physics (SM). In section 1.2 follows an outline of the SM and how it relates to the neutrino. Special attention is paid to the neutrino mass: First, in section 1.3, an extension of the SM that allows for neutrino masses is summarized. Second, in section 1.4, the phenomenon of neutrino flavor oscillations is introduced. Corresponding experiments proved that neutrinos have mass. Third, in section 1.5, experiments for an absolute neutrino mass measurement are presented because as such they relate particularly to the KATRIN experiment.

## 1.1. Neutrinos until the 1960s

Albeit the neutrino as a hypothetical new particle was not postulated until 1930, its rich scientific history might be seen as already heralded during the preceding 35 years.

In 1895, Becquerel reported results on experiments with phosphorescent substances, especially uranium salts, on photographic plates [Bec95]. These experiments mark the discovery of radioactivity and triggered manifold subsequent investigations.

In 1899, Rutherford published a classification of radioactive decays into  $\alpha$  and  $\beta$  types according to their penetration strength [Rut99].

In 1900, Becquerel determined the mass-charge ratio of  $\beta$ -decay particles [Bec00] and identified them as the electron previously described by Thomson [Tho97].

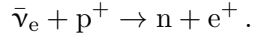
In 1914, Chadwick measured a continuous electron energy spectrum in the  $\beta$  decay of lead-214 and bismuth-214 [Cha14].

In 1927, Ellis and Wooster conducted a calorimetric measurement of the  $\beta$ -decay energy of radium and demonstrated that the continuity of the  $\beta$  spectrum was intrinsic to the decay as opposed to be caused by secondary effects [EW27].

In 1930, a  $\beta$  decay was thought of as a two-body decay  ${}^zA \rightarrow {}^{z+1}B + e^-$ . Assuming conservation of energy and momentum, in a two-body-decay the momenta of the daughter particles B and  $e^-$  are solely determined by their masses and the “energy content”, as Bohr put it, of the parent particle A. According to Bohr, there was no reason to believe that different nuclei of the same element A should have a different energy content in a  $\beta$  decay. Hence, the continuous nature of the  $\beta$  spectrum could not be explained [Boh32]. As a possible solution Pauli suggested the  $\beta$  decay to be a three-body decay and postulated an electrically neutral particle that carries part of the decay energy [Pau30].

In 1934, Fermi developed a quantitative theory of  $\beta$  decay that could describe the preceding experimental results [Fer34]. It comprises a four-fermion contact interaction respectively, a

three-body-decay model. It was the first description of the so-called “weak interaction”. Furthermore, Fermi coined the term “neutrino” for the particle postulated by Pauli. Fermi’s theory inspired the idea to use the so-called “inverse  $\beta$  decay” or “neutrino capture” to detect neutrinos, which in today’s nomenclature is written as



In 1956, Cowan and Reines published results of a corresponding experiment. It was conducted using the high neutrino flux of the nuclear reactor of the Savannah River Plant. The neutrinos originating in the reactor passed a tank of water and cadmium chloride triggering the above process. The emerging neutron was captured by the cadmium which emitted a photon in a 3 MeV to 11 MeV range



The emerging positron annihilated with an electron which produced two photons of 0.5 MeV each. A coincidence measurement of the corresponding photons enabled discriminating signal and background events. Based on their results Cowan and Reines reported the discovery of the free neutrino [Cow+56].

In the same year, 1956, Lee and Yang published an article on parity conservation. Parity conservation implies that a mirrored physical process behaves the same as its non-mirrored counterpart. Here, mirroring means a change of sign of the position vector in the applied physical laws. Lee and Yang pointed out that parity conservation might be violated in weak interactions and suggested several probing methods [LY56].

In 1957 Wu et al. conducted an experiment which employed one of the corresponding probing methods based on  $\beta$  decay. The parity operation respectively “the mirroring” corresponded a change of the magnetic field orientation in the experiment. The results showed that parity is violated in weak interactions [Wu+57].

In 1958, Goldhaber et al. measured the helicity  $H$  of the neutrino. Helicity is defined as  $H = \hat{\sigma} \cdot \hat{p}$ , where  $\hat{\sigma}$  is the spin unit vector and  $\hat{p}$  is the momentum unit vector (here: of the neutrino). The experiment found  $H = -1$  which corresponds to maximum parity violation. In other words, only left-handed neutrinos and right-handed antineutrinos participate in weak interactions [Gol+58].

In 1962, Danby et al. reported on a second type of neutrinos. A beam of pions generated at the Alternating Gradient Synchrotron in Brookhaven decayed according to  $\pi^\pm \rightarrow \mu^\pm + \bar{\nu}$ . The emerging neutrinos penetrated a 13.5-meter iron shield wall and their interactions were detected in a 10-t aluminum spark chamber. The observed interactions were path-like as opposed to shower-like, which implied the production of muons as opposed to electrons. This was marked as the discovery of the muon neutrino [Dan+62].

The attempts to uniformly describe the manifold discoveries in the field of particle physics in a combined theory converged over the course of the second half of the 20th century into what is known today as the Standard Model of Particle Physics.

## 1.2. Neutrinos in the Standard Model of Particle Physics

This section introduces the basic concepts of the Standard Model of Particle Physics (SM) in a condensed manner. It aims at giving a description of relevant particle properties in section 1.2.1 and relating them to neutrinos in section 1.2.2.

The SM is a gauge quantum field theory exhibiting the gauge symmetry  $SU(3) \times SU(2) \times U(1)$ . As such it can be formulated using the principle of least action and a Lagrangian density

$\mathcal{L}$  depending on fields and their derivatives [Zee03]. Albeit it can not account for all known subatomic phenomena, within its known boundaries, the SM is a well-tested and established theory, which is evident by e.g. the extensive review of particle properties of the Particle Data Group [Tan+18].

### 1.2.1. General Particle Properties

The gap between fields and particles can be bridged as follows: If “[i]n region 1 in spacetime there exists a source that sends out a ‘disturbance in the field’, which is later absorbed by a sink in region 2 in spacetime[,] experimentalists choose to call this a particle” [Zee03]. Intrinsic particle properties can be derived from the relation of their associated fields to the Lagrangian density. E.g., a particle’s mass is encoded by the Yukawa coupling of its field to the higgs doublet through the higgs mechanism and spontaneous symmetry breaking [Hig64]. A further intrinsic property is a particle’s spin, that takes half-integer values in units of  $\hbar$  for fermions or integer values for bosons. A particle’s flavor is its eigenstate with respect to the weak interaction, which is described by the  $SU(2) \times U(1)$  subgroup (Glashow-Weinberg-Salam model [Gla61; Wei67; Sal68]). According to Noether’s theorem, each symmetry conserves an associated charge [Noe18]. In the case of the  $SU(2) \times U(1)$  symmetry, the associated charges are called isospin  $\mathbf{T} = (T_1, T_2, T_3)^\top$  and hypercharge  $Y$ . A derivative of these charges is the electric charge  $Q = T_3 + \frac{1}{2}Y$  [Sch19]. In that sense, each particle has an associated antiparticle that carries the opposite electric charge. As mentioned in the historical overview (section 1.1), a theory consistent with experiment must violate parity. Such theories are called chiral [Zee03]. The SM is a chiral theory and thus its fermion fields can be decomposed in left- and right handed components [Sch19].

Figure 1.1 depicts the particles of the SM along with their selected properties mass and electric charge. It also shows a further categorization among the fermions into quarks and leptons.

### 1.2.2. Neutrino Properties

With reference to the particle properties listed in the previous section 1.2.1, a neutrino can be described as follows: A neutrino carries a spin of  $1/2\hbar$ . Thus, it is a fermion. It is categorized as a lepton. It has an electric charge of 0. And there are only left-handed neutrinos and right-handed antineutrinos [Sch19].

The mass of a neutrino will be discussed separately within the following chapters.

Neutrino come in three flavors, typically denoted as  $\nu_e$ ,  $\nu_\mu$  and  $\nu_\tau$ . Some additional remarks about the neutrino flavors can be made: First, the historical overview (section 1.1) mentions the discovery of the electron and muon flavor, but it was not until 2001 that the tau neutrino was discovered by the DONUT collaboration [Kod+01]. Second, a precision measurement of the width of the  $Z^0$ -boson resonance  $\Gamma_Z = (2.68 \pm 0.15) \text{ GeV}$  at the Large Electron Positron Collider (LEP) in the 1990s yielded a number of active light neutrino flavors consistent with three. In this context, “light” refers to a neutrino mass smaller than half the mass  $M_Z = (91.174 \pm 0.070) \text{ GeV}$  of the  $Z^0$ -boson [Acc+98]. (It should be noted that this refers to active neutrino flavors. Sterile neutrinos as an extension of the SM are not ruled out [OW08].)

## 1.3. Mechanisms to generate Neutrino Masses

Section 1.4 lists experiments which proof that neutrinos have mass. However, in the SM as described in section 1.2 the neutrino masses are assumed to be zero. Nevertheless, an extension of the SM is possible. The corresponding mass terms are introduced in section 1.3.1. The neutrino-mass formalism entails neutrino flavor mixing as described in section 1.3.2.

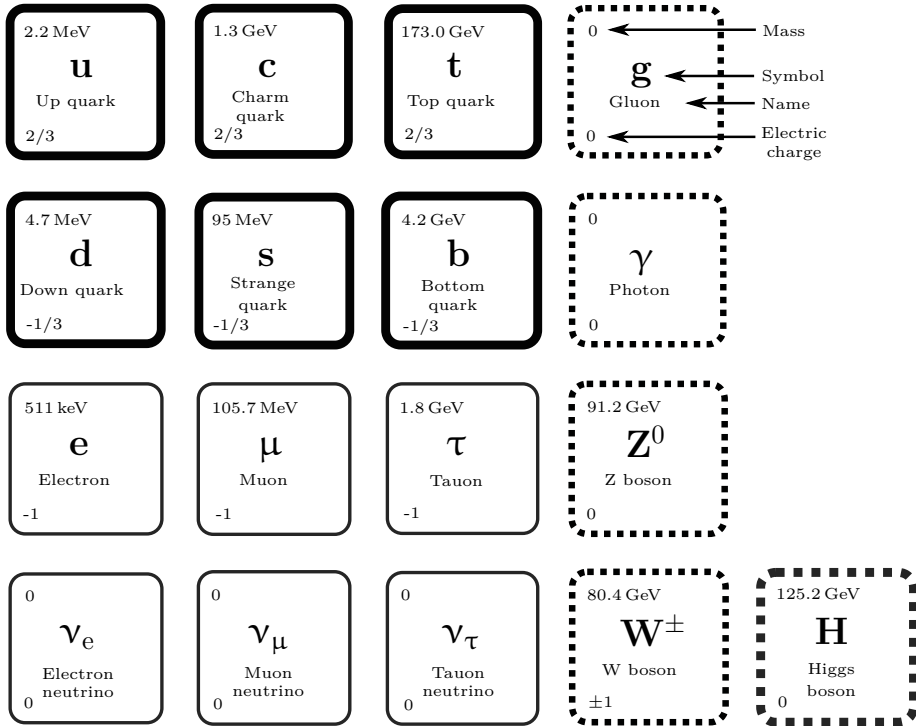


**Figure 1.1.: The Standard Model of Particle Physics.** The diagram illustrates possible categorizations of particles within the SM. The fermions are framed with continuous and the bosons with dotted lines. Among the fermions the quark sector is marked by a thick frame and the lepton sector by a thin one. The first three columns show the fermions; and the fourth and the fifth the bosons. While the bosons in the fourth column carry a spin of 1, the higgs boson in the fifth column marked with a thicker frame carries a spin of 0. Also shown are the particle masses in natural units and their electric charge in units of the absolute electron charge. All quantities along with uncertainties can be found in the Review of Particle Physics [Tan+18]. (Illustration adapted from [Sei19].)

### 1.3.1. Neutrino Mass Terms

For a theory to account for neutrino masses, its Lagrangian density must exhibit corresponding mass terms. According to [Zub11] the formalism can be summarized: The form of a mass term is given by the Dirac equation, which is produced by applying the principle of least action to a suitable Lagrangian density  $\mathcal{L}$ . The mass terms have to be quadratic in the fermion fields  $\psi$  and must leave the Lagrangian density hermitian. Furthermore, a field  $\psi$  must have a left- and right-handed component in order for the mass terms not to vanish. Two possible term forms are named after Dirac and Majorana. Whether one or a mixture of both forms corresponds to the neutrino's reality is an open question.

#### Dirac Masses

A Dirac mass term with mass  $m_D$  split in its chiral components (Weyl spinors)  $\psi_{L,R}$  has the form [Zub11]

$$\mathcal{L}_D = -m_D \bar{\psi} \psi = -m_D (\bar{\psi}_L \psi_R + \bar{\psi}_R \psi_L) . \quad (1.1)$$

Applying this to neutrinos requires both a left- and a right-handed Dirac neutrino. Right-handed neutrinos have not yet been observed. If they exist, they do not interact weakly and hence are called sterile.

## Majorana Masses

For Majorana mass terms the CP-conjugate  $\psi^C$  of a fermion spinor  $\psi$  is used. It should be noted that if  $\psi$  is left-handed,  $\psi^C$  is right-handed and vice versa. Then, a Majorana field  $\phi$  can be defined and a corresponding mass term  $\mathcal{L}_M$  with a mass  $m_M$  be constructed [Zub11]:

$$\phi = \psi + \psi^C \quad \mathcal{L}_M = -\frac{1}{2}m_M\bar{\phi}\phi. \quad (1.2)$$

As  $\phi^C = \phi$ , the described Majorana particle is its own antiparticle, which due to charge conservation is only possible for neutral particles, such as a neutrino.

### 1.3.2. Neutrino Mixing

If neutrinos have mass, their mass eigenstates  $|\nu_i\rangle$  ( $i \in \{1, 2, 3\}$ ) of the free Hamiltonian need not be identical to their flavor eigenstates  $|\nu_\alpha\rangle$  ( $\alpha \in \{e, \mu, \tau\}$ ) of the weak interaction [Zub11]. In case they differ, there must be a basis-change matrix. Such a matrix was introduced by Maki, Nakagawa and Sakata in order to explain the so-called neutrino oscillations (see section 1.4) predicted by Pontecorvo [Pon58; MNS62]. Therefore, the matrix  $U$  for a basis change is called Pontecorvo-Maki-Nakagawa-Sakata matrix (PMNS matrix)

$$|\nu_\alpha\rangle = \sum_i U_{\alpha i} |\nu_i\rangle. \quad (1.3)$$

As a complex unitary matrix  $U$  can be expressed by six parameters. A possible choice are three angles  $\theta_{12}, \theta_{23}, \theta_{13} \in [0, 2\pi)$ , a phase  $\delta \in [0, 2\pi)$  and two Majorana phases  $\alpha, \beta \in [0, 2\pi)$ :

$$U = \begin{pmatrix} 1 & 0 & 0 \\ 0 & \cos \theta_{23} & \sin \theta_{23} \\ 0 & -\sin \theta_{23} & \cos \theta_{23} \end{pmatrix} \begin{pmatrix} \cos \theta_{13} & 0 & \sin \theta_{13} e^{-i\delta} \\ 0 & 1 & 0 \\ -\sin \theta_{13} e^{i\delta} & 0 & \cos \theta_{13} \end{pmatrix} \begin{pmatrix} \cos \theta_{12} & \sin \theta_{12} & 0 \\ -\sin \theta_{12} & \cos \theta_{12} & 0 \\ 0 & 0 & 1 \end{pmatrix} \begin{pmatrix} 1 & 0 & 0 \\ 0 & e^{i\alpha} & 0 \\ 0 & 0 & e^{i\beta} \end{pmatrix}. \quad (1.4)$$

These parameters are called neutrino mixing parameters. It should be noted that  $\delta$  is also called “CP-violating” phase. Here,  $P$  stands for parity conjugation as it was explained in section 1.1; and  $C$  for electric charge conjugation that follows the same idea with a sign change of the electric charge instead of the position vector. Why  $\delta \neq 0$  implies  $CP$ -violation is shown in section 1.4.1.

One of the consequences of neutrino mixing, namely neutrino oscillations, will be explained in the following section 1.4.

## 1.4. Neutrino Oscillations

The term “neutrino oscillations” refers to the neutrino’s change of flavor after passing a certain propagation distance. In other words, neutrinos might be detected in another flavor than the one they originated in. Section 1.4.1 introduces a demonstrative formalism that aims at showing the link between oscillations and the masses of neutrinos. Neutrino oscillations also depend on the neutrino mixing parameters introduced in section 1.3.2. The accessibility of these mixing parameters and neutrino masses via neutrino oscillation experiments will be evaluated in section 1.4.4. Neutrino oscillation experiments are manifold. As an exemplary case study the so-called “solar neutrino problem” is discussed in section 1.4.3. Finally, the experimental results on neutrino oscillations will be summarized in section 1.4.4.

### 1.4.1. Relation to Neutrino Masses

According to [Zub11] a formula demonstrating neutrino oscillations can be derived: Using the PMNS matrix  $U$  from equation (1.4) the evolution of a neutrino's flavor eigenstate on a one-dimensional path starting at position  $x = 0$  at time  $t = 0$  with momentum  $p_i$  and energy  $E_i$  of its mass eigenstates  $|\nu_i\rangle$  is

$$|\nu_\alpha(x, t)\rangle = \sum_i U_{\alpha i} e^{-i(E_i t - p_i x)} |\nu_i\rangle. \quad (1.5)$$

This leads to the transition amplitudes

$$A(\alpha \rightarrow \beta)(t) = \langle \nu_\beta | \nu_\alpha(x) \rangle = \sum_i U_{\beta i}^* U_{\alpha i} e^{-i(E_i t - p_i x)t} \quad (1.6a)$$

$$A(\bar{\alpha} \rightarrow \bar{\beta})(t) = \langle \bar{\nu}_\beta | \bar{\nu}_\alpha(x) \rangle = \sum_i U_{\beta i} U_{\alpha i}^* e^{-i(E_i t - p_i x)t}. \quad (1.6b)$$

It should be noted that if  $U \neq U^*$ , equation (1.6) implies  $CP$ -violation. In reference to section 1.3.1 it holds  $U \neq U^* \Leftrightarrow \delta \neq 0$ , justifying that  $\delta$  is called  $CP$ -violating phase.

The following assumptions allow for a simple and demonstrative form of the transition probability:

- The neutrinos are relativistic:
  - Their momentum equals approximately their energy which is by far larger than their mass  $p_i \approx E_i \gg m_i$ . This also implies that the energy can be expanded in the mass-momentum-ratio  $m_i/p_i$ .
  - They travel the distance  $x = L = ct$  at the speed of light  $c$ .
- All neutrino generations have approximately the same momentum  $E \approx p \approx p_i$ .
- The  $CP$ -violating phase vanishes:  $\delta = 0$ . (This assumption is not necessary, but simplifies the expression for the transition probability. See [Zub11] for  $\delta \neq 0$ .)

Then, the transition probability from one flavor  $\alpha$  to another  $\beta$  in dependence of the neutrino masses and mixing parameters is

$$\begin{aligned} P(\alpha \rightarrow \beta)(L) &= |\langle \nu_\beta | \nu_\alpha(L) \rangle|^2 \\ &= \delta_{\alpha\beta} - 4 \sum_i \sum_{j>i} U_{\alpha i} U_{\alpha j} U_{\beta i} U_{\beta j} \sin^2 \left( \frac{(m_i^2 - m_j^2)}{4} \frac{L}{E} \right). \end{aligned} \quad (1.7)$$

Equation (1.7) shows oscillatory behavior if two conditions are fulfilled. First, the mass eigenvalue of at least two mass eigenstates must differ. Second, the product of the corresponding PMNS matrix elements must not be zero. In other words, neutrino oscillations require at least one neutrino to have mass and to undergo flavor mixing. Furthermore, neutrino oscillation experiments are sensitive to the difference of squared masses

$$\Delta m_{ij}^2 = |m_i^2 - m_j^2|, \quad (1.8)$$

which only yields two independent observables for three masses. Thus, these experiments cannot be used to determine the absolute mass scale of neutrinos.

### 1.4.2. Experimental Considerations

According to equation (1.7), the ratio  $L/E$  determines the sensitivity of an experiment to the oscillation parameters given by the PMNS matrix  $U$  (mixing parameters) and  $\Delta m_{ij}^2$  (mass ordering).  $L$  can be tuned by placing the detector in a suitable distance from a Earth-based neutrino source.  $E$  can either be tuned by using e. g. particle accelerators as source or it varies naturally, for instance if the source exhibits an energy spectrum like e. g. the Sun.

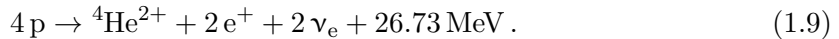
Furthermore, two detection channels can be distinguished. If, on one hand, an experiment is only sensitive to the neutrino flavor which is emitted by the neutrino source, it can detect a weakening of the neutrino flux. This is referred to as disappearance channel. If, on the other side, an experiment is sensitive to a different neutrino flavor than the one which the neutrino source emits, this is referred to as appearance channel [Zub11].

There are four major classes of neutrino sources that can be used to measure the mixing parameters and the mass ordering. They are listed in table 1.1. For each class multiple experiments exist [Zub11]. Not all experiments will be discussed here. Instead, the following section 1.4.3 discusses the so-called “Solar Neutrino Problem” as an exemplary case study on solar neutrino experiments.

### 1.4.3. Experimental Case Study: The Solar Neutrino Problem

The term “Solar Neutrino Problem” refers to the mismatch of the total neutrino flux arriving on Earth predicted by the standard solar model (SSM) and measured by, first, the Homestake and, later, other experiments. In this section the problem is briefly described and its resolution developed.

At the end of the 1930s, Bethe, von Weizsäcker and Critchfield showed that there are two main fusion cycles in the Sun, the so-called CNO and pp cycle. The latter is the primary source of solar neutrinos [Wei38; BC38; Bet39]. Its multi-step reaction can be summarized as [Zub11]



Its initial reaction and the one with the broadest neutrino energy spectrum (from below 0.1 to  $\sim 11$  MeV [Tan+18]) are



It should be noted that only electron neutrinos are produced in the Sun. Starting from the 1970s the solar electron neutrino flux was measured; the first time by the Homestake

**Table 1.1.: Neutrino source classes for neutrino oscillation experiments.** Listed are different neutrino source classes and which neutrino flavors they emit [Zub11]. Furthermore, the oscillation parameters they are mainly sensitive to are tabulated along with an example experiment.

source class	flavors	sensitive to	example experiment
nuclear power plants	$\bar{\nu}_e$	$\sin \theta_{13}$	Double Chooz [Abe+16]
accelerators	$\nu_e, \nu_\mu, \bar{\nu}_e, \bar{\nu}_\mu$	$\sin \theta_{12}, \sin \theta_{23}, \Delta m_{12}^2, \Delta m_{23}^2$	MiniBooNE [Agu+09]
atmosphere	$\nu_e, \nu_\mu, \bar{\nu}_e, \bar{\nu}_\mu$	$\sin \theta_{23}, \Delta m_{23}^2$	Super-KamiokaNDE [Fuk+98]
the Sun	$\nu_e$	$\sin \theta_{12}, \Delta m_{21}^2$	SNO [Aha+13]

experiment using the inverse beta decay of  $^{37}\text{Cl}$ . It could detect electron neutrinos with an energy threshold of 813 keV. The measured flux was one third of the prediction by the SSM [Cle+98; BPB01]. This is marked as the beginning of the solar neutrino problem. The experiments GALLEX/GNO and SAGE confirmed the results, where the latter could detect electron neutrinos with an energy threshold of 233 keV [Kir98; Alt+05; Abd+09]. The low energy threshold is of importance because the neutrinos emitted by the initial reaction of the pp cycle, equation (1.10), exhibit the highest flux, but at the same time an energy spectrum that ends at approximately 400 keV [Bah96].

Starting from 1999 the SNO experiment measured the neutrino flux of all flavors. It used 1000 t of heavy water  $\text{D}_2\text{O}$  to detect electron neutrinos via charged currents as well as all flavors via neutral currents and elastic neutrino-electron scattering. In order to fully explain the flux data, the so-called Mikheyev-Smirnov-Wolfenstein effect (MSW effect) had to be respected [Wol78; MS86]: Electron neutrinos can undergo charged current interactions with surrounding electrons in a coherent forward scattering process, which alters the flavor transition amplitude. This effect is only significant in areas of high electron densities, such as the Sun. Taking these matter-mediated oscillations into account, the measured flux of all flavors of the  $^8\text{B}$  neutrinos, equation (1.10), was in accordance with the electron neutrino flux predicted by the SSM [Aha+13]. Thus, the solar neutrino problem was resolved after more than three decades.

#### 1.4.4. Summary of Experimental Results

This section summarizes the results obtained from neutrino oscillation experiments. The neutrino oscillation parameters consist of the squared neutrino mass differences, equation (1.8), and the mixing parameters of the PMNS matrix, equation (1.4). It should be noted first, that the MSW resonance of solar neutrinos requires  $m_1 < m_2$ , which still allows for two possible mass orderings [Zub11]:

1. normal ordering  $m_1 < m_2 < m_3$  and
2. inverted ordering  $m_3 < m_1 < m_2$ .

For these two cases a combination of recent experimental results for the neutrino oscillation parameters is given in table 1.2 and illustrated in figure 1.2. All in all, neutrino oscillations are experimentally verified and provide unequivocal that neutrinos have mass.

### 1.5. Absolute Neutrino Mass Measurements

The absolute masses of neutrinos remain unknown and, as shown in section 1.4.1, neutrino oscillations are only sensitive to squared mass differences. This section presents methods to probe the absolute neutrino mass. The corresponding measurements fall into one of three categories [OW08]:

- observational cosmology (section 1.5.1),
- search for neutrinoless double  $\beta$  decay (section 1.5.2) or
- kinematic measurements of weak decays such as  $\beta$  decay and electron capture (section 1.5.3).

#### 1.5.1. Observational Cosmology

In the early Universe, neutral particles such as light neutrinos could escape from areas of high mass density to areas of low mass density. As they carry away mass, the larger the neutrino mass, the stronger is the suppression of density fluctuations on small scales.

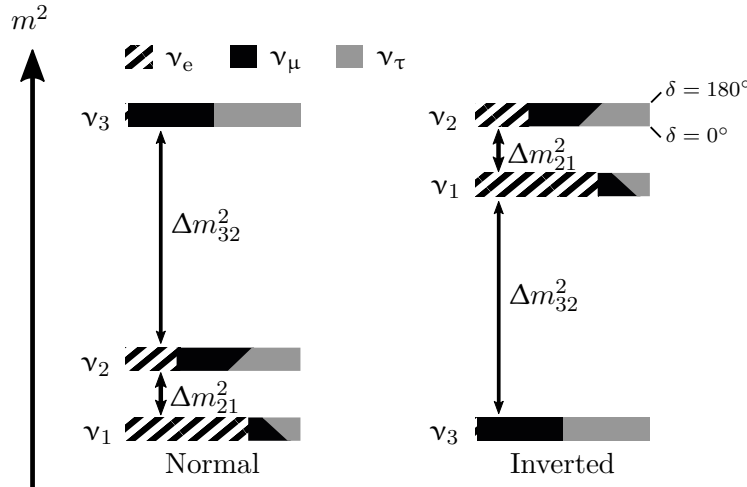


**Figure 1.2.: Neutrino mixing parameters and mass ordering.** The chart shows how the mass eigenstates  $\nu_i$  are composed of the flavor eigenstates  $\nu_\alpha$  in the normal and inverted mass ordering. The composition depends on the phase  $\delta$ . The mixing is shown for the two extreme cases  $\delta = 0^\circ$  (baseline) and  $\delta = 180^\circ$  (topline). (Adapted from [Sei19]. Numerical values can be found in [Est+19].)

In a mathematical formulation the power spectrum of the density contrast is examined and a higher neutrino mass would lead to a stronger suppression of small scale structures. Corresponding data are obtained, for example, by the Sloan Digital Sky Survey (SDSS). This survey records the sky's optical and infrared spectrum via telescope in order to map the large scale distribution of galaxies and galaxy clusters [Dor+04]. Furthermore, the temperature anisotropies in the cosmic microwave background (CMB) encode information on the Universe's structure. The latest and most precise data are recorded by the Planck satellite [Agh+18]. Under the assumption that all mass states contribute with the same number density cosmological observations are to first order only sensitive to the sum of all neutrino masses  $\sum_i m_i$ . A combination of the above data sets yields [Yèc+17]

$$\sum_i m_i < 0.14 \text{ eV} \quad (95\% \text{ C.L.}) .$$

**Table 1.2.: Overview of neutrino oscillation parameters.** The table lists the observables and their best fit values along with the  $1\sigma$ -uncertainty range for normal and inverted ordering. (From [Est+19].)

observable	normal ordering	inverted ordering
$\sin \theta_{13}$	$0.310^{+0.013}_{-0.012}$	$0.310^{+0.013}_{-0.012}$
$\sin \theta_{23}$	$0.580^{+0.017}_{-0.021}$	$0.584^{+0.016}_{-0.020}$
$\sin \theta_{13}$	$0.02241^{+0.00065}_{-0.00065}$	$0.02264^{+0.00066}_{-0.00066}$
$\delta / {}^\circ$	$215^{+40}_{-29}$	$248^{+27}_{-29}$
$\frac{\Delta m_{21}^2}{10^{-5} \text{ eV}^2}$	$7.39^{+0.21}_{-0.20}$	$7.39^{+0.21}_{-0.20}$
$\frac{\Delta m_{31}^2}{10^{-3} \text{ eV}^2}$	$+2.525^{+0.033}_{-0.032}$	
$\frac{\Delta m_{32}^2}{10^{-3} \text{ eV}^2}$		$-2.512^{+0.034}_{-0.032}$

### 1.5.2. Search for Neutrinoless Double- $\beta$ Decay

Double- $\beta$  decay ( $2\nu\beta\beta$ ) is described as a nucleus of element  $X(Z, A)$  with  $Z$  protons and  $A - Z$  neutrons that decays to a daughter isotope  $Y(Z + 2, A)$  via two simultaneous  $\beta$  decays

$$X(Z, A) \rightarrow Y(Z + 2, A) + 2e^- + 2\bar{\nu}_e. \quad (1.11)$$

If the neutrino is its own antiparticle, respectively of Majorana type, the neutrino emitted in the first decay can be absorbed in the second decay resulting in a neutrinoless double decay ( $0\nu\beta\beta$ ). This would require the neutrino to have mass. Such a decay would manifest itself in a peak in the  $\beta$  spectrum two neutrino masses above the endpoint of the continuum [Zub11]. It should be noted that this would violate lepton number conservation. The half-life of such a decay encodes the Majorana mass of the electron neutrino as a coherent sum of all neutrino masses using the PMNS matrix  $U$  from equation (1.4)

$$m_{\beta\beta}^2 = \left| \sum_i U_{ei}^2 m_i \right|^2. \quad (1.12)$$

As  $U$  contains two unknown Majorana phases partial cancellation might occur. Hence, it is difficult to compare  $m_{\beta\beta}$  to masses obtained by other methods. The two most stringent upper limits on  $m_{\beta\beta}$  are listed in table 1.3.

### 1.5.3. Kinematic Measurements of Weak Decays

Several laboratory experiments as well as the supernova event 1987A have provided upper limits of absolute neutrino masses from the analysis of kinematics of weak interactions involving neutrinos or neutrino time-of-flight considerations. Such experiments can not

**Table 1.3.: Constraining the neutrino mass by double- $\beta$  decay experiments.** Listed are the two most stringent limits on  $m_{\beta\beta}$ , equation 1.12, given as ranges.

experiment	isotope	90 % C.L. upper limit on $m_{\beta\beta}$ (eV)
GERDA [Ago+18]	$^{76}\text{Ge}$	0.12–0.26
KamLAND-Zen [Gan+16]	$^{136}\text{Xe}$	0.05–0.16



**Figure 1.3.: Feynman graph of neutrinoless double- $\beta$  decay.** The graph depicts the simultaneous transformation of two neutrons into two protons where the down quarks transform into up quarks, whilst two electrons and two neutrinos are produced. The two emitted neutrinos annihilate in a Majorana transition.

**Table 1.4.: Neutrino mass constraints from kinematic measurements.** The table lists upper limits on the absolute neutrino masses for different neutrino flavors.

flavor	measurement basis	upper limit	reference
$\nu_e$	neutrinos from Supernova 1987A	5.7 eV (95 % credible interval)	[LL02]
$\nu_\mu$	muon decay	17 keV (90 % C.L.)	[Ass+96]
$\nu_\tau$	tau decay	18.2 MeV (95 % C.L.)	[Bar+98]
$\bar{\nu}_e$	tritium- $\beta$ decay	2 eV (95 % C.L.)	[Kra+05; Ase+11; Tan+18]

resolve the mass splitting between the squared mass eigenvalues. Therefore, the corresponding observable is a weighted sum of the  $N$  neutrino eigenmasses where the weights are the elements of the PMNS matrix from equation (1.4) [OW08]

$$m_{\nu_\alpha}^2 = \sum_i^N |U_{\alpha i}|^2 m_i^2. \quad (1.13)$$

In the scope of this thesis, the measurement of the mass of the electron antineutrino via  $\beta^-$ -decay kinematics is of special interest. Hence, this subject is examined more closely within this section. For completeness, aside from the upper limit on the mass of the electron antineutrino, table 1.4 also lists upper limits for other neutrino flavors obtained by kinematic measurements.

### Neutrino Masses from $\beta$ -decay Kinematics

In  $\beta^-$  decay

$$X(Z, A) \rightarrow Y(Z + 1, A) + e^- + \bar{\nu}_e \quad (1.14)$$

part of the released surplus energy generates the neutrino's mass. This leaves a signature in the  $\beta$  spectrum. (Also see section 3.1.) In a neutrino mass experiment four criteria are important for a suitable  $\beta$  emitter [OW08]:

- The  $\beta$  emitter should have an energy spectrum with a relatively low endpoint, because in the uncertainty on the neutrino mass enter the input uncertainties of neutrino energy and momentum scaled up with the endpoint energy.
- The  $\beta$  emitter must have a sufficiently high activity to provide statistically relevant count rates for quantities that can be handled in the laboratory.
- The  $\beta$  decay should be super-allowed in order for the nuclear matrix element of the decay process to be energy independent.

- The  $\beta$ -emitter molecule should be as simple as possible to allow for a theoretical treatment of its decay kinematics such as the final state of the decay-daughter molecule.

Tritium is an ideal candidate with respect to these criteria [OW08]. The corresponding measurement principle will be explained more closely in the following chapters about the KATRIN experiment. However, KATRIN has several predecessor experiments. The most recent two experiments based on tritium- $\beta$  decay in Mainz and Troitsk obtained a combined upper limit on the electron antineutrino mass of [Kra+05; Ase+11; Tan+18]

$$m_{\bar{\nu}_e} < 2 \text{ eV} \quad (95\% \text{ C.L.}) .$$

It should be noted that KATRIN aims for a precision that is better by one order of magnitude.

## 2. The KATRIN Experiment

The Karlsruhe Tritium Neutrino (KATRIN) experiment performs a kinematic measurement of the tritium- $\beta$  spectrum in order to determine the effective mass of the electron antineutrino (from here forth labeled  $m_\nu$ ) as defined by equation (1.13). In case no neutrino mass signal is observed, KATRIN aims to set an upper limit of

$$m_\nu < 200 \text{ meV} \quad (90\% \text{ C.L.}),$$

which is one order of magnitude more constraining than the one set by its predecessor experiments. KATRIN recorded the first  $\beta$  spectrum in a commissioning run in May 2018 and started neutrino mass measurements in March 2019.

This chapter provides an overview of the KATRIN apparatus. However, given KATRIN's complexity, it can by no means be exhaustive and for a comprehensive treatment the reader is referred to the KATRIN Design Report [KAT05] supplemented by an up-to-date hardware overview that is in the making at the time of writing this thesis<sup>1</sup>.

### 2.1. Overview

The KATRIN experiment comprises a 70-m-long beam line depicted in figure 2.1. It can be divided into two sections:

1. The **source and transport section (STS)** comprises i. a. the gaseous tritium source where the tritium decays and the  $\beta$  electrons are magnetically guided along the beam line. Furthermore, the gas flow from the tritium source to the exit of the STS is reduced by at least 14 orders of magnitude.
2. In the **spectrometer and detector section (SDS)** the  $\beta$  electrons are filtered according to their kinetic energy and finally counted at the detector.

A central concept of the KATRIN setup is the magnetic flux tube. The  $\beta$  electrons must be guided from their point of origin to the detector. Therefore, a magnetic field is created by superconducting solenoids surrounding the beam line in the STS as well as coils around, and superconducting solenoids before and after the spectrometer tank in the SDS. The field lines are intersperse the beam line over the range of the whole experiment. The volume that is mapped onto the detector by this mechanism is called the flux tube. Within the flux tube, charged particles perform cyclotron motions around the field lines and are adiabatically guided from the STS to the detector. Adiabaticity is guaranteed by avoiding strongly varying field strengths on short distances.

A further central concept of KATRIN is the windowless source. As  $\beta$  electrons must not loose energy before energy analysis takes place, the SDS is windowlessly connected to the STS. However, the spectrometer must be kept practically free of any tritium flow

---

<sup>1</sup>K. Altenmüller et al. (KATRIN collaboration), in prep.

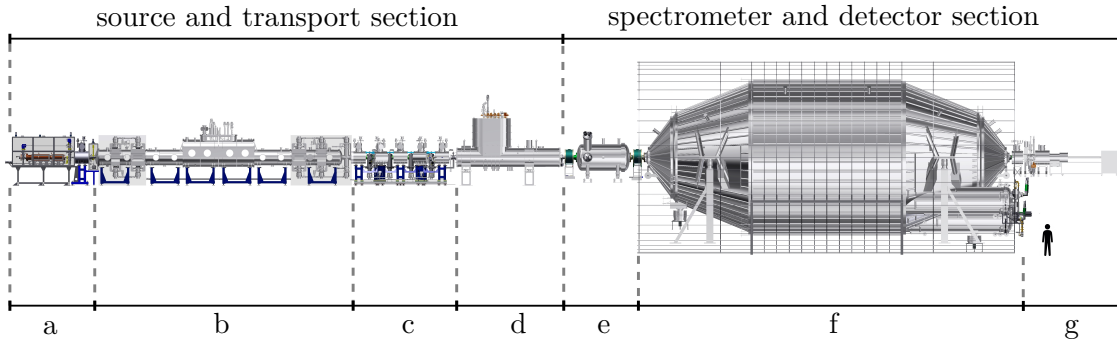


**Figure 2.1.: The KATRIN beamline.** Shown are the main hardware components:

- a) rear section (see section 2.3)
- b) windowless gaseous tritium source (WGTS) (see section 2.2)
- c) differential pumping section (DPS) (see section 2.4)
- d) cryogenic pumping section (CPS) (see section 2.5)
- e) pre spectrometer (see section 2.6)
- f) main spectrometer (see section 2.6)
- g) detector (see section 2.7)

for safety reasons and to keep the strict background requirements. Therefore, pumping systems reduce the gas inlet pressure of  $1.8 \text{ mbar}\ell/\text{s}$  to the tritium partial pressure of below  $10^{-14} \text{ mbar}\ell/\text{s}$  of the spectrometer.

The following sections step through the various components along the KATRIN beam line describing their functionality and purpose.

## 2.2. Windowless Gaseous Tritium Source

The WGTS is a 16-m-long, 1.5-m-wide and 4-m-high cryostat. It is depicted in figure 2.2 and a detailed description can e. g. be found in [Gro+08; Bab+12]. In the following the major features of the WGTS are reviewed:

**Tritium purity:** The molecular tritium ( $\text{T}_2$ ) is injected in the middle of the 10-m beam tube of 90 mm diameter, where it decays. The design gas column density is  $\rho d = 5 \times 10^{17} \text{ molecules}/\text{cm}^2$  with an isotropic tritium purity of  $\epsilon_T = 95\%$  [KAT05] or better. At the front and rear of the WGTS, the gas is extracted from the beam tube by turbo molecular pumps in designated differential pumping sections called DPS-1-R (rear) and DPS-1-F (front). The extracted gas is re-injected in the center of the beam tube. The respective circulation system is called the inner loop [PSB15]. The tritium purity  $\epsilon_T$  must be kept stable on a 0.1 % level [KAT05]. Therefore, a permeator is installed that separates impurities (like e. g. helium) and ejects them into the exhaust loop of the Tritium Laboratory Karlsruhe (TLK). Furthermore, the isotopic composition of the gas is monitored by a designated laser Raman system (LARA) [Sch13].

**Injection pressure:** The design injection pressure of the tritium gas is  $1.8 \text{ mbar}\ell/\text{s}$ . It must be kept stable at the 0.1 % level. This is achieved via a pressure- and temperature-controlled buffer vessel within the inner loop [PSB15].

**Magnetic field:** In order to adiabatically guide the  $\beta$  electrons to the spectrometer section the WGTS is pervaded by a magnetic field parallel to its beam tube axis of up to 5.6 T. It is created by 7 superconducting coils, that surround the beam tube. These magnets are kept at a temperature of 4.2 K by liquid helium [Are+18b].

**Temperature:** On the one hand, thermal motion smears the energy spectrum of the  $\beta$  electrons (Doppler effect). On the other hand, at low temperatures the gas molecules



**Figure 2.2.: The windowless gaseous tritium source (WGTS).** The hull and a sketch of the beam tube are shown. Indicated are the 8 turbo molecular pumps (TMP), the 7 magnets, the design temperatures for tritium operation, the maximum magnetic field strengths and a gradient within the beam tube depicting the decreasing gas density from the center to the sides. (Adapted from [Har15].)

start to cluster.  $T = 30\text{ K}$  is chosen as a compromise and established by a two-phase neon cooling system. For calibration purposes, it is also possible to operate the WGTS with krypton-83m instead of tritium. This requires a beam tube temperature of  $T = 100\text{ K}$  in order for the krypton not to freeze. In this operational mode the neon has to be exchanged for argon [KAT05].

### 2.3. Rear Section

The rear section (RS) terminates the beam line in the upstream direction and houses monitoring, calibration and control devices. It is depicted in figure 2.3 and a detailed description can e.g. be found in [Bab14]. In the following the major features of the RS are reviewed:

**Electron gun:** The RS houses an electron gun in order to measure the response function of the experiment (see section 3.2) via a electron source with a well-defined energy resolution of  $\sim 0.2\text{ eV}$  and angular resolution of  $\sim 4^\circ$ . The electrons are guided towards and through the rear wall by a designated electromagnetic guidance system. Furthermore, their flight path can be adjusted by dipole magnets mounted in the WGTS which enable a scanning of the full flux tube [Bab14].

**Rear wall and plasma control:** The so-called rear wall is a gold-coated stainless-steel disc with a diameter of 6 inches that terminates the beam tube. It has a hole in the center to let electrons from the electron gun pass through. Its main purpose is the control of plasma effects: Space charges, respectively a plasma, forms within the WGTS due to the tritium decay. Therefore,  $\beta$  electrons may start at different potentials which adds uncertainty to the measured  $\beta$  spectrum. Simulations show that the plasma can be influenced by the rear wall potential which can be controlled via a voltage supply in the range of  $\pm 10\text{ V}$ . Moreover, a UV light illumination of the rear wall can provide a large flux of electrons extracted via the photoelectric effect that can compensate space charges. Therefore, a homogeneous work function of the rear wall with fluctuations less than  $20\text{ meV}$  is required [Kuc+18; Kuc16].

**Activity monitoring:** A super conducting coil designed to create a magnetic field of  $4.7\text{ T}$  in the RS ensures that the magnetic flux tube terminates at the rear wall. Hence, per

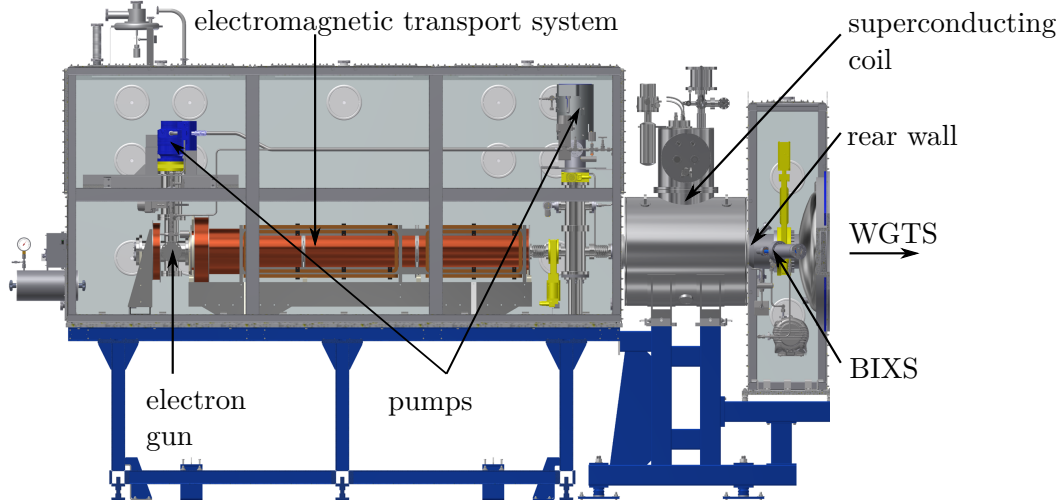


**Figure 2.3.: The rear section (RS)** terminates the KATRIN beam line and houses several monitoring and calibration devices that are described in the main text. (Adapted from [Sei19].)

design of the magnetic guidance,  $\beta$  electrons either arrive at the detector or hit the rear wall. On hitting the rear wall they emit bremsstrahlung. Two dedicated beta-induced X-ray spectroscopy (BIXS) systems measure the corresponding X-ray spectrum to determine the source strength respectively the gas column density [Röl15].

#### 2.4. Differential Pumping Section

The differential pumping section (DPS) is composed of five elements. It is depicted in figure 2.4 and a detailed description can e. g. be found in [Kos12]. For orientation, in this section, the elements are labeled 1 to 5 from WGTS to cryogenic pumping section (CPS). In the following the major features of the differential pumping section (DPS) are reviewed:

**Reduction of tritium flow:** The five beam tube elements of the differential pumping section (DPS) form a  $20^\circ$  angle to each other and are arranged in a chicane.  $\beta$  electrons are magnetically guided along the chicane by a magnetic field of up to 5.5 T created by five superconducting solenoids. By contrast, the neutral gas molecules scatter off the walls. This reduces the molecular beaming effect and enhances the pumping probability [ZJH12]. Four turbo molecular pumps mounted between the beam tube elements then reduce the gas flow by approximately five orders of magnitude and feed the gas into the so-called outer loop where it is reprocessed [Kos12].

**Ion blocking:** In the WGTS, ions such as  $\text{HeT}^+$ ,  $\text{T}_2^+$ ,  $\text{T}_3^+$ ,  $\text{T}_5^+$  can form. If not blocked, reach the spectrometer section together with the  $\beta$  electrons and are even accelerated by the retarding voltage (see section 2.6). This would eventually lead to an increased background rate. A potential barrier created by two ring electrodes in element 5 and the pump port between DPS and CPS set to +100 V avoids such a scenario. The positive ions are deflected, and dipole electrodes in the elements 1 to 4 make them drift out of the flux tube. They hit the wall and get neutralized [Klein19].

**Ion monitoring:** Downstream of the blocking electrodes the remaining ion flux is measured by a Fourier transform ion cyclotron resonance device (FT-ICR) [Ubi+09].

#### 2.5. Cryogenic Pumping Section

The cryogenic pumping section (CPS) is an approximately 7-m-long cryostat. It is depicted in figure 2.5 and a detailed description can e. g. be found in [Jan15]. For orientation, in



**Figure 2.4.: The differential pumping section (DPS)** reduces the gas flow by five orders of magnitude and blocks tritium ions. Its five elements, each with a separate magnet (M1-M5), and connected by pump ports, are shown. The outer loop connects the turbo molecular pumps to the infrastructure of the TLK. (Adapted from [Sei19].)

this section, its seven elements are labeled 1 to 7 from WGTS to CPS. In the following the major features of the CPS are reviewed:

**Reduction of tritium flow:** The CPS consists of seven beam tube elements of which the first five are arranged in a similar manner as the beam tube elements of the DPS, in a chicane forming 15° angles. Charged particles are guided along the chicane by a magnetic field of up to 5.6 T created by seven superconducting coils. Neutral molecules hit the walls that are covered by a frozen argon layer cooled down to 3 K in order to cold-trap particles. These low temperatures are achieved via a liquid helium cooling and a heat shield of liquid neon. After the accumulation of about 1 Ci of tritium the argon frost layer has to be renewed. In order to achieve this, the beam tube is warmed up and the argon is pumped off along with the accumulated tritium. Tests and simulations show a reduction of the tritium flow by approximately 10 orders of magnitude [Jan15; Röt19].

**The forward beam monitor (FBM):** The FBM can be moved horizontally into the pump port between beam tube element 6 and 7 of the CPS with a 2-dimensional spatial resolution of 0.1 mm. Two *pin*-diodes measure the β-electron flux and thus the stability of the gas column density in the WGTS. Furthermore, the forward beam monitor (FBM) equips a temperature and a hall sensor. A second detector board holding a Faraday cup for ion measurements is also available [Klein19]. More information about the FBM can e.g. be found in [Ell+17; Ell19].

**The condensed  $^{83m}\text{Kr}$  source (CKrS):** The condensed  $^{83m}\text{Kr}$  source (CKrS) is a sub mono-layer of  $^{83m}\text{Kr}$  on a pyrolytic graphite substrate with a diameter of 2 cm. It can be lowered in the pump port of the CPS and moved in a 2-dimensional plane perpendicular to the beam line. This enables the spatial scanning of the properties of the spectrometer using quasi-monoenergetic conversion electron lines of  $^{83m}\text{Kr}$  [Bau14; Dyb19; Are+18a].

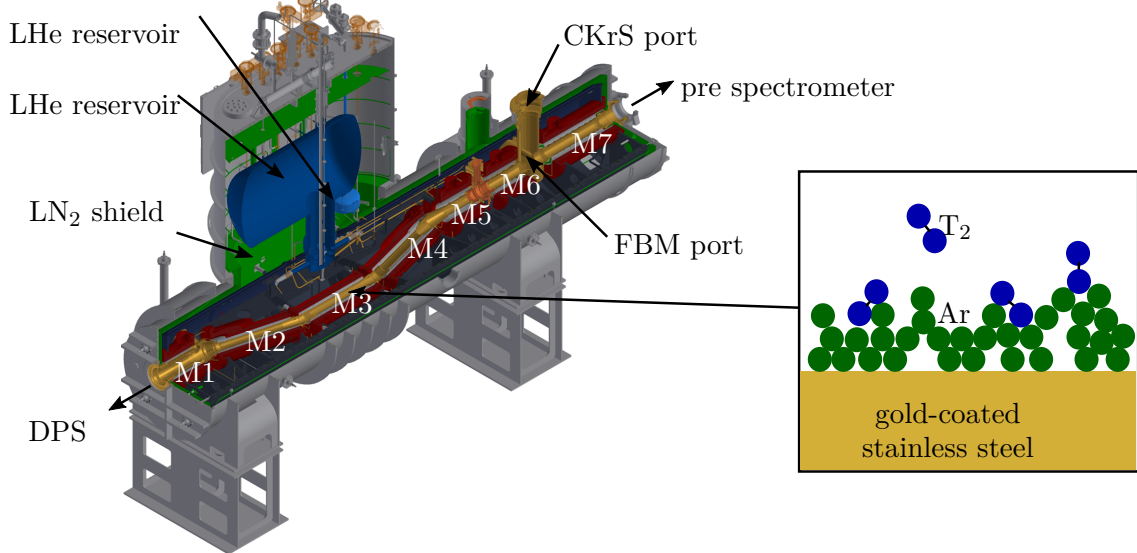


**Figure 2.5.: The cryogenic pumping section (CPS)** is the coldest part of the KATRIN experiment. It consists of 7 elements, labeled from 1 to 7 from the DPS to the pre spectrometer. Elements 2 to 5 are covered by a frozen argon layer at 3K in order to cold-trap tritium molecules. The low temperatures are established using liquid helium (LHe) and an insulation of liquid nitrogen (LN<sub>2</sub>). Each element is enclosed by a super conducting coil (M1 to M7) for magnetic guidance of the  $\beta$  electrons. For the FBM and CKrS the reader is referred to the main text. (Adapted from [Sei19].)

## 2.6. Pre and Main Spectrometer

The pre and main spectrometer are vacuum vessels designed to filter passing electrons according to their kinetic energy. The pre spectrometer has a length of 3.4 m and a diameter of 1.7 m. Details on its design can e. g. be found in [Val09; Frä10]. The main spectrometer has a length of 23 m and a diameter of 10 m. Details on its design can e. g. be found in [Val09; Val04]. The functionality and purpose of spectrometer related aspects are reviewed in this section. The content is divided into two parts: Section 2.6.1 explains the so-called MAC-E filter principle and section 2.6.2 list several measures to keep the strict KATRIN background requirements.

### 2.6.1. MAC-E-filter principle

The pre and main spectrometer are based on the principle of the so-called magnetic adiabatic collimation with electrostatic filtering (MAC-E) [BPT80]. It enables the filtering of electrons according to their kinetic energy. Figure 2.6 sketches the MAC-E filter of KATRIN. The following paragraphs outline the basic concepts and their experimental implementation. As the principle is of key importance for the KATRIN experiment, it is additionally treated in a mathematical way in the subsequent section 3.2.3.

**Electrostatic filtering:** A retarding voltage barrier is applied along the beam axis within the spectrometer, reaching its maximum  $U$  at the so-called analyzing plane in the center and dropping off towards the source and the detector. The retarding voltage barrier deflects electrons with kinetic energies below  $eU$ . For higher energies it depends on the electron's angle with respect to the beam line axis whether it can pass the spectrometer or not, see equation (3.13).

**Magnetic collimation:** The electric field gradient of the retarding voltage barrier is parallel to the beam line, but  $\beta$  electrons are emitted in an arbitrary angle with respect



**Figure 2.6.: Scheme of the KATRIN main spectrometer and the magnetic adiabatic collimation with electrostatic filtering (MAC-E) filter principle.** The KATRIN design magnetic field settings are  $B_{PS2} = 4.5$  T,  $B_S = 3.6$  T,  $B_{\max} = 6.0$  T,  $B_D = 3.6$  T,  $B_A \approx 3 \times 10^{-4}$  T.  $\vec{E}$  denotes the magnetic field regulated by the retarding potential  $U$  that reaches its maximum  $U_a = U$  at the analyzing plane. (Adapted from [Sei19].)

to the magnetic field lines. In order to analyze their full kinetic energy, they have to be collimated. This is achieved by a magnetic field gradient that drops from  $B_S = 3.6$  T in the STS to  $B_A \approx 3 \times 10^{-4}$  T in the analyzing plane. In the following a plausibility argument for the momentum collimation due to the field gradient, according to [KAT05], is given: Electrons entering the spectrometer vessel perform cyclotron motions around the magnetic field lines. Their total kinetic energy  $E_S$  is split into a longitudinal component  $E_{\parallel}$  along the beam axis and a transverse component  $E_{\perp}$

$$E_S = E_{\parallel} + E_{\perp}. \quad (2.1)$$

In the non-relativistic and adiabatic approximation the transverse component can be expressed by the magnetic field strength  $B$  and the electron's magnetic moment  $\mu$  respectively its charge  $q = e$ , its mass  $m_e$  and angular momentum  $L$  [Jac75]

$$E_{\perp} = -\mu B = \frac{e}{2m_e} LB. \quad (2.2)$$

Adiabaticity conserves angular momentum  $L$  and the total energy of the electron  $E_S$  along its trajectory. Hence, when the magnetic field strength  $B$  decreases to  $B_A = B_{\min}$  in the analyzing plane, the transverse component of the electron's energy  $E_{\perp}$  decreases likewise and transforms to longitudinal energy  $E_{\parallel}$ .

**Magnetic Bottle effect:** As the source is placed in a lower magnetic field  $B_S$  compared to the maximum field strength along the beam line  $B_{\max}$  at the detector side,  $\beta$  electrons traveling downstream to the detector are subject to the magnetic bottle effect [KAT05].

They get reflected and travel upstream to the rear wall if their starting angle  $\theta_S$  with respect to the beam line axis surpasses  $\theta_{\max}$  with

$$\sin \theta_{\max} = \sqrt{\frac{B_S}{B_{\max}}}. \quad (2.3)$$

For the KATRIN design values  $B_{\max} = 6$  T and  $B_S = 3.6$  T one obtains  $\theta_{\max} \approx 51^\circ$ . A cutting angle  $\theta_{\max}$  is beneficial because the greater the emission angle of a  $\beta$  electron the larger the distance it travels in the WGTS and the more it is subject to energy losses such as scattering or synchrotron radiation [KAT05].

**MAC-E-filter width:** Electrons with a kinetic energy below  $qU$  cannot pass the spectrometer. Electrons with a kinetic energy above  $qU + \Delta E$  do pass the spectrometer. Here,  $\Delta E$  denotes the filter width [KAT05]

$$\Delta E = \frac{B_A}{B_{\max}} E. \quad (2.4)$$

Electrons with an energy between  $eU$  and  $eU + \Delta E$  pass the potential barrier only with a certain probability. A quantitative description of this so-called transmission probability is given in the subsequent section 3.2.3. However, it can already be deduced, that a larger  $\Delta E$  adds a greater uncertainty to the measurement and thus it should be kept as low as possible.  $\Delta E$  depends on the maximum magnetic field strength along the beam line  $B_{\max} = 6$  T, the kinetic energy of  $\beta$  electrons  $E \approx 18.6$  keV, and the field in the magnetic field in the analyzing plane  $B_A \approx 3 \times 10^{-4}$  T. Hence, its KATRIN design value is  $\Delta E \approx 0.93$  eV.

**Dimensions of the KATRIN main spectrometer:** This paragraph outlines, why the diameter of the KATRIN main spectrometer is 10 m, while the one of its predecessor experiment in Mainz was only 1 m [Kra+05]. KATRIN's envisaged sensitivity requires a relative MAC-E-filter width of at least  $\Delta E/E = 1/20000$ , which directly corresponds the ratio of the magnetic fields  $B_{\max}/B_A$  (see equation (2.4)). For a smaller  $\Delta E$ ,  $B_A$  should be chosen as low as possible. However, the lower  $B_A$ , the wider the flux tube that must be governed by the spectrometer vessel. Also, the magnetic field must decrease at a sufficiently slow rate from the spectrometer's entrance to the analyzing plane in order to guarantee adiabaticity, which requires a certain spectrometer length. Dimensions that meet the demands and are feasible for the main spectrometer were found to be a radius of 10 m and a length of 23 m [KAT05; Val04].

Now, that the requirements on the magnetic and electrostatic fields are outlined, the following two paragraphs review their technical implementation:

**Magnetic field:** The main spectrometer is surrounded by a system of coils that shapes the MAC-E filter's magnetic field. Upstream, there is the PS2 magnet ( $B_{\max} = 4.5$  T); downstream the pinch ( $B_P = B_{\max} = 6.0$  T) as well as the detector magnet ( $B_D = 3.6$  T), which are superconducting solenoids. The field is fine-tuned by a system of air coils around the spectrometer hull: There is the Earth magnetic field compensation system (EMCS) with 26 current loops parallel to the beam line axis. Furthermore, there is the low-field correction system (LFCS) with 14 air coils perpendicular to the beam line axis. The combined system constrains the electrons' flux tube to the spectrometer vessel and compensates the Earth's magnetic field as well as effects from ferromagnetic materials in the spectrometer's surroundings [Erh+18]. Additionally, a vertical and radial magnetic measuring system (VMMS and RMMS) are installed outside the spectrometer vessel. The field inside the spectrometer vessel is assessed via samples of these measuring systems combined with simulations [Let+18].

**Electrostatic field:** A high-voltage system establishes the MAC-E filter's retarding potential. The fluctuation of the retarding voltages must have a standard deviation smaller

than 60 mV for the envisaged sensitivity on the neutrino mass [KAT05]. The antenna-like beam line setup is sensitive to electromagnetic fluctuations of any source, which is why an active post-regulation system is deployed. It monitors the retarding potential and regulates it with the required precision. For the monitoring the monitor spectrometer and a voltage divider are deployed. For details on the later systems the reader is referred to [Thü+09; Erh+14; Zbo11].

### 2.6.2. Background Mitigation Strategies

The KATRIN sensitivity goal requires a background rate of less than 10 mcps [KAT05]. Several background-related aspects with respect to the spectrometer tanks are:

**Vacuum:** The spectrometers are operated at a pressure on the order of  $1 \times 10^{-11}$  mbar. This prevents electron scattering on residual gas and minimizes background effects by ionization. Correspondingly, turbo molecular and getter pumps are installed at three pump ports of the spectrometer vessels. Furthermore, the spectrometers can be baked out at up to 350 °C [Are+16].

**Wire electrodes:** The inner walls of the spectrometer vessels are lined by wire electrodes. Their potential is at a few hundred volts more negative than the spectrometer hull reflecting electrons coming from the vessel walls. Such electrons may be induced by cosmic rays [Val09].

**Ion blocking:** Analogously to the ones in the CPS (section 2.5), three blocking electrodes are installed; one between the CPS and the pre spectrometer, one between the pre and main spectrometer; and one between the main spectrometer and the detector [Klein19].

**Tandem setup:**  $\beta$  electrons may scatter on residual gas. This can either directly lead to secondary electrons or create positive ions that travel down the beam line. The positive ions in turn may again yield secondary electrons through scattering. The more  $\beta$  electrons enter the main spectrometer, the higher is the probability to create secondary electrons. In order to reduce the flux of  $\beta$  electrons into the main spectrometer, the retarding potential of the pre spectrometer is set to a few hundred volts more positive than the one of the main spectrometer. On the one hand this is a countermeasure against background events, but on the other hand, charged particles can be trapped between the two spectrometers due to the electromagnetic setup (Penning trap). A sudden discharge may harm the hardware, especially the detector. Therefore, it is possible to sweep a charged wire through the volume in order to collect the trapped particles and avoid this “Penning discharges” [Val09].

## 2.7. Detector Section

The detector section terminates the beam line in downstream direction. It can be separated from the spectrometer section by closing a gate valve. The detector section is depicted in figure 2.7 and a detailed description can e.g. be found in [Ams+15]. In the following the major features of the detector section are reviewed:

**Focal plane detector (FPD):** The FPD counts the  $\beta$  electrons that pass the spectrometer section. It is a *pin*-silicon detector with a sensitive area of 9 cm diameter. It is subdivided in 148 pixels of the same area arranged in 12 rings of 12 pixels each and the so called bull’s eye of 4 pixels in the center. This arrangement allows later correction for radial electrical, magnetic and gas dynamical inhomogeneities in the beam line [Ams+15].

**Shield and veto system:** The radiation shield of the FPD system consists of two nested cylindrical shells: an outer lead shell of 3 cm that reduces photon background and an inner copper shell of 1.27 cm that blocks X-rays originating from the outer lead shell. The shield is surrounded by a veto system to tag incoming muons. Such a system is necessary to keep the strict background requirements [Ams+15].

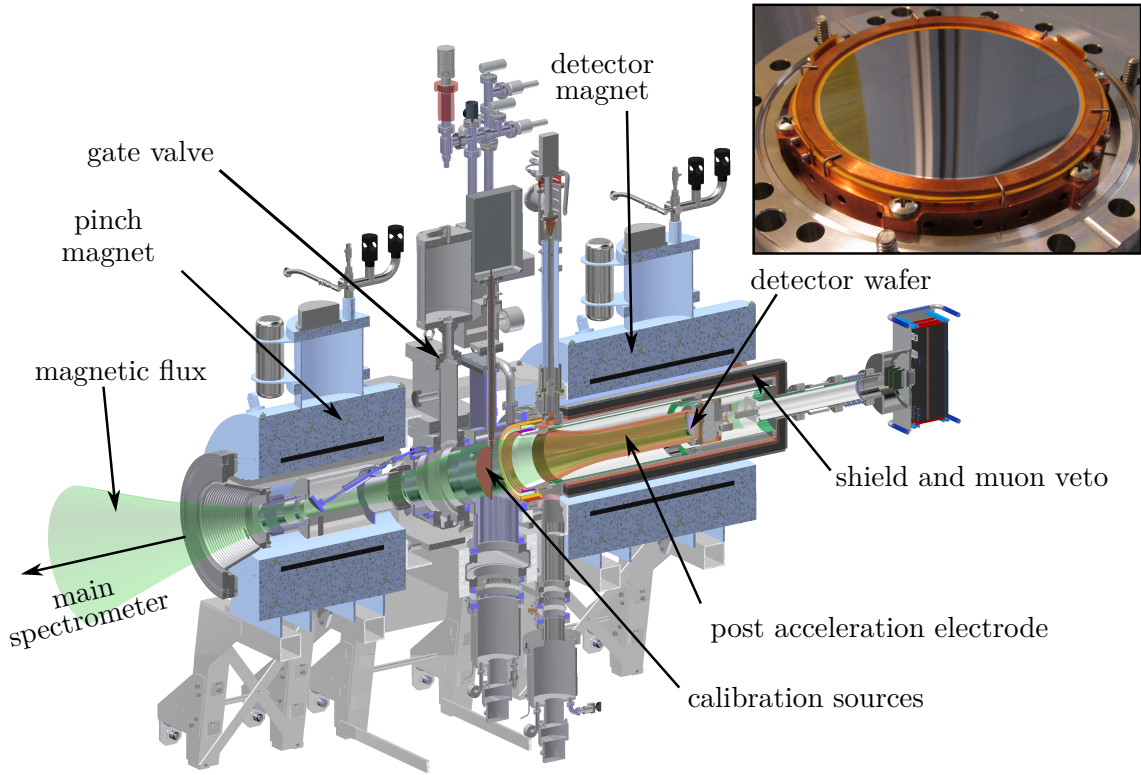


**Figure 2.7.: The detector section** terminates the KATRIN beam line. Among other instruments it houses the focal plane detector (FPD) for  $\beta$  electrons with the detector wafer at its core. For an explanation of the other components the reader is referred to the main text. (Adapted from [Sei19].)

**Calibration:** Photoelectron sources can be lowered in the line of sight of the detector. The corresponding photocurrent can be measured with the precision ultra-low current integrating normalization electrometer for low-level analysis (PULCINELLA) system. A comparison of PULCINELLA and the FPD yields the FPD's detection efficiency. It was determined to be  $\epsilon_{\text{det}} = 95 \pm 1.8 \pm 2.2\%$  [Ams+15].

**Detector magnet:** The detector magnet ( $B_D = 3.6$  T) allows to form the flux tube near the detector independently of the main spectrometer magnetic field setting. It especially allows its mapping on the the detector [Ams+15].

**Post-acceleration electrode:** The post-acceleration potential shifts the electrons arriving from the main spectrometer to a more favorable energy region. This increases the detector efficiency and, additionally,  $\beta$  electrons can be distinguished from noise originating in the detector by an energy region of interest cut. An appropriate setting was found to be  $\sim 10$  keV [Ams+15].

### 3. Mathematical Formalism of a KATRIN Measurement

For neutrino mass inference from data or simulation a mathematical model of a KATRIN neutrino mass measurement is required. As parameter inference is of importance within the scope of this thesis, a mathematical formalism describing a KATRIN neutrino mass measurement is outlined within this chapter. Therefore, an expression for the  $\beta$ -decay rate of a tritium molecule is given in section 3.1. Section 3.2 describes the KATRIN response function, respectively the mathematical modeling of the KATRIN apparatus. Sections 3.3 combines the concepts of the two preceding sections into the  $\beta$ -electron rate at the KATRIN detector. Section 3.4 incorporates the detector efficiency, the background rate and the measurement time in order to translate the rates into an expression for the electron counts measured by the KATRIN detector for a fixed retarding potential. Section 3.6 introduces the concept of a measurement time distribution over retarding potentials. Finally, section 3.7 shows a full simulated KATRIN neutrino mass measurement.

#### 3.1. Differential Tritium- $\beta$ -Decay Spectrum

This section presents a quantitative expression for the  $\beta$ -decay rate of a tritium molecule in dependence on the kinetic energy of the emitted  $\beta$  electron (differential rate). First the whole mathematical description is denoted, then its components are explained.

Using Fermi theory and Fermi's golden rule the decay rate of a tritium molecule is [Kle+19; OW08]

$$\frac{d\Gamma(E_S)}{dE_S} = \frac{G_F^2 |V_{ud}|^2}{2\pi^3} |M_{\text{nuc}}|^2 \cdot F(Z, E_S) \cdot p(E_S + m_e) \cdot \sum_f P_f \cdot \epsilon_f \cdot \sqrt{\epsilon_f^2 - m_\nu^2} \cdot \Theta(\epsilon_f - m_\nu). \quad (3.1)$$

Its constituents are the kinetic electron energy  $E_S$ ; the effective electron-antineutrino mass  $m_\nu$  defined via the PMNS matrix  $U$  (see equation 1.4),

$$m_\nu^2 = |U_{ei}|^2 m_i^2; \quad (3.2)$$

the Fermi constant  $G_F$ ; the up-down-quark-coupling given by the Cabibbo angle  $\theta_C$  [Tan+18]

$$V_{ud} = \cos \theta_C = 0.97425 \pm 0.00022; \quad (3.3)$$

and the nuclear transition matrix element [Tan+18]

$$|M_{\text{nuc}}|^2 = g_V^2 + 3g_A^2 \quad \text{with } g_V = 1 \quad \text{and} \quad g_A/g_V = -1.2646 \pm 0.0035 \quad (3.4)$$

which is independent of the electron's kinetic energy as the decay is super-allowed and given by the vector  $g_V$  and axial vector  $g_A$  coupling.



**Figure 3.1.: Tritium- $\beta$  spectrum for a vanishing and non-vanishing neutrino mass.** The plot shows the differential rate as described by equation (3.1) for a vanishing and non-vanishing neutrino mass. The inset zooms into the endpoint region where a non-vanishing mass causes a shift and a distortion of the spectrum. (Calculated with [S-SSC].)

Furthermore, the Fermi function  $F(Z, E_S)$  accounts for the Coulomb interaction between the outgoing electron and the daughter nucleus with atomic charge  $Z = 2$ , which in its relativistic version can be approximated as [Sim81]

$$F(Z, E_S) \approx \frac{2\pi\eta}{1 - \exp 2\pi\eta} \cdot R, \quad (3.5)$$

with Sommerfeld parameter  $\eta = \alpha Z/\beta$ , fine structure constant  $\alpha$ , relativistic velocity  $\beta$  and a relativistic correction factor  $R = 1.002037 - 0.001427\beta$ .

The phase-space factor of the outgoing electron with momentum  $p$  and mass  $m_e$  is given by the factor  $p(E_S + m_e)$ .

The phase space factor of the emitted neutrino depends on multiple quantities: First, there is the  $\beta$ -spectrum endpoint of molecular tritium  $E_0 = (18\,574.00 \pm 0.07)$  eV [Mye+15; OW08]. Second, there is the final state energy of the molecule  $V_f$ . The excited energy state  $f$  is caused by vibration, rotation or electronic excitation of the decaying molecule. A review on tritium molecular final states and tabulated values can e.g. be found in [BPR15] and references therein. The probability that the molecule is in a final state of energy  $V_f$  after the decay is denoted by  $P_f$ . Then the energy of the neutrino reads

$$\epsilon_f = E_0 - E - V_f. \quad (3.6)$$

Third, there is the neutrino's momentum  $\sqrt{\epsilon_f^2 - m_\nu^2}$ . Then, the complete phase space factor of the neutrino is a sum over all possible molecular final states labeled  $f$ .

Lastly, the Heavyside step function  $\Theta$  ensures a positive kinetic energy of the neutrino.

The differential rate is depicted in figure 3.1 for a vanishing and non-vanishing effective electron-antineutrino mass. The difference of the two  $\beta$  spectra forms the foundation for neutrino mass inference at KATRIN.

### 3.2. Response Function

The aim of this chapter is an introduction to the mathematical formalism for the electron rate at the KATRIN detector. The previous section 3.1 gives an expression for the differential  $\beta$ -electron rate. The next step is the inclusion of the characteristics of the KATRIN experimental setup. This can be accomplished by denoting the KATRIN response function. In the outlined formalism, it reflects the probability of an electron emitted in the WGTS to reach the KATRIN detector [Gro15] (the detector efficiency is treated separately.)

First, central concepts and the nomenclature are presented in section 3.2.1. Then, components of the response function are introduced:

- The gas dynamics within the STS needs to be simulated. See section 3.2.2.
- The characteristics of the KATRIN spectrometer can be summarized in the transmission function. See section 3.2.3.
- The passage of electrons through the WGTS is influenced by scattering from gas molecules. The probability for such scattering is discussed in section 3.2.4. Furthermore, the amount of energy an electron loses when scattering is considered in section 3.2.5.

Finally, the described components will be assembled to the KATRIN response function in section 3.2.6.

#### 3.2.1. Concepts and Nomenclature

Before the formalism for the KATRIN response function is developed, this section introduces naming conventions and useful concepts.

##### Coordinate System

This chapter focuses on a one-dimensional description of the KATRIN response function. The position along the beam line is denoted with  $z$ . The origin of the coordinates system is the center of the WGTS as already chosen in previous works, e. g. [Gro15; Kle14]. In this sense, the rear and the front of the WGTS of length  $d$  have the coordinates  $\mp d/2$ .

##### Pitch Angle

Within this chapter the angle between an electron's direction of motion and the beam line axis, the so-called pitch angle, is denoted by  $\theta$ .

##### Parameter Indices

Whether an electron reaches the KATRIN detector depends i. a. on its parameters when originating in the WGTS. Within this chapter these starting parameters are denoted with a lower index S. The three decisive starting parameters are the following:

1. The starting kinetic energy  $E_S$  as discussed within the description of the differential rate in equation (3.1).
2. The starting position  $z_S$  within the WGTS.
3. The starting pitch angle  $\theta_S$  within the WGTS.

Parameters that denote quantities in the analyzing plane (see section 2.6) are denoted with a lower index A.

## Probabilistic Treatment of the Starting Pitch Angle

It should be noted, that the three listed starting parameters are not known for a single  $\beta$  electron, which suggests a probabilistic treatment. Within the scope of this thesis this is of importance with respect to the starting pitch angle. Therefore, the concept is explained in the following:

Given the distribution  $\omega(\theta_S)$  of starting pitch angles, the mean value of any function  $g(\theta_S)$  depending on a fixed starting pitch angle  $\theta_S$  can be calculated within an interval  $[0, \theta_{\max}]$  by applying the definition of the mean value

$$\langle g(\theta_S) \rangle = \frac{\int_0^{\theta_{\max}} \omega(\theta_S) g(\theta_S) d\theta_S}{\int_0^{\theta_{\max}} \omega(\theta_S) d\theta_S}. \quad (3.7)$$

An isotropic  $\beta$ -electron emission by a tritium molecule into the unit sphere, meaning all combinations of spherical emission angles  $(\varphi, \vartheta = \theta_S)$  are equally likely, yields as distribution for the starting pitch angles [KAT05]

$$\omega(\theta_S) = \sin \theta_S \quad (3.8)$$

with normalization

$$\int_0^{\theta_{\max}} \omega(\theta_S) d\theta_S = \frac{1}{1 - \cos \theta_{\max}}. \quad (3.9)$$

Within this chapter  $\theta_{\max}$  denotes the maximum acceptance angle due to the magnetic bottle effect as explained in section 2.6.1 with a design value of  $\theta_{\max} \approx 51^\circ$  [KAT05]. This calculation of the mean value is applied multiple times within this chapter and in the scope of this thesis.

### Experimental Settings

As the response function models the characteristics of the KATRIN apparatus it naturally depends on the experimental settings. The quantities used within this chapter are listed in the following:

- the magnetic field  $B_S$  at the place of origin of a  $\beta$  electron within the WGTS;
- the magnetic field  $B_A$  within the analyzing plane;
- the maximum magnetic field  $B_{\max}$  along the beam line axis;
- the retarding voltage  $U$  and the retarding energy  $qU$ ;
- the starting potential  $U_S$  of a  $\beta$  electron within the WGTS.

For the detailed meaning of these parameters and their KATRIN design values, see section 2.6. It should be noted, that none of these quantities are constant, but they exhibit a spatial, especially a radial, dependency [KAT05]. For ease of notation, the spatial dependency is left implicit within this chapter.

#### 3.2.2. Gas Dynamics

The gas dynamics within the STS has to be simulated. This topic is not treated in detail here. The reader is referred to [Höt12]. In short, in a one-dimensional description the output of such a gas dynamic simulation is the gas molecule density  $\rho(z)$ . For nominal settings, averaging  $\rho(z)$  along the beam line axis and multiplication by the length  $d$  of the WGTS yields the design column density  $\rho d = 5 \times 10^{17} \text{ cm}^{-2}$  [KAT05].

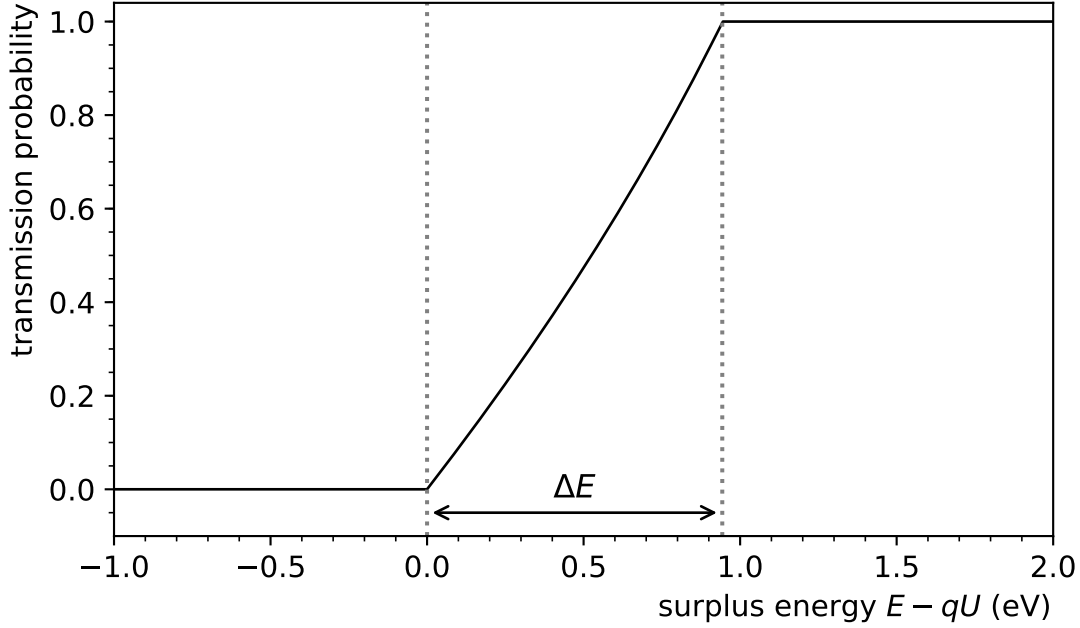


**Figure 3.2.: The KATRIN transmission function** as described by equation (3.13). It denotes the probability for an electron with a kinetic energy  $E$  to pass through the spectrometer set to a retarding potential of  $U$ . The probabilistic treatment of the starting pitch angles of electrons leads to the MAC-E-filter width  $\Delta E$  with the nominal value of  $0.93 \text{ eV}^2$  [KAT05]. (Calculated with [S-SSC].)

### 3.2.3. Transmission Function

The transmission function denotes the probability of an electron to pass the MAC-E filter. It can be characterized by the transmission energy [Gro15]

$$E_{\text{tr}}(qU, E, \theta_S) = \frac{q(U - U_S)}{1 - \sin^2 \theta_S \frac{B_A}{B_S} \frac{\gamma(E) + 1}{\gamma_A + 1}}. \quad (3.10)$$

where  $\gamma(E)$  and  $\gamma_A$  denote the relativistic Lorentz factor of the  $\beta$  electrons with energy  $E$  and in the analyzing plane. As the electrons are slowed down substantially by the retarding potential in the spectrometer, it holds  $\gamma_A \approx 1$ . In the following, for ease of notation, also  $U_S = 0$  and  $\gamma_S = 1$  is assumed.

Electrons pass the MAC-E filter if their energy  $E$  when arriving at the spectrometer surpasses the transmission energy  $E_{\text{tr}}$ , equation (3.10). This condition can be resolved for the starting pitch angle [Gro15]

$$\begin{aligned} E &> E_{\text{tr}}(qU, E, \theta_S) \\ \Leftrightarrow \theta_S &< \theta_{\text{tr}}(E, qU) := \arcsin \left( \sqrt{\frac{E - qU}{E} \frac{B_A}{B_S}} \right). \end{aligned} \quad (3.11)$$

Using equation (3.11), the transmission function depending on the starting pitch angle and the starting energy of electrons can be formulated as a step function

$$\mathcal{T}(E, qU, \theta_S) = \begin{cases} 1 & \text{if } \theta_S < \theta_{\text{tr}}(E, qU) \\ 0 & \text{otherwise} \end{cases}. \quad (3.12)$$

Calculating the mean value of this step function with respect to the probabilistic distributed starting pitch angles of  $\beta$  electrons as described in section 3.2.1 yields the KATRIN transmission function [KAT05]

$$T(E, qU) = \langle \mathcal{T}(E, qU, \theta_S) \rangle = \begin{cases} 0 & \text{if } E < qU \\ \frac{1 - \sqrt{1 - \frac{E - qU}{E} \frac{B_S}{B_A}}}{1 - \sqrt{1 - \frac{\Delta E}{E} \frac{B_S}{B_A}}} & \text{if } qU < E < qU + \Delta E , \\ 1 & \text{if } qU + \Delta E < E \end{cases} \quad (3.13)$$

where

$$\Delta E = E \cdot B_A / B_{\max} \quad (3.14)$$

is the MAC-E-filter width as explained in section 2.6. The transmission function is depicted in figure 3.2 for the KATRIN design values.

### 3.2.4. Probability of Electron Scattering within the WGTS

This section derives an expression for the probability  $P_l$  of an electron to scatter  $l$  times within the WGTS.

The electron moves on a spiral track due to its cyclotron motion in the magnetic field in the WGTS. Therefore, when traveling an infinitesimal distance  $dz$  in  $z$ -direction, it travels a total distance of

$$ds = \frac{1}{\cos \theta_S} dz . \quad (3.15)$$

Remarkably, this expression is independent of the electron energy and the magnetic field strength in the WGTS. The effective column density can then be expressed as a line integral along the electrons path  $\varphi$  over the gas density  $\rho(z)$  from the starting position of the electron to the point where it leaves the WGTS

$$\lambda(z_S, \theta_S) = \int_{\varphi} \rho(\vec{r}) ds = \frac{1}{\cos \theta_S} \int_{z_S}^{d/2} \rho(z) dz . \quad (3.16)$$

Then, the expected scattering count is the product of the effective column density  $\lambda(z_S, \theta_S)$  and the scattering cross section  $\sigma$  [Gro15]

$$\mu(z_S, \theta_S) = \lambda(z_S, \theta_S) \sigma . \quad (3.17)$$

Using  $\mu(z_S, \theta_S)$ , the probability for  $l$ -fold scattering can be expressed as a Poisson distribution [Gro15]

$$P_l(z_S, \theta_S) = \frac{\mu(z_S, \theta_S)^l}{l!} e^{-\mu(z_S, \theta_S)} . \quad (3.18)$$

The mean value with respect to the starting positions and the starting pitch angles can be calculated [Gro15]

$$\bar{P}_l = \frac{1}{d} \int_{-d/2}^{d/2} \frac{1}{1 - \cos \theta_{\max}} \int_0^{\theta_{\max}} \sin \theta_S P_l(z_S, \theta_S) d\theta_S dz_S . \quad (3.19)$$

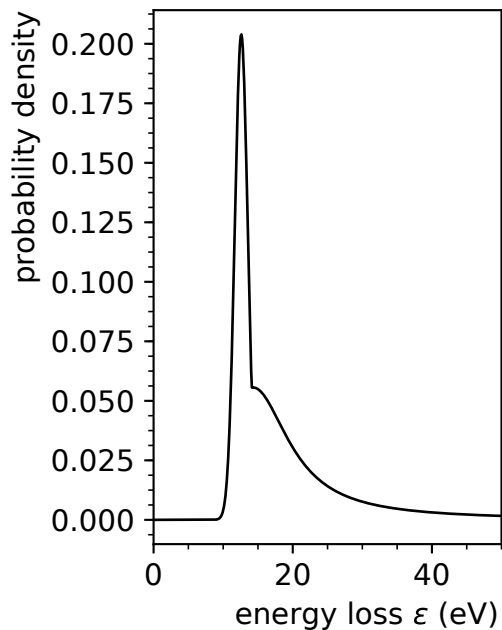
Table 3.1 lists the numerical evaluation of these averaged scattering probabilities. With these probabilities at hand, the next step is the derivation of the energy an electron loses when scattering.

**Table 3.1.: Probability for electron scattering within the WGTS averaged over starting positions and pitch angles.** Listed are the evaluations of equation (3.19) for the following input parameters: A scattering cross section of  $\sigma = 3.456 \times 10^{-22} \text{ m}^2$  [KAT05], a constant gas column density  $\rho d = 5 \times 10^{17} \text{ cm}^{-2}$ , a WGTS length of  $d = 10.0820 \text{ m}$  and a maximum acceptance angle of  $\theta_{\max} = 50.7685^\circ$ . The same values can be found in [Gro15; Kle14]. The reader is also referred to a review of this values in section 5.2.

scattering count $l$	scattering probability according to equation (3.19)
0	41.33 %
1	29.27 %
2	16.73 %
3	7.91 %
4	3.18 %

**Figure 3.3.: The energy loss probability density due to electron scattering in the WGTS given by equation (3.21) and determined at the Troitsk experiment [Ase+00].** The table below lists the corresponding parameters, where  $\epsilon_1$  was fixed and  $\epsilon_c$  was chosen to make the piece wise defined function continuous.

parameter	value
$A_1$	$0.204 \pm 0.001$
$A_2$	$0.0556 \pm 0.0003$
$\omega_1$	$(1.85 \pm 0.02) \text{ eV}$
$\omega_2$	$(12.5 \pm 0.1) \text{ eV}$
$\epsilon_1$	12.6 eV
$\epsilon_2$	$(14.30 \pm 0.02) \text{ eV}$
$\epsilon_c$	14.09 eV



### 3.2.5. Energy Loss of Electrons due to Scattering

This section describes the “energy loss function”  $f_l(\epsilon)$ . It denotes the probability density for an electron to loose an energy  $\epsilon$  when scattering  $l$  times. Only the case of inelastic scattering is treated here. For an additional treatment of elastic scattering, which is less likely by one order of magnitude, the reader is referred to [Kle+19].

The energy loss function for no scattering is the Dirac delta function [Kle+19]

$$f_0(\epsilon) = \delta(\epsilon) . \quad (3.20)$$

A phenomenological description for 1-fold scattering of electrons from hydrogen isotopologues was derived from data at the Troitsk experiment [Ase+00; Abd+17]

$$f_1(\epsilon) = \begin{cases} A_1 e^{-2\left(\frac{\epsilon-\epsilon_1}{\omega_1}\right)^2} & \text{if } \epsilon < \epsilon_c \\ A_2 \frac{\omega_2^2}{\omega_2^2 + 4(\epsilon - \epsilon_2)^2} & \text{if } \epsilon \geq \epsilon_c \end{cases} \quad (3.21)$$

Figure 3.3 depicts this energy loss function. It should be noted that in the scope of this thesis a more recent, preliminary energy loss model derived from a dedicated subgroup of the KATRIN collaboration is investigated in chapter 6.

For multiple scattering the above function  $f_1$  has to be convoluted with itself and the energy loss function becomes [Kle+19]

$$f_l(\epsilon) = \bigotimes_{i=0}^l f_1(\epsilon) \quad (3.22)$$

where  $\otimes$  denotes the convolution

$$(f \otimes f)(\epsilon) = \int_{-\infty}^{\infty} f(\epsilon - \epsilon') f(\epsilon') d\epsilon'. \quad (3.23)$$

### 3.2.6. Assembly of the KATRIN Response Function

This section gives an expression for the KATRIN response function. It should be noted that the chosen notation differs slightly from those used in the works [Gro15; Kle+19], that this derivation is largely based on. The latter make approximations of the transmission properties and introduce more involved concepts where the approximations do not hold. Here, this approach is inverted: First, the involved concepts are applied and the approximations are introduced in a second step. However, the final results reconcile.

The KATRIN response function in dependence on the starting position and pitch angle of an electron reads

$$\mathcal{R}(E_S, qU, z_S, \theta_S) = \sum_l \int_{-\infty}^{\infty} \mathcal{T}(E_S - \epsilon, qU, \theta_S) \cdot P_l(z_S, \theta_S) \cdot f_l(\epsilon) d\epsilon \quad (3.24)$$

$$= \sum_l \int_0^{\infty} \mathcal{T}(E_S - \epsilon, qU, \theta_S) \cdot P_l(z_S, \theta_S) \cdot f_l(\epsilon) d\epsilon. \quad (3.25)$$

where the integral goes over the energy losses, the sum goes over the scattering count,  $\mathcal{T}$  denotes the non-averaged transmission function (3.13),  $P_l$  the non-averaged scattering probabilities (3.18) and  $f_l$  the energy loss function (3.22). The cut of the lower integral limit is caused by the vanishing energy loss function ( $f_l(\epsilon) = 0$  if  $\epsilon < 0$ ). In words, the transmission function is smeared using the energy loss function as a smearing kernel and then a weighted sum is formed over generations of  $l$ -fold scattered electrons where the weight is the probability to scatter  $l$  times.

The mean value of equation (3.24) with respect to the starting pitch angle can be calculated as described in section 3.2.1. Also the corresponding integral is swapped with the integral over the energy loss and the sum over the scattering count

$$\begin{aligned} R(E_S, qU, z_S) &= \langle \mathcal{R}(E_S, qU, z_S, \theta_S) \rangle \\ &= \sum_l \int_0^{\infty} \int_0^{\theta_{\max}} \frac{\sin \theta_S \cdot \mathcal{T}(E_S - \epsilon, qU, \theta_S) \cdot P_l(z_S, \theta_S)}{1 - \cos \theta_{\max}} d\theta_S \cdot f_l(\epsilon) d\epsilon. \end{aligned} \quad (3.26)$$

This expression can be reformulated to have the same form as the non-averaged response function (3.24). This means, the product “transmission function times scattering probability times energy loss function” can be reestablished, which also reconciles the notation with the expression given in [Gro15]. Therefore, the factor  $1 = \bar{P}_l / P_l$  with the averaged scattering probabilities from equation (3.19) is introduced into equation (3.26) and the “detailed

transmission function”  $T_l^*$  is defined

$$\begin{aligned} R(E_S, qU, z_S) &= \sum_l \int_0^\infty \underbrace{\int_0^{\theta_{\max}} \frac{\sin \theta_S \cdot \mathcal{T}(E_S - \epsilon, qU, \theta_S) \cdot P_l(z_S, \theta_S)}{(1 - \cos \theta_{\max}) \cdot \bar{P}_l} d\theta_S \cdot \bar{P}_l \cdot f_l(\epsilon) d\epsilon}_{T_l^*(E_S - \epsilon, qU, z_S)} \\ &= \sum_l \int_0^{E_S - qU} T_l^*(E_S - \epsilon, qU, z_S) \cdot \bar{P}_l \cdot f_l(\epsilon) d\epsilon, \end{aligned} \quad (3.27)$$

where the cut on the upper integral limit from  $\infty$  to  $E_S - qU$  is justified below.

The non-averaged transmission function  $\mathcal{T}$  (3.11) within  $T_l^*$  is a step function with respect to the starting pitch angle  $\theta_S$  of an electron. This cuts the upper integral limit from  $\theta_{\max}$  to  $\theta_{\text{tr}}$  when integrating over  $\theta_S$ . Furthermore, in analogy to the KATRIN transmission function from equation 3.13, a distinction of cases avoids imaginary square roots. One obtains the detailed transmission function as given in [Gro15; Kle+19]

$$T_l^*(E, qU, z_S) = \begin{cases} 0 & \text{if } E < qU \\ \int_0^{\theta_{\text{tr}}(E, qU)} \frac{\sin \theta_S \cdot P_l(z_S, \theta_S)}{(1 - \cos \theta_{\max}) \cdot \bar{P}_l} d\theta_S & \text{if } qU < E < qU + \Delta E, \\ 1 & \text{if } qU + \Delta E < E \end{cases}, \quad (3.28)$$

where  $\theta_{\text{tr}}$  denotes the transmission-pitch angle (3.11) and  $\Delta E$  the MAC-E-filter width (3.14). As  $T_l^*$  vanishes for  $E < qU$  the upper integral limit over energy losses in the response function 3.27 can be cut to  $E_S - qU$ . Furthermore, it was found, that for  $l > 3$  scatterings the detailed transmission  $T_l^*$  function can be exchanged for the KATRIN transmission function (3.13) without making a significant error [Gro15].

## Summary

In equation 3.27 the KATRIN response function was derived, which reconciles with the expressions given in [Gro15; Kle+19]

$$R(E_S, qU, z_S) = \sum_l \int_0^{E_S - qU} T_l^*(E_S - \epsilon, qU, z_S) \cdot \bar{P}_l \cdot f_l(\epsilon) d\epsilon, \quad (3.29)$$

where  $T_l^*$  is the detailed transmission function, equation (3.28),  $\bar{P}_l$  are the averaged scattering probabilities, equation (3.19) and  $f_l$  is the energy loss function, equation (3.22). The response function denotes the probability of an electron starting with an energy  $E_S$  at a position  $z_S$  to overcome the retarding energy  $qU$  and reach the detector.

Figure 3.4 shows the response function for two different starting positions of electrons as well as averaged over all starting positions. It exhibits many features: For unscattered electrons the response function resembles the transmission function. This causes the steep rise at  $E_S - qU = 0$  eV within the interval of the MAC-E-filter width  $\Delta E \approx 0.93$  eV. As the transmission probability is weighted by the probability for no scattering, the plateaus resemble the corresponding probabilities (equation 3.18 averaged over starting pitch angles):  $\sim 12\%$  (rear),  $41.33\%$  (average, see table 3.1),  $\sim 98\%$  (front). The discontinuity in the first derivative of the energy loss function at  $\epsilon_c = 14.09$  eV causes kinks. As the energy loss function has an onset at  $\epsilon_0 \approx 10$  eV, the corresponding kinks are at  $n \cdot \epsilon_0 + \epsilon_c$  ( $n \in \{0, 1, \dots\}$ ) and increasingly smoothed for higher  $n$ . (Also see figure 3.3 for the energy loss function.) The response function (3.29) can be understood as a weighted sum of smeared transmission functions approximately shifted by the onset of the energy loss function. Electrons starting from the front of the WGTS are unlikely to scatter, which is why the response function almost resembles the transmission function. Electrons starting from the rear are likely

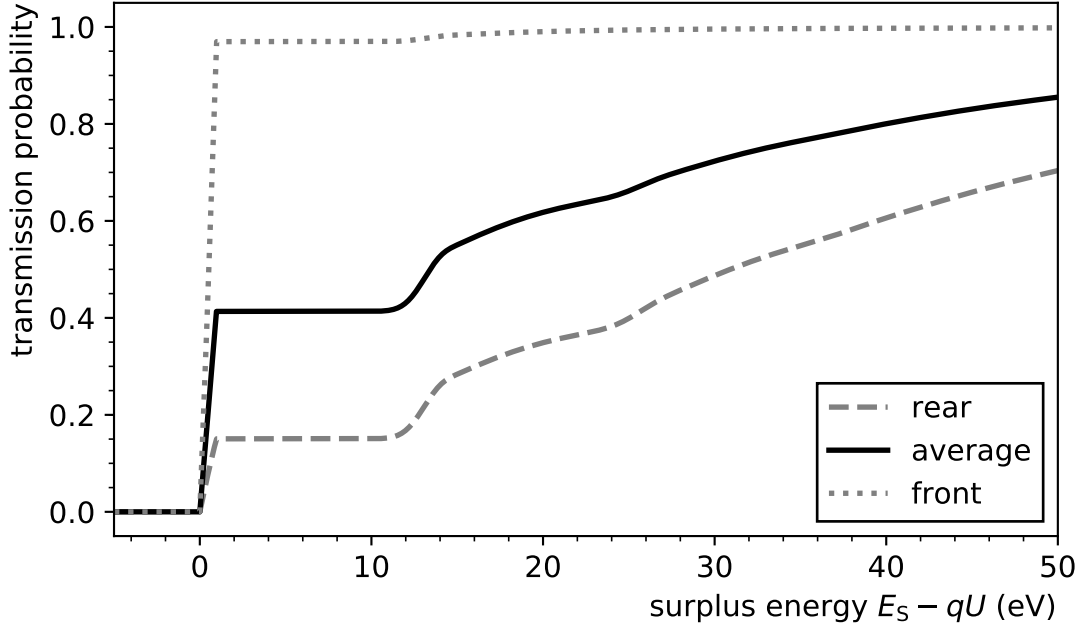


**Figure 3.4.: The KATRIN response function** at a retarding energy of  $qU = 18\,545$  V. It is depicted for three cases: for electrons starting  $\sim 9$  mm from the rear and front of the WGTS and averaged over all starting positions. For a description of the manifold features, the reader is referred to the main text. (Calculated with [S-SSC].)

to scatter. Thus, the corresponding response function shows the features of multiple scatterings. For multiple scatterings, the sharp edges of the transmission function are smoothed by the energy loss, which is why only one sharp edge and one plateau, namely for the no-scattering case, is apparent.

### 3.3. Integral Rate

This section gives an expression for the integral  $\beta$ -electron rate at the KATRIN detector.

As already mentioned, the response function (3.29) depends on the starting position of the electrons. To account for this, the WGTS can be thought of being divided into  $n$  slices of width  $w = d/n$  and an averaged response function for the  $j$ th ( $j \in \{0, 1, \dots, n-1\}$ ) slice can be given

$$R(E_S, qU, z_S) \rightarrow R_j(E_S, qU) = \int_{-d/2+jw}^{-d/2+(j+1)w} R(E_S, qU, z_S) dz_S. \quad (3.30)$$

As can be seen from equations (3.29) and (3.28), this averaging integral can be propagated to the scattering probabilities in the enumerator of the detailed transmission function.

The integral rate then reads [Kle+19]

$$\Gamma(qU) = \frac{1}{2} \sum_{j=0}^n N_{j,T} \cdot \int_{qU}^{E_0} \left( \frac{d\Gamma(E_S)}{dE_S} \right) \cdot R_j(E_S, qU) dE_S. \quad (3.31)$$

Here, the integral goes over all starting energies that enable electrons to overcome the retarding potential. The transmission probability vanishes for starting energies smaller than  $qU$  and the differential rate vanishes for energies above the  $\beta$ -spectrum endpoint  $E_0$  (see equation 3.1), which yields the two integral limits. The sum goes over all slices of the

WGTS.  $N_{j,T}$  is the number of tritium nuclei in the  $j$ th slice of the WGTS. And the factor 1/2 accounts for the fact, that on average only half the  $\beta$  electrons are emitted towards the detector.

### 3.4. Detector Counts

This section gives an expression for the electron counts measured by the KATRIN detector.

Therefore, the detector efficiency  $\epsilon_{\text{det}} \in [0, 1]$  has to be taken into account. (For a description, its determination and value see section 2.7.) Furthermore, the background rate  $\Gamma_{\text{bg}}$  with a nominal value of 10 cps [KAT05] has to be considered. Also a relative rate factor  $A_S = 1$  between the background and the  $\beta$ -electron rate is introduced as it can be used in fitting procedures (see section 4.3.) Assuming a measurement time of  $t(qU)$  attributed to a retarding energy  $qU$ , the detector counts are [Kle14]

$$N(qU) = t(qU) \cdot \epsilon_{\text{det}} \cdot (A_S \cdot \Gamma(qU) + \Gamma_{\text{bg}}), \quad (3.32)$$

where  $\Gamma(qU)$  denotes the integral rate (3.31).

### 3.5. Model Amendments

The outlined formalism that lead to the expression for the detector counts (3.32) forms a scaffold for the mathematical formalism that describes a KATRIN measurement. Modifications of isolated terms can incorporate further effects. For a comprehensive list, the reader is referred to [Kle+19]. Selected examples are listed below:

- **Doppler effect:** Gas flow and temperature move the tritium molecules and hence, smear the kinetic energy distribution of  $\beta$  electrons (see section 2.2). This can be modeled by convolving the differential rate (3.1) with a Maxwellian distribution or by applying corrections to the final energy states of the decaying molecules.
- **Plasma potential:** Space charges, respectively a plasma, forms within the WGTS due to the tritium decay (see section 2.2).  $\beta$  electrons may originate at higher/lower potentials due to space charges. This can be modeled by an adaption of the starting potential  $U_S$  in the transmission energy (3.10).
- **3-dimensional description:** This chapter focuses on a 1-dimensional formalism. However, as noted, input parameters such as the magnetic fields are not solely  $z$ -dependent, which requires a 3-dimensional approach and an incorporation of the segmentation of the detector. This can be accomplished by calculating the detector counts (3.32) separately for each detector pixel exploiting that the magnetic flux tube maps specific volumes of the WGTS onto specific areas of the analyzing plane and detector pixels.

### 3.6. Measurement Time Distribution

KATRIN measures electron counts as described in equation (3.32) at a set of retarding energies  $\{qU_i\}$ . How much measurement time  $t(qU_i)$  is attributed to a certain retarding energy is specified in a measurement time distribution (MTD). The MTD influences the experiment's sensitivity to the neutrino mass. An optimal MTD balances the following aspects:

1. Some measurement time has to be attributed to retarding energies beyond the endpoint of the integral tritium- $\beta$  spectrum to determine the background rate. The optimal duration depends on the background rate, but can generally take up a sizable fraction (of order 30 percent) of the overall measurement time. [KAT05; Kle14].

- 
2. Near its endpoint, the shape of the integral tritium- $\beta$  spectrum depends most strongly on the neutrino mass. Hence, most measurement time should be attributed to this region [KAT05; Kle14].
  3. Retarding voltage bins deeper into the spectrum increase the count rate and hence, lower the statistical uncertainty due to Poisson statistics. These measurements mainly determine the endpoint from extrapolating the slope of the integral tritium- $\beta$  spectrum [KAT05; Kle14].
  4. The theoretical description of the integral tritium- $\beta$  spectrum is optimized for the endpoint region. E. g. the molecular final states for  $\beta$ -electron energies 40 eV below the endpoint would need further investigation [Dos+06]. Hence, deeper scans introduce modeling uncertainties. However, it is expected that continuous modeling efforts decrease these uncertainties as needed.

The KATRIN Design Report [KAT05] suggests five 3-year-long MTDs for different measurement ranges  $[E_0 - \alpha \text{ eV}, E_0 + 5 \text{ eV}]$  with  $\alpha \in \{20, 25, 30, 40, 50\}$  and the conclusion that  $\alpha = 30$  yields the best sensitivity to the neutrino mass.

As an energy-dependent effect is investigated within this thesis, it should be noted that scans beyond the 50 eV range have already been performed and may also be performed again in the future. E. g. searches for sterile neutrinos at the keV-scale would require deeper scans [Mer+19]. On top of that, within several measurement campaigns deeper scans were conducted: The First Tritium (FT) commissioning campaign successfully proved the apparatus functioning. The corresponding MTD covered a range starting at  $\sim E_0 - 1.6 \text{ keV}$ . The KATRIN neutrino mass measurement campaign 1 (KNM1) is being evaluated during the writing of this thesis. It set out to establish an unprecedented limit on the neutrino mass by  $\beta$ -decay measurements. Its MTD starts at  $\sim E_0 - 90 \text{ eV}$ , but the analysis range for neutrino mass inference remains still to be determined.

### 3.7. A Simulated KATRIN Neutrino Mass Measurement

In summary, a KATRIN measurement yields a set of electron counts  $\{N(qU_i)\}$ , equation (3.32), distributed over retarding voltage bins  $\{qU_i\}$ , where the counts fluctuate statistically [KAT05]. A possible model for the fluctuations is a Poissonian distribution [Kle14]. Figure 3.5 shows a KATRIN measurement for an MTD starting at  $E_0 - 30 \text{ eV}$  and a total measurement time of three years. The distortion of the measured integral rate by a non-vanishing neutrino mass can be seen approximately 4 eV below the endpoint  $E_0$ . This distortion can be used to infer the squared electron antineutrino mass from a KATRIN neutrino mass measurement. Chapter 4 presents corresponding statistical methods.

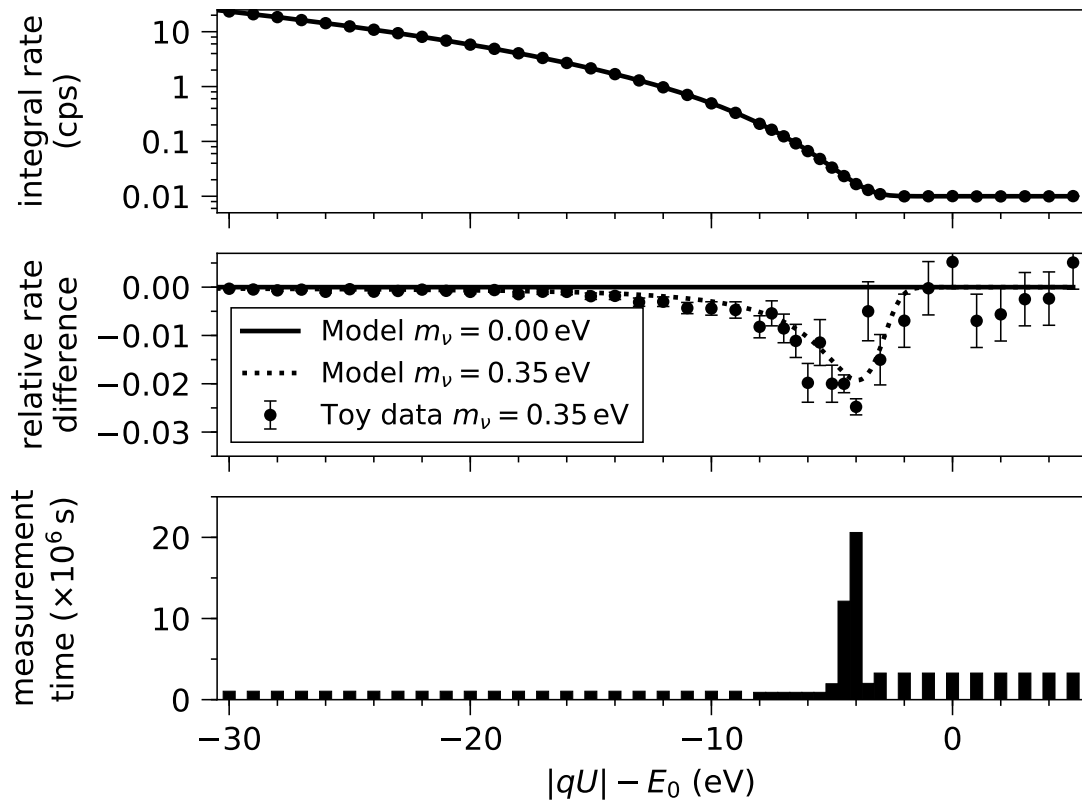


**Figure 3.5.: Simulated KATRIN measurement for a non-vanishing neutrino mass.** The total measurement time is three years. The top panel shows the measured integral rate  $\Gamma$  in dependence of the retarding energy. The center panel shows the relative rate difference for a non-vanishing neutrino mass  $\Gamma(m_\nu = 0.35 \text{ eV})/\Gamma(m_\nu = 0 \text{ eV}) - 1$ . The difference is  $\sim 2\%$  at a retarding energy approximately 4 eV below the endpoint (simulated as  $E_0 = 18575 \text{ eV}$ ). The bottom panel shows the MTD where most measurement time is attributed to the most sensitive region. This is also reflected by the uncertainty bars of the toy data. (Adapted from [Sei19].)



## 4. Statistical Methods and Neutrino Mass Inference at KATRIN

The best estimator for the neutrino mass  $m_\nu$  alongside with an uncertainty or an upper limit will be retrieved by comparing the output of the KATRIN measurement with theoretical predictions within the process of parameter inference. This chapter reviews a selection of statistical approaches suitable in relation to the KATRIN experiment.

Section 4.1 outlines the principle of the maximum likelihood estimator (MLE). Section 4.2 relates the principle of the MLE to a KATRIN measurement and neutrino mass inference. Section 4.3 introduces the formalism of a nominal neutrino mass fit at KATRIN. Section 4.4 reviews the concept of uncertainty intervals and how confidence intervals can be extracted from the likelihood. Section 4.5 introduces the software framework that was used within this thesis. Section 4.6 relates the principle of uncertainty to neutrino mass inference and explains the origin of the often quoted 200 meV (90 % C.L.) KATRIN sensitivity.

### 4.1. Maximum Likelihood Estimation

The likelihood is the probability of a measurement outcome given a hypothesis. A hypothesis depending on a parameter vector  $\boldsymbol{\theta}$  is called a composite hypothesis. A measurement outcome can be quantified by a vector of observed values  $\mathbf{x}$ . The probability  $P$  of  $\mathbf{x}$  given a hypothesis in dependence of  $\boldsymbol{\theta}$  is called the likelihood function [Tan+18]

$$L(\boldsymbol{\theta}) = P(\mathbf{x} \mid \boldsymbol{\theta}). \quad (4.1)$$

If  $p$  denotes the probability for one observed value  $x_i$  in  $\mathbf{x}$ , then the likelihood function can be written as a product [Tan+18]

$$L(\boldsymbol{\theta}) = \prod_i p(x_i \mid \boldsymbol{\theta}). \quad (4.2)$$

The parameter vector  $\hat{\boldsymbol{\theta}}$  that maximizes the likelihood function is called the maximum likelihood estimator (MLE) for the true values of  $\boldsymbol{\theta}$ .

### 4.2. The Likelihood of a KATRIN Measurement

The MLE-method can be applied to a KATRIN measurement as follows: The data vector is given by a set of  $n$  electron counts  $\{N_{\text{obs},i}\}$  measured at different retarding potentials  $\{qU_i\}$ . The hypothesis is that these counts follow a Poisson distribution with predicted expected electron counts  $\{N_{\text{theo},i}\}$  as per equation (3.32) [Kle14]. For sufficiently high counts ( $> 25$  [Kle+19]) the Poisson distribution can be approximated by a Gaussian distribution  $\mathcal{N}(x, \mu, \sigma)$  with mean  $\mu = N_{\text{theo},i}(\boldsymbol{\theta})$  and standard deviation  $\sigma = \sqrt{N_{\text{obs},i}}$ . The likelihood function then reads [Kle14]

$$L(\boldsymbol{\theta}) = \prod_i^n \mathcal{N}\left(x = N_{\text{obs},i}, \mu = N_{\text{theo},i}(\boldsymbol{\theta}), \sigma = \sqrt{N_{\text{obs},i}}\right). \quad (4.3)$$

Commonly, instead of maximizing the likelihood function, its negative logarithm is minimized and a factor 2 is introduced [Tan+18]. This yields

$$-2 \ln L(\boldsymbol{\theta}) = \chi^2(\boldsymbol{\theta}) = \sum_i^n \left( \frac{N_{\text{obs},i} - N_{\text{theo},i}(\boldsymbol{\theta})}{\sqrt{N_{\text{obs},i}}} \right)^2 + \text{constants}. \quad (4.4)$$

The minimization of equation (4.4) yields the MLE estimator  $\hat{\boldsymbol{\theta}}$  for  $\boldsymbol{\theta}$ .

Equation (4.4) is a sum of  $n$  standard normal distributed random variables. Hence, evaluated at the MLE, this chi-square expression  $\chi^2(\hat{\boldsymbol{\theta}})$  follows the Pearson's chi-square statistic with  $n - \dim \boldsymbol{\theta}$  degrees of freedom. Accordingly, the value  $\chi^2(\hat{\boldsymbol{\theta}})$  is a measure for the goodness-of-fit [Tan+18]. In conclusion, equation (4.4) can be used for neutrino mass inference via the maximum likelihood method.

### 4.3. A Nominal KATRIN Neutrino-Mass Fit

In regard to a KATRIN neutrino mass measurement, the parameter of interest in the parameter vector  $\boldsymbol{\theta}$  is the squared neutrino mass  $m_\nu^2$ . Furthermore,  $\boldsymbol{\theta}$  typically comprises the endpoint of the tritium- $\beta$  spectrum  $E_0$ , equation (3.6), an overall normalization factor for the  $\beta$ -electron counts  $A_S$  and the background rate  $\Gamma_{\text{bg}}$  [Kle14; KAT05], that are treated as nuisance parameters. For the latter two see equation (3.32). Hence, in order to infer the neutrino mass, the four-dimensional likelihood has to be minimized. Following this procedure with simulated data enables the determination of KATRIN's sensitivity (see subsequent section 4.6).

### 4.4. Uncertainty Intervals

The presented maximum likelihood method (section 4.1) provides point estimates  $\hat{\boldsymbol{\theta}}$ . However, additional information can be provided by interval estimates. There are two main approaches to statistical inference, which may be called Bayesian and frequentist [Tan+18]. They differ in their interpretation of probability, which becomes especially evident by the interval estimates associated with the two approaches: Credible and confidence intervals. Both interval types can be given with reference to quantiles of the Gaussian distribution. E.g. the 1- and 2- $\sigma$  levels define 68 % and 95 % intervals. The following two sections 4.4.1 and 4.4.2 explain the matter in more detail.

#### 4.4.1. Bayesian Credible Intervals

The likelihood  $L(\mathbf{x} | \boldsymbol{\theta})$  is a probability distribution for the data  $\mathbf{x}$  given the parameters  $\boldsymbol{\theta}$ . The likelihood can be transformed into a probability density for the parameters  $\boldsymbol{\theta}$  by multiplication with a prior distribution  $\pi(\boldsymbol{\theta})$  and normalization to one using Bayes theorem. One obtains the posterior distribution [Tan+18]

$$P(\boldsymbol{\theta} | \mathbf{x}) = \frac{L(\mathbf{x} | \boldsymbol{\theta})\pi(\boldsymbol{\theta})}{\int L(\mathbf{x} | \boldsymbol{\theta}')\pi(\boldsymbol{\theta}') d\boldsymbol{\theta}'}. \quad (4.5)$$

Credible regions, in which the true parameters lie with a certain probability can be extracted. When  $\boldsymbol{\theta}$  is one-dimensional a credible region is also called a credible interval.

#### 4.4.2. Frequentist Confidence Intervals

This section first gives definitions for the terms “confidence interval”, “coverage probability” and “confidence level”. It is explained, how confidence intervals can be extracted from a likelihood on the basis of these definitions. This approach was applied within the scope of

this thesis in order to study the impact of model uncertainties on KATRIN’s sensitivity in chapter 6.

In frequentist statistics, probability is interpreted as the frequency of the outcome of a repeatable experiment. The boundary of a confidence region is given by a function of the data. There is some freedom of choice for the corresponding function. It should be noted that in this sense, the term confidence region is somewhat “unqualified” [Tan+18]. But it obtains a deeper meaning in combination with a coverage probability. First, it should be noted that the boundary of the confidence region would fluctuate if one were to repeat the experiment many times. An ensemble of confidence regions would be obtained. The coverage probability  $\alpha$  refers to the fraction of confidence regions in such an ensemble that contains the true parameter values  $\boldsymbol{\theta}_T$  [Tan+18]. If an ensemble of confidence regions covers the true parameter values  $\boldsymbol{\theta}_T$  at least a fraction of  $\alpha$  times, the confidence interval is understood to have a confidence level of  $\alpha$  [Tan+18]. When  $\boldsymbol{\theta}$  is one-dimensional a corresponding confidence region is called a confidence interval.

In a practical context, a prescription is required on how to construct confidence intervals of a eligible confidence level. The Neyman construction [Ney37] or the unified approach by Feldman and Cousins [FC98] are such prescriptions.

A further method of constructing confidence intervals is to consider a test (see hypothesis testing in [Tan+18]) of the hypothesis that the parameter values  $\boldsymbol{\theta}$  have the true values  $\boldsymbol{\theta}_T$  [Tan+18]. In this construction the choice of test to be used is free. One possibility is a test statistic based on the likelihood ratio between the MLE  $\hat{\boldsymbol{\theta}}$  and  $\boldsymbol{\theta}$  [Tan+18]

$$\lambda(\boldsymbol{\theta}) = \frac{L(\boldsymbol{\theta})}{L(\hat{\boldsymbol{\theta}})}. \quad (4.6)$$

In the case of a construction via a hypothesis test, all parameter values  $\boldsymbol{\theta}$  are excluded from the confidence interval of level  $\alpha$  that are rejected by the test with a significance of  $\alpha$  [Tan+18].

If the likelihood follows the form of a multivariate Gaussian distribution in  $\boldsymbol{\theta}$ , then the above test statistic (4.6) can be evaluated and the hyper surface defined by

$$\ln L(\boldsymbol{\theta}) = \ln L(\hat{\boldsymbol{\theta}}) - \frac{s^2}{2} \quad (4.7)$$

encloses a  $s\sigma$  confidence region for  $\boldsymbol{\theta}$  [Tan+18]. (Here,  $s\sigma$  denotes the corresponding quantile of a Gaussian distribution.)

It should be noted that the extraction of confidence intervals from the KATRIN likelihood requires its extrapolation to nonphysical negative squared neutrino masses [Kle14] - a complication that can be avoided when using Bayesian methods.

In conclusion, in this section a constructive approach has been presented, that enables the extraction of confidence regions for the parameters of a KATRIN measurement from the KATRIN likelihood. An extension of this formalism (namely, the profile-likelihood method) finds application in the scope of this thesis in chapter 6.

## 4.5. The KaFit and SSC Software Frameworks

With respect to neutrino mass inference at KATRIN two formalisms have been presented: the model for a KATRIN neutrino mass measurement in chapter 3 and a statistical framework for parameter inference within the current chapter 4.

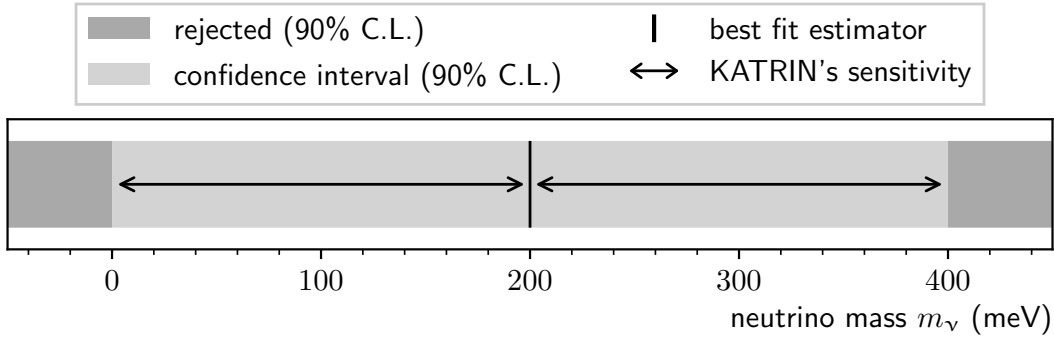


**Figure 4.1.: Illustration of KATRIN’s sensitivity to the neutrino mass.** The graph illustrates KATRIN’s sensitivity of 200 meV [KAT05] as per equation (4.8). It shows a hypothetical measurement of the neutrino mass with a symmetric confidence interval (90 % C.L.) centrally located around the best fit estimator. If such a classical confidence interval is constructed, KATRIN can reject the null hypothesis of a vanishing neutrino mass at 90 % C.L. if it estimates a neutrino mass of at least 200 meV.

The two formalisms are implemented within two modules of the “KATRIN Analysis and Simulations Package” (KASPER) [S-KAS]:

1. The **source and spectrum calculation (SSC)** [S-SSC] module implements the formulas for the differential and integrated spectrum calculations. Therefore, it follows the formulas given in chapter 3. Additionally, it also includes aspects beyond the given description, such as the gas dynamics within the WGTS [Höt12; Gro15; Kle+19; Käf12].
2. The **KaFit** [S-KF] module translates the  $\beta$  spectrum calculated by SSC into expected detector counts. Furthermore, KaFit implements several statistic tools tailored to the KATRIN experiment. One of which is the extraction of confidence intervals according to the profile-likelihood method (see section 4.4.2), which is of importance in the scope of this thesis. The actual minimization and profiling are done by the interfaced MINUIT2 [S-MIN] and MINOS package from the ROOT<sup>1</sup> [Ant+09] analysis framework [Kle14].

Both packages were used and extended to allow for the analysis done within the scope of this thesis as will be explained in chapters 5 and 6.

## 4.6. KATRIN’s Sensitivity to the Electron Antineutrino Mass

This section explains the origin of the often quoted KATRIN design sensitivity to the neutrino mass of 200 meV (90 % C.L.). First, a definition of the sensitivity is given in section 4.6.1. Then, section 4.6.2 and 4.6.3 show how this definition was applied by different works to deduce KATRIN’s sensitivity.

### 4.6.1. Definition and Construction of KATRIN’s Sensitivity

KATRIN’s sensitivity can be understood as half the width of a symmetric and central confidence interval (90 % C.L.) for the neutrino mass obtained from a KATRIN neutrino mass measurement. As such it can be constructed from a  $1-\sigma$  uncertainty  $\sigma(m_\nu^2)$  on the squared neutrino mass [KAT05]

$$S_{m_\nu}(90\%) = \sqrt{1.645 \cdot \sigma(m_\nu^2)}, \quad (4.8)$$

<sup>1</sup><http://root.cern.ch/>

**Table 4.1.: KATRIN's sensitivity to the neutrino mass from ensemble tests.**

The table lists KATRIN's sensitivity  $S_{m_\nu}$  (90 %) as defined by equation (4.8). Several works reevaluated the statistical uncertainty according to experimental and theoretical progress. For each reevaluation a systematic uncertainty of  $\sigma_{\text{sys}}(m_\nu^2) = 0.017 \text{ eV}^2$  was assumed. A value derived from an ensemble test is a random variable. Corresponding uncertainty intervals are reprinted where originally stated.

$\sigma_{\text{stat}}(m_\nu^2)$ (eV <sup>2</sup> )	$S_{m_\nu}$ (90 %) (meV)	comment	reference
0.018	200	design value	[KAT05]
$0.0165 \pm 0.0001$	198	updated $\beta$ -spectrum calculation	[Höt12]
$0.0162 \pm 0.0001$	197	further updated $\beta$ -spectrum calculation	[Kle14]
0.01490	193	optimized MTD	[Kle14]

where the factor 1.645 translates the 68.3 % interval into a 90 % interval.

In other words, KATRIN's sensitivity to the neutrino mass can be understood as the minimal neutrino mass that has to be inferred from a KATRIN neutrino mass measurement to exclude the null hypothesis of a vanishing neutrino mass [Kle14] when constructing a symmetric and central confidence interval (90 % C.L.). Figure 4.1 illustrates this statement.

For a more comprehensive picture, where not only a symmetric and central confidence interval is considered, but also the unified approach according to Feldmann and Cousins as well as Bayesian statistics, the reader is referred to [Kle+19].

#### 4.6.2. Sensitivity from Simulated Ensembles

In the KATRIN Design Report the sensitivity to the neutrino mass was evaluated using ensemble tests. An ensemble of many KATRIN measurements was simulated (see section 3.7 on how such a simulation can be conducted) with a true neutrino mass of 0 eV. From each simulated measurement the squared neutrino mass was inferred in a standard KATRIN four-parameter fit (see section 4.3). Probability was interpreted as the frequency of an outcome of such a fit. The central 1- $\sigma$  interval of the obtained ensemble of squared neutrino masses was taken as the statistical uncertainty on the squared neutrino mass [KAT05]

$$\sigma_{\text{stat}}^{\text{TDR}}(m_\nu^2) = 0.018 \text{ eV}^2 \quad (4.9)$$

A systematic uncertainty was estimated to be approximately 0.01 eV. Due to the early stage of the experiment the systematic uncertainty was conservatively enlarged to a systematic budget at approximately the same scale as the statistical uncertainty [KAT05]

$$\sigma_{\text{sys}}^{\text{TDR}}(m_\nu^2) = 0.017 \text{ eV}^2 \quad (4.10)$$

Adding the statistic and systematic uncertainty quadratically and applying the definition (4.8) yields KATRIN's design sensitivity [KAT05]

$$S_{m_\nu}^{\text{TDR}}(90 \%) = \sqrt{1.645 \cdot \sqrt{\sigma_{\text{stat}}^{\text{TDR}}(m_\nu^2)^2 + \sigma_{\text{sys}}^{\text{TDR}}(m_\nu^2)^2}} \approx 200 \text{ meV}. \quad (4.11)$$

The corresponding investigations were redone in the scope of several works. Table 4.1 lists selected results.

#### 4.6.3. Sensitivity from the Profile-Likelihood Method

In the scope of this thesis, the sensitivity on the neutrino mass as obtained by the profile-likelihood method is of importance. (See chapter 6 for a description and application of the profile-likelihood method.) In this regard, previous results from [Kle14] based on the

profile-likelihood method are shortly reviewed here. Two uncertainties were obtained for two different MTDs in a KATRIN standard 4-parameter fit (see section 4.3). The first MTD had been specially optimized with regard to KATRIN’s sensitivity and the resulting statistical uncertainty is  $\sigma_{\text{stat}}(m_\nu^2) = 0.01494 \text{ eV}^2$ . For the second result the nominal MTD from the KATRIN Design Report was used as introduced in section 3.6. The corresponding profile likelihood was plotted and  $\sigma_{\text{stat}}(m_\nu^2)$  can be extracted to be between  $0.0155 \text{ eV}^2$ – $0.0165 \text{ eV}^2$ . Both results are in agreement on the  $10^{-3}$  level with the results from ensemble tests (see [Kle14] in table 4.1). This is an indicator for the general validity of the profile-likelihood method in the context of a KATRIN measurement. A more detailed discussion on the matter is given in chapter 6.

# 5. Energy-Dependence of the Cross Section for Inelastic Electron Scattering within the WGTS

The probability of an electron to scatter when traveling through the WGTS can be characterized by the total scattering cross section  $\sigma_{\text{tot}}$ . Two types of scatterings can be distinguished: elastic and inelastic scattering. The cross section for elastic scattering is by smaller than the one for inelastic scattering by one order of magnitude [Kle+19]. This chapter focuses on inelastic scattering and neglects the other. Within this chapter, the cross section for electrons scattering inelastically off tritium molecules is just denoted as “cross section” and with the symbol  $\sigma$ . For ease of notation and reading, the adjective “inelastic” and an index such as “inel” is omitted where the context allows it unambiguously.

The cross section depends on the energy of the incident electrons:  $\sigma \equiv \sigma(E_{\text{kin}})$ . This dependence has been neglected in the formal modeling of a KATRIN measurement within the previous chapter 3. This chapter investigates effects related to the incorporation of the energy-dependence. Section 5.1 lists cross section values from different sources and relates them to each other. Section 5.2 extends the mathematical formalism for a KATRIN measurement in order to incorporate the energy-dependence of the scattering cross section. Section 5.3 discusses the energy-dependence within the context of neutrino mass inference. In the end, section 5.4 concludes and offers an outlook.

## 5.1. Cross Section for Electrons Scattering off Molecules of Hydrogen Isotopologues

There exist several sources for cross-section formulae and values. This section gives an overview about the sources considered in this thesis and how they relate to each other. First, the cross section for electrons with an energy of 18 600 eV scattering off tritium was measured at the Troitsk experiment to be [Ase+00]

$$\sigma(18\,600\,\text{eV}) = (3.40 \pm 0.07) \times 10^{-22} \text{ m}^{-2}. \quad (5.1)$$

Also, the KATRIN Design Report lists a reference value [KAT05]

$$\sigma_{\text{TDR}} = 3.456 \times 10^{-22} \text{ m}^{-2}. \quad (5.2)$$

Furthermore, there exist theoretical calculations of the cross section for electrons scattering off hydrogen molecules. In section 5.1.1 the theoretical formulae are reviewed. How the different sources relate to each other and what approach is chosen within the scope of this thesis is explained in section 5.1.2.

### 5.1.1. Theoretical Formulae

An expression for the inelastic cross section for electrons scattering off hydrogen molecules can be found in [Liu73]. Two expressions are given, one for relativistic incident electrons and one for non-relativistic incident electrons. With regard to KATRIN the energies of  $\beta$  electrons from tritium  $\beta$  decay are relevant. The maximum relativistic  $\beta$  factor of electrons from tritium  $\beta$  decay is

$$\beta(E_{\text{kin}}, m) = \sqrt{1 - \frac{1}{(\frac{E_{\text{kin}}}{m} + 1)^2}} \quad (5.3)$$

$$\Rightarrow \beta_{\text{max,T}} = \beta(E_0^{\text{eff}} \approx 18.6 \text{ keV}, m_e \approx 511 \text{ keV}) \approx 0.26. \quad (5.4)$$

Traveling at approximately a forth of the speed of light, the  $\beta$  electrons are assumed to behave non-relativistic. Then, the given expression for the energy-dependent cross section is [Liu73]

$$\sigma(E) = (4\pi a_0^2) \cdot \left(\frac{E}{R}\right)^{-1} \cdot \left[C_1 \cdot \ln\left(\frac{E}{R}\right) + C_2\right] \quad (5.5)$$

with the Bohr radius<sup>1</sup>  $a_0$ , the Rydberg energy<sup>2</sup>  $R$  and two constants  $C_1$  and  $C_2$ . The latter two depend on the hydrogen isotopologue. Different values are stated in different works for isotopic hydrogen

$$C_1 = 1.5487 \quad [\text{Liu73}] \quad (5.6a)$$

$$C_2 = 2.2212 \pm 0.0434 \quad [\text{Liu73}] \quad (5.6b)$$

$$C_2 = 1.53 \quad [\text{Ger75}] \quad (5.6c)$$

$$C_2 = 2.4036 \quad [\text{Liu87}]. \quad (5.6d)$$

The latest of these references [Liu87] acknowledges that the listed values for  $C_2$  are not compatible. Within this work, the value from [Liu87] is chosen as it is the most up-to-date of the listed ones.

In equation (5.5),  $E$  denotes<sup>3</sup>

$$E \equiv E(E_{\text{kin}}) = \frac{1}{2} m_e \beta^2(E_{\text{kin}}, m_e) \quad (5.7)$$

with  $\beta$  as in equation (5.3). Figure 5.1 shows the theoretical cross-section formula along with the measured value by the Troitsk experiment and the value from the KATRIN Design Report.

### 5.1.2. Relation to Former Works

As can be seen in figure 5.1, the cross section from the KATRIN Design Report does not match the theoretical calculations used in this thesis. However, the value stated in the KATRIN Design Report can be recovered from equation (5.5). If instead of the energy interpretation of equation 5.7, one applies the interpretation

$$E \equiv E_{\text{kin}}. \quad (5.8)$$

The obtained cross section is  $\sigma(E_{\text{kin}} \approx 18564.4 \text{ eV}) = 3.456 \times 10^{-22} \text{ m}^2$  as stated in the KATRIN Design Report where the energy 18564.4 eV is within the KATRIN design

<sup>1</sup>Bohr radius  $a_0 = 0.52917721067(12) \times 10^{-10} \text{ m}$  [Tan+18]

<sup>2</sup>Rydberg energy  $R = 13.605693009(84) \text{ eV}$  [Tan+18]

<sup>3</sup>I would like to thank F. Glück for pointing this out.

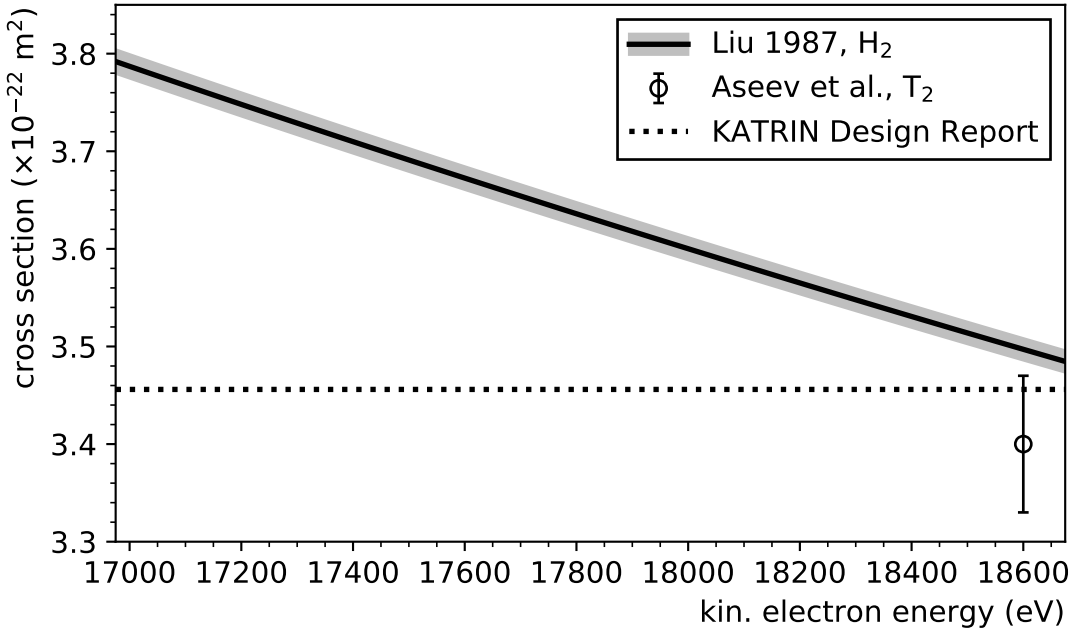


**Figure 5.1.: Inelastic cross section for non-relativistic incident electrons scattering off molecular hydrogen isotopologues.** Shown is the theoretical calculation according to equation (5.5) with constants from equation (5.6a) and (5.6d) where the latter is assumed to have an uncertainty according to equation (5.6b). Also shown is the measurement by [Ase+00] at the Troitsk experiment and the value stated in the KATRIN Design Report [KAT05]. The shown energy interval is chosen according to the MTD of the FT measurement campaign.

analysis interval (see section 3.6). This work applies the energy interpretation (5.8) when comparability to former work is of importance. Otherwise, interpretation (5.7) is used<sup>4</sup>. Corresponding indications are given. The quantitative difference of these two interpretations can be assessed by expanding the  $\beta$  factor (5.3) in the ratio  $E_{\text{kin}}/m_e \approx 18.575/511 \approx 0.036 \ll 1$

$$\beta^2 \approx 2 \frac{E_{\text{kin}}}{m_e} - 3 \left( \frac{E_{\text{kin}}}{m_e} \right)^2 \quad (5.9)$$

The energy interpretation of equation (5.7) then becomes

$$E(E_{\text{kin}}) \approx 0.95 E_{\text{kin}} \quad (5.10)$$

which is a shift in energy and hence in the cross section of about 5 % compared to the interpretation in (5.8). Exact calculations are given in the subsequent sections.

## 5.2. An Energy-Dependent Scattering Model within the KATRIN Formalism

The energy-dependence of the cross section enters into the calculation of the scattering probabilities (3.18). In the derivation, that is given in the previous section 3.2.4, the dependence on the starting energy  $E_S$  of electrons is neglected. Instead an average starting energy and hence, an average scattering cross section

$$\sigma(18\,564.374\,63\,\text{eV}) = 3.456 \times 10^{-22} \text{ m}^2 \quad (5.11)$$

<sup>4</sup>The cross sections obtained from the theoretical formula (5.5) applying the energy interpretation via equation (5.7) are in better agreement with recently taken data at KATRIN according to preliminary analysis results by dedicated subgroups of the KATRIN collaboration at the time of writing this thesis.

**Table 5.1.: Probabilities for severalfold scattering of electrons in the WGTS** averaged over all starting positions and starting pitch angles. Both, the values from a Monte Carlo (MC) simulation and the values according to equation (3.19) are given. The cross section was evaluated at an energy of  $E = 18\,564.374\,63$  eV for the two energy interpretations described by equation (5.8) and (5.7). Further input parameters to the calculations are a constant gas column density  $\rho d = 5 \times 10^{17} \text{ cm}^{-2}$ , a WGTS length of  $d = 10.0820 \text{ m}$  and a maximum acceptance angle of  $\theta_{\max} = 50.7685^\circ$ .

cross section ( $10^{-22} \text{ m}^{-2}$ ) →	3.456	3.456	3.673
source →	MC particle tracking [Gro15]	eq. (3.19) [Gro15; Kle14]	eq. (3.19)
scattering count ↓			
0	$0.415 \pm 0.002$	0.41334	0.39564
1	$0.292 \pm 0.002$	0.29266	0.28967
2	$0.166 \pm 0.001$	0.16733	0.17298
3	$0.079 \pm 0.001$	0.07913	0.08590
4	$0.031 \pm 0.001$	0.03178	0.03634

(energy interpretation as per equation 5.8) is assumed. Table 5.1 lists the corresponding scattering probabilities averaged over all starting positions and pitch angles of electrons. Additionally, the results of a Monte-Carlo simulation by [Gro15] and the values using the energy interpretation of equation (5.7) are given. How the energy-dependence of the scattering probabilities can be modeled is shown in section 5.2.1. Subsequently, section 5.2.2 discusses the presented model.

### 5.2.1. Model Description

Within this section, two models are presented in order to incorporate the energy-dependence of the scattering cross section into the mathematical formalism of a KATRIN measurement.

#### Poisson Model

An expression for the probability of  $l$ -fold scattering of electrons within the WGTS is derived in the previous section 3.2.4. The given model is independent of the energy of the electrons. Instead of using a constant cross section, the energy-dependence can be respected. The corresponding formulae from section 3.2.4 are repeated below, with the energy-dependence made explicit

$$\mu(E_S, z_S, \theta_S) = \frac{\sigma(E_S)}{\cos \theta_S} \int_{z_S}^{d/2} \rho(z) dz \quad (5.12a)$$

$$P_l(E_S, z_S, \theta_S) = \text{Poisson}(\mu(E_S, z_S, \theta_S), l) \quad (5.12b)$$

$$\bar{P}_l(E_S) = \frac{1}{d \cdot (1 - \cos(\theta_{\max}))} \int_{-d/2}^{d/2} \int_0^{\theta_{\max}} \sin(\theta_S) \text{Poisson}(\mu(E_S, z_S, \theta_S), l) d\theta_S dz_S. \quad (5.12c)$$

As a reminder,  $\bar{P}_l(E_S)$  in the final equation (5.12c) denotes the probability of  $l$ -fold scattering for a  $\beta$  electron with a starting energy  $E_S$  averaged over all starting positions and pitch angles. In the following, this model is denoted “Poisson model”. It is expected to be accurate for the probability of no scattering  $\bar{P}_0(E_S)$ . But, depending on the required accuracy, for one or more scatterings the Poisson model does not necessarily hold as explained in the following paragraph.

## Extended Model

A scattering electron loses energy. The scattering cross section increases with decreasing energies and the electron becomes more likely to scatter again. In other words, the probabilities of individual scattering processes are no longer independent when respecting the dependence on the electron energy. This violates one of the preconditions to model the scattering probabilities via a Poisson distribution. Another model is suggested that partly accounts for this fact (inspired by a model in [Gro15] that incorporates changes of the electron pitch angle due to scattering). It assumes a fixed energy loss per scattering. A descriptive derivation is given in appendix A. In this section it is labeled by

$$\bar{P}_l^*(E_S) \quad (5.13)$$

and it denotes the probability of  $l$ -fold scattering for a  $\beta$  electron with a starting energy  $E_S$  averaged over all starting positions and pitch angles assuming a fixed energy loss  $\epsilon$  per scattering. In the following, this model is denoted the “extended model”. The value  $\epsilon = 12.6$  eV was chosen as it is the most probable energy loss for electrons traveling through tritium gas (see figure 3.3). A more accurate description would incorporate the full energy loss function. This may be the subject of a future study.

The extended model was evaluated numerically as it includes one limit and two integrals (see appendix A.1). The numerical accuracy had to be good enough to decide whether it differs significantly from the Poisson model or not. At the same time, a balance between the numerical accuracy and the evaluation run time had to be found. The probability for one-fold scattering could be calculated with a numerical accuracy on the  $10^{-5}$  level (see appendix A.2 on how this value is derived and how it can be interpreted). However, the evaluation of the extended model for more than one scattering has not yet been done and may be the subject of a future study.

### 5.2.2. Model Discussion

Figure 5.2 shows the Poisson model along with the suggested extended model. The results are discussed in the following paragraphs.

#### Model compatibility

Table 5.1 lists the scattering probabilities for an energy-independent Poisson model (see section 3.2.4) and a reference cross section  $\sigma(E_{\text{kin}} \approx 18\,564.4 \text{ eV}) \approx 3.673 \times 10^{-22} \text{ m}$ . The energy-dependent Poisson model recovers the energy-independent model exactly at the corresponding energy as expected. For the probability of one-fold scattering the difference between the Poisson and the extended model is below  $10^{-4}$ . How this difference propagates to neutrino mass inference was not further investigated in the scope of this thesis, but may be the subject of a future study. The source and spectrum calculation (SSC) software framework, used by many former works (e.g. [Gro15; Kle14; Sei19]) evaluates the integrals within the scattering probabilities numerically with an accuracy of  $10^{-5}$ , which may serve as an indicator on to what extend the difference is of importance.

#### The Poisson Model as Probability Density

In the following, it is shown that the energy-dependent Poisson model  $\bar{P}_l(E_S)$  (see equation 5.12) resembles a probability density in  $l$  independent of a constant starting energy  $E_S$  of electrons because this can be used to explain further model properties. Accordingly, the two properties that have to be verified are

$$\forall E_S > 0 : \bar{P}_l(E_S) > 0 \quad (5.14)$$

$$\sum_l^{\infty} \bar{P}_l(E_S) = 1. \quad (5.15)$$

The first condition holds because all quantities in the calculation of  $\bar{P}_l(E_S)$  are positive. For the second condition, one can use that the Poisson distribution is a probability density that sums to one

$$\begin{aligned}\sum_l^{\infty} \bar{P}_l(E_S) &= \frac{1}{d \cdot (1 - \cos(\theta_{\max}))} \int_{-d/2}^{d/2} \int_0^{\theta_{\max}} \sin(\theta_S) \sum_l^{\infty} \text{Poisson}(\mu(E_S, z_S, \theta_S), l) d\theta_S dz_S \\ &= \frac{1}{d \cdot (1 - \cos(\theta_{\max}))} \int_{-d/2}^{d/2} \int_0^{\theta_{\max}} \sin(\theta_S) \cdot 1 d\theta_S dz_S \\ &= 1.\end{aligned}$$

This verifies that the Poisson model is a probability density in the amount of scatterings  $l$ .

### Trend of energy-dependence

As depicted in figure 5.2, for an increasing starting energy of electrons within the WGTS the probability for no and one-fold scattering also increases, while the probability for two-fold scattering decreases. This paragraph aims at giving an intuitive argument for this change of sign in the derivative  $d\bar{P}_l(E_S)/dE_S$  in the transition from  $l = 1$  to  $l = 2$ . First, the expected scattering count for an energy within the depicted range  $E_S \in [17 \text{ keV}, 18.6 \text{ keV}]$  of starting energies can be calculated numerically (the sum converges because  $\bar{P}_l(E_S)$  is a probability density as shown in the previous paragraph):

$$\bar{l}(17.0 \text{ keV}) = \sum_l^{\infty} \bar{P}_l(17.0 \text{ keV}) \cdot l \approx 1.23 \quad (5.16)$$

$$\bar{l}(18.6 \text{ keV}) = \sum_l^{\infty} \bar{P}_l(18.6 \text{ keV}) \cdot l \approx 1.14. \quad (5.17)$$

In other words, electrons with a starting energy between 17 keV and 18.6 keV are expected to scatter between 1 and 2 times on their way through the WGTS (averaged over all starting positions and pitch angles). Then, the illustrative chain-of-argument is the following:

- the starting energy  $E_S$  increases
- $\Rightarrow$  the scattering cross section decreases (see figure 5.1)
- $\Rightarrow$  scattering becomes less likely
- $\Rightarrow$   $\bar{l}$  moves closer to 1 and away from 2
- $\Rightarrow$  the probability for no and one-fold scattering increases,  
while the probability for more than one scattering decreases.

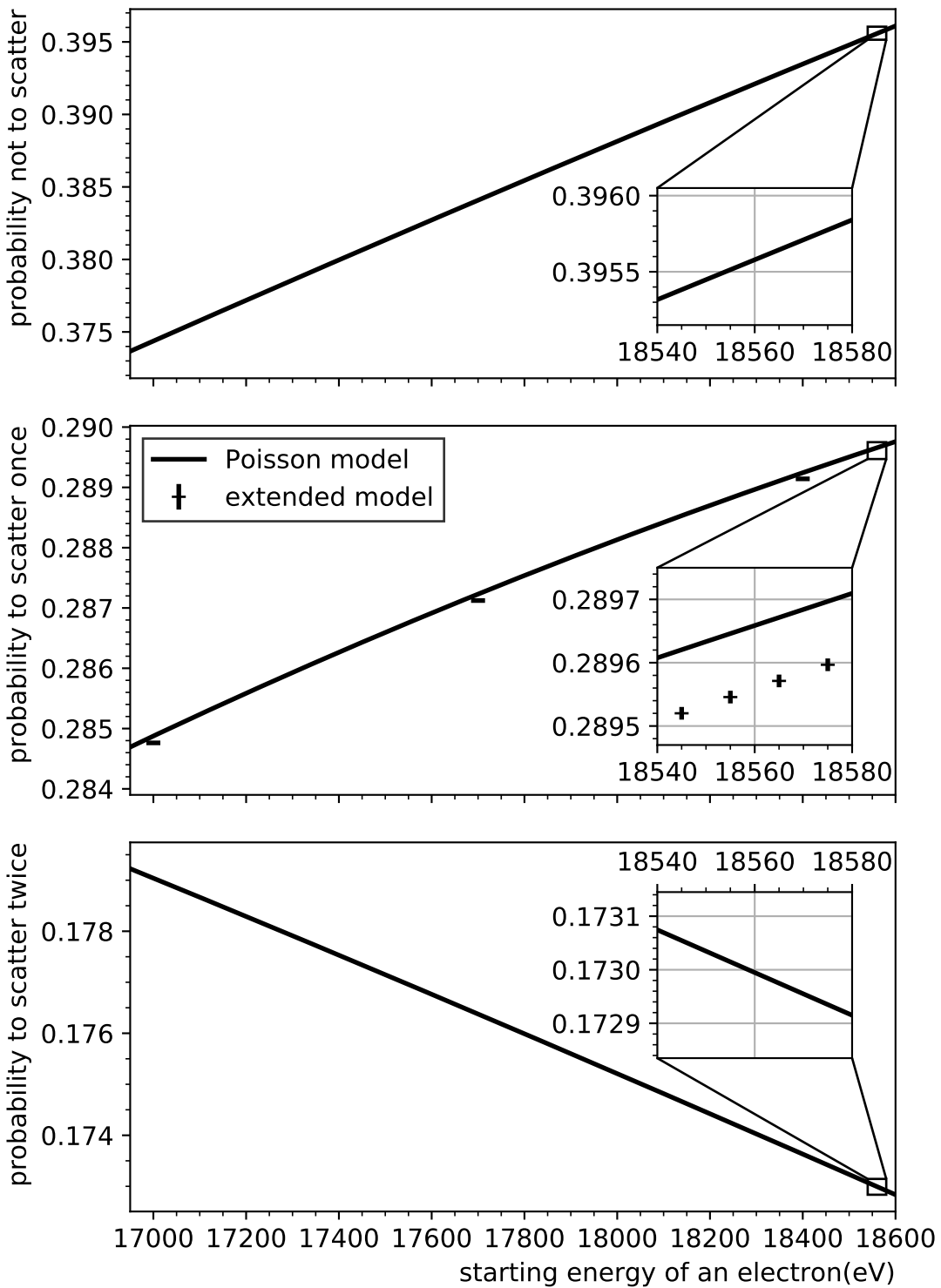


**Figure 5.2.: Energy-dependent probabilities for electron scattering within the WGTS.** Shown are from top to bottom the probability for no, one-fold and two-fold scattering averaged over all starting positions and starting pitch angles of electrons within the WGTS. The lines show the Poisson model and the markers the extended model (see main text for a description of the models). The extended model is only shown for one-fold scattering because for no scattering, it equals the Poisson model and for two-fold scattering it was not calculated (see appendix A for an explanation). The numerical evaluation of the extended model is subject to an uncertainty of  $\sim 10^{-5}$  (see appendix A.2), that is depicted as uncertainty bars. The shown energy range matches the measurement range of the First Tritium (FT) measurement campaign and the inset shows an energy span around the endpoint of the tritium  $\beta$  spectrum.

## Implementation and Performance

Within the scope of this thesis, the energy-dependent Poisson model of equation (5.12) was implemented into the SSC software framework. The extended model of equation (5.13) was not further investigated in this work. The energy-dependence of the scattering cross section may not be negligible in neutrino mass inference as is explained in the subsequent section 5.3. For that reason, the impact on the fitting run time by using an energy-dependent cross section was probed. Depending on the MTD, a fit might become slower by a factor of 40 to 120. This is due to the fact, that, when integrating over the energy loss in the response function in equation (3.29), the scattering probabilities have to be recomputed in every step of the numerical integration. It might be beneficial to investigate whether the evaluation can be speeded up in the future.

### 5.3. Effect on the Inferred Neutrino Mass

It was investigated how much the squared neutrino mass that is inferred from a KATRIN measurement would be shifted if the energy-dependence of the scattering cross section is neglected in the corresponding fitting procedure. The comparability to former results is of importance within this section. For that reason, the energy interpretation of equation 5.8 is used, which yields a cross section of  $\sigma_{\text{TDR}} = 3.456 \times 10^{-22} \text{ m}^{-2}$  [KAT05] within the KATRIN design analysis interval of 30 eV below the endpoint of the tritium  $\beta$  spectrum.

First, the results from a similar study in [Gro15] are reviewed because they might intuitively contradict the results presented in this thesis. Then, the results of this thesis are listed and an argument is given, why both sets of results are probably in accordance.

In [Gro15], it was investigated how much a constant offset of the cross section would shift the inferred squared neutrino mass if the offset were neglected in the analysis. A rule of thumb for the neutrino mass shift in dependence on the offset of the cross section  $\Delta\sigma$  is given [Gro15]

$$\frac{\Delta m_\nu^2(\sigma)}{10^{-3} \text{ eV}^2} = -0.45 - 1204 \cdot \frac{\Delta\sigma}{\sigma_{\text{TDR}}} \quad \text{with} \quad \sigma_{\text{TDR}} = 3.456 \times 10^{-22} \text{ m}^{-2}. \quad (5.18)$$

The difference between the cross section  $\sigma_{\text{TDR}}$  at an electron energy in the middle of the KATRIN analysis interval and the cross section at the interval's boundary energies can be determined using the energy-dependent formula for the cross section (5.5) with the energy interpretation of equation (5.8). Together with the rule of thumb (5.18) one obtains

$$\begin{aligned} |\Delta m_\nu^2(\sigma(18575 \text{ eV}))| &< 3 \times 10^{-3} \text{ eV}^2 \\ |\Delta m_\nu^2(\sigma(18545 \text{ eV}))| &< 3 \times 10^{-3} \text{ eV}^2. \end{aligned}$$

In contrast to the constant offset of the cross section investigated in [Gro15], in the scope of this thesis, an energy-dependent offset was investigated. A KATRIN neutrino mass measurement for a neutrino mass of 0 eV was simulated using an energy-dependent cross section<sup>5</sup>. A model that uses a constant cross section was fitted to the simulated spectrum. This procedure was repeated for the five different MTDs given in the KATRIN Design Report. Figure 5.3 shows the results. For the 30 eV measurement range, the difference from 0 eV respectively the shift of the squared neutrino mass is

$$\Delta m_\nu^2 = 1.09 \times 10^{-2} \text{ eV}^2. \quad (5.19)$$

---

<sup>5</sup>In the presented study, the simulated electron detector counts were substituted by their expectation values as opposed to fluctuated according to Poissonian statistics. For more details on such an Asimov data, see section 6.4.3.

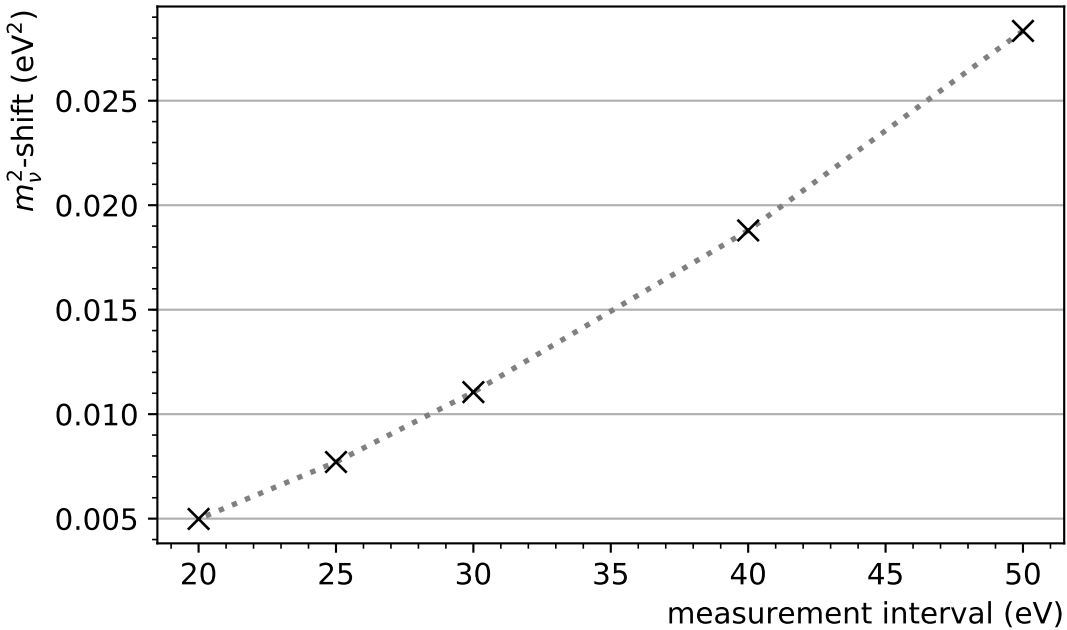


**Figure 5.3.: Shift of an inferred squared neutrino mass induced by a neglected energy-dependence of the inelastic scattering cross section.** The neutrino mass was inferred from data that was simulated using an energy-dependent inelastic scattering cross section as per equation 5.5 with the energy interpretation of 5.8 using a fit model that assumes a constant cross section of  $\sigma_{\text{TDR}} = 3.456 \times 10^{-22} \text{ m}^{-22}$ . The procedure was repeated for the five different MTDs given in the KATRIN design report.

This shift is larger than the one listed above under equation (??). This might be counterintuitive, but can be argued. The reason may be that the fit parameter for the signal amplitude  $A_S$  in a nominal KATRIN fit (see section 4.3) can compensate for a constant offset of the cross section. However, it may not compensate for an energy-dependent one. In order to verify this statement, two arguments are presented below. First, the study from [Gro15] was reproduced - once with a free fit parameter for  $A_S$  and once with  $A_S = 1$  fixed. The results are shown in figure 5.5. A cross section offset, that corresponds to the KATRIN design measurement range of 30 eV (refer to the caption of figure 5.5), yields a shift of the squared neutrino mass, that is larger by an order of magnitude with a fixed  $A_S$  as opposed to leaving  $A_S$  as a free parameter. The shifts are then compatible with the shifts of the study presented in this chapter.

The second plausibility argument is the following: Figure 5.5 shows the simulated integral rate for different cross section models normalized to the integral rate obtained by using the constant cross section  $\sigma_{\text{TDR}}$  from the KATRIN Design Report. The integral rates that are based on a model with a constant, energy-independent cross section differ from each other by almost ( $< 2 \times 10^{-4}$  level) a constant factor. This implies, when one of these models is used in a simulation of a KATRIN measurement and another model is used in a corresponding fit for neutrino mass inference, their difference can be compensated by the fit parameter for the signal amplitude  $A_S$ . However, the model, that uses an energy-dependent cross section, does not differ from the one with the constant cross  $\sigma_{\text{TDR}}$  section by a constant factor. The difference varies over the energy range. Such a difference can not be compensated by the fit parameter for the signal amplitude  $A_S$ .

These two presented arguments show that the results presented in this chapter and the ones in [Gro15] do not necessarily contradict each other.

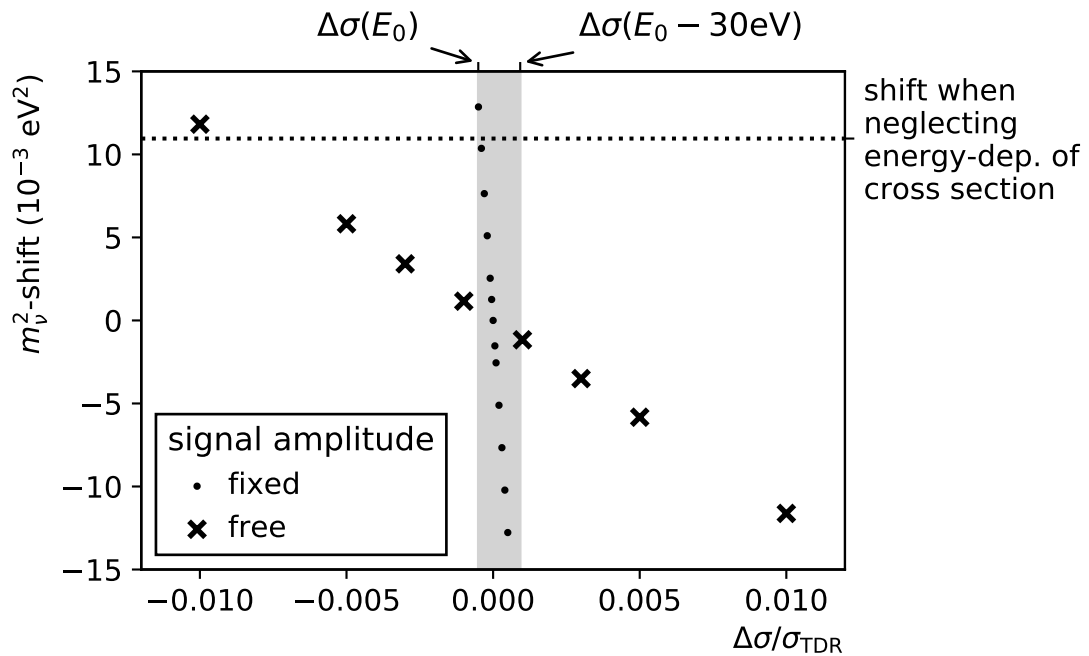


**Figure 5.4.: Shift of an inferred squared neutrino mass induced by a neglected offset of the inelastic scattering cross section.** The neutrino mass was inferred from data that was simulated using an inelastic scattering cross section of  $\sigma_{\text{TDR}} = 3.456 \times 10^{-22} \text{ m}^{-22}$ . The x-axis shows the relative offset of the inelastic scattering cross section assumed in the inference process. In an energy-dependent scenario, a cross section corresponds an energy of incident electrons as per equation (5.5). The cross section range, that corresponds the design KATRIN analysis interval of 30 eV is depicted as a gray band. The analysis was done twice: once with a free parameter for the signal amplitude, which reproduced the results given in [Gro15] (figure 6.31 on page 221); the second analysis had this parameter fixed. The shifts obtained with a fixed signal amplitude are compatible with the one obtained by neglecting the energy-dependence of the cross section within the 30 eV measurement interval.

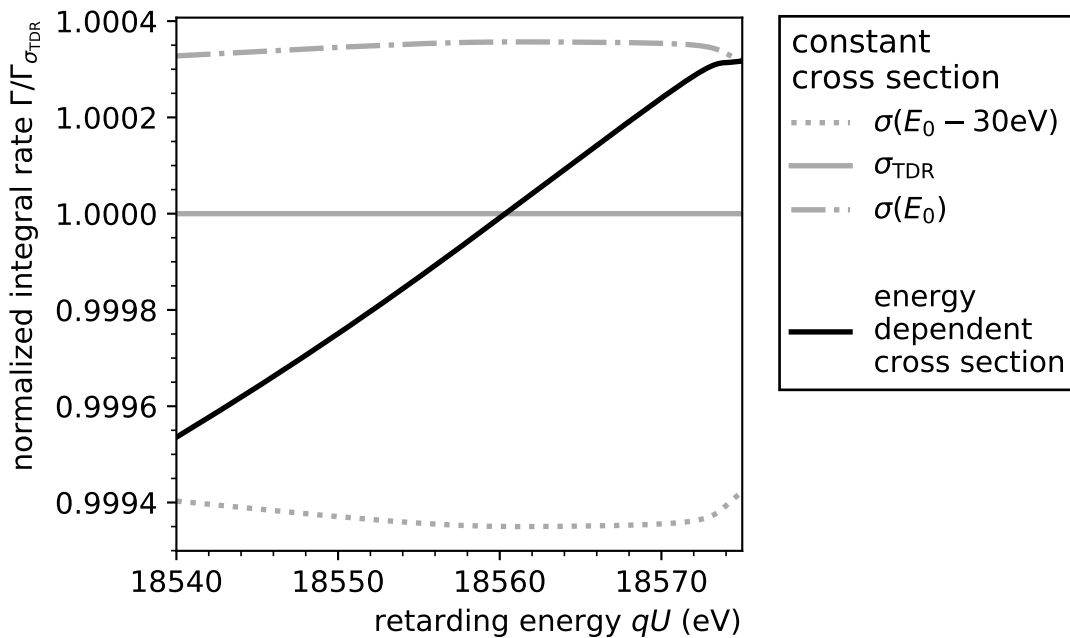


**Figure 5.5.: Simulated integral  $\beta$ -electron rate using different models of the cross section for inelastic electron scattering.** The x-axis shows the energy range of the design KATRIN analysis interval. The lines show the integral rate of  $\beta$  electrons for different models for the inelastic scattering cross section normalized to the model, that uses the constant cross section  $\sigma_{TDR} = 3.456 \times 10^{-22} \text{ m}^{-22}$ . The gray lines use a model with a constant cross section. The cross section values can be identified with electron energies as per equation (5.5) and the energy interpretation of equation (5.8) with  $\sigma(E_0 - 30 \text{ eV} = 18545 \text{ eV}) = 3.459 \times 10^{-22} \text{ m}^{-22}$  and  $\sigma(E_0 = 18575 \text{ eV}) = 3.454 \times 10^{-22} \text{ m}^{-22}$ . The black line shows the simulated integral rate for an energy-dependent cross section. This graph is meant to emphasize that the integral rates for models using a constant cross section differ by an almost constant factor, whereas the rate using an energy dependent cross section differs by a varying factor.

#### 5.4. Conclusion and Outlook

The energy-dependence of the scattering cross section enters into the calculation of the scattering probabilities. An accurate modeling of the energy-dependent scattering probabilities is challenging due to performance reasons, but modeling them according to a Poisson distribution is possible. It was shown that the difference between the Poisson model and a more accurate model for 1-fold scattering is on the  $10^{-4}$  level. The cases for more than 1 scatterings need further investigation. Also a fixed energy loss per scattering was assumed instead of a energy loss probability distribution. Future work might consider these aspects and what influence a more accurate modeling on the scattering probabilities has on the neutrino mass determination.

Given the KATRIN uncertainty budget, when modeling the energy-dependent scattering probabilities via a Poisson distribution, the energy dependence of the scattering cross section is not negligible for measurement intervals that extend more than 35 eV below the endpoint of the tritium  $\beta$  spectrum.

Including the energy dependence in the analysis increases the run time of the fitting procedure significantly. Future work might consider to precalculate the scattering probabilities for different fixed energies and use interpolation techniques for energies in-between the fixed ones.

# 6. Sensitivity Study using an Empirical Energy Loss Model Derived from KATRIN Data for Electrons Scattering Inelastically off Deuterium

A quantitative accurate description of the scattering processes of  $\beta$  electrons within KATRIN’s gaseous tritium source is of crucial importance for the neutrino-mass-sensitivity goal. In modeling the corresponding effects the energy loss function (see section 3.2.5) plays an important role. The KATRIN Design Report states that the precision of the energy loss functions from literature is not sufficient for the KATRIN-sensitivity goal. It was planned to deduce a sufficiently accurate model from data taken at KATRIN [KAT05]. In that regard, a preliminary model has successfully been established for electrons scattering off deuterium molecules based on data taken in October 2018 by a dedicated subgroup of the KATRIN collaboration. In the following this model is referred to as the “KATRIN model” or the “KATRIN energy loss model”. This preliminary energy loss model has partially-improved uncertainties with respect to the model from literature by [Ase+00] which was used in many previous works with regard to KATRIN [Gro15; Kle14; Kle+19; Sei19]. In the following, the latter model is referred to as the “Aseev model” after the primary author of the corresponding publication [Ase+00]. Additionally, the KATRIN model exhibits features not present in the Aseev model, but motivated by data (see section 6.2 and figure 6.1). Within the scope of this thesis the impact on KATRIN’s sensitivity by the exchange of the Aseev model for the KATRIN model was studied. Therefore, this chapter is structured as follows: Section 6.1 presents the general idea of this study. Section 6.2 outlines the KATRIN model. Section 6.3 discusses the scope of the validity of this study, for example what is expected of the comparison of a model for electrons scattering off deuterium and another model for scattering off tritium. Section 6.4 introduces the applied statistical tools. Section 6.5 lists and discusses the results. And section 6.6 concludes and offers an outlook.

## 6.1. Motivation and Introduction

As the energy loss function is a source of systematic uncertainties within neutrino mass inference, it is of importance to provide early feedback to the team that measures it. Beyond that, the implementation of the required statistical tools into the available software frameworks is of general interest as the approach taken in the scope of this thesis may be applied to other model uncertainties, not only to the ones stemming from the energy loss function.

For the conducted sensitivity study, KATRIN neutrino mass measurements were simulated assuming a neutrino mass of 0 eV and using the KATRIN energy loss model. A confidence interval for the neutrino mass was deduced using the profile-likelihood method as described in the subsequent section 6.4.2. This enables the treatment of the model uncertainties and

their correlations as nuisance parameters. This approach is repeated for the Aseev model to enable a comparison. Furthermore, the case where all parameters of the KATRIN model are fixed to their best estimates is also evaluated as a further comparison.

## 6.2. The Empirical KATRIN Energy Loss Model

The presented KATRIN energy loss model is a phenomenological description fitted to data taken at the KATRIN experiment in October 2018. It was established by a dedicated subgroup of the KATRIN collaboration. The model is outlined in the following.

### 6.2.1. Description

Figure 6.1 shows the KATRIN model in comparison to the Aseev model. They are not expected to be fully compatible within their uncertainties as they describe the scattering off two different hydrogen isotopologues. For a comparison of the presented KATRIN model with an energy loss model for deuterium from literature, the reader is referred to [Pre-Rod19]. Furthermore, the parametrization of the KATRIN model comprises a second peak for excitation and molecular dissociation of deuterium. As the KATRIN model is still in its early stages, this work refrains from a detailed physical interpretation and instead focuses on uncertainty propagation. For a more detailed physical interpretation the reader is referred to the KATRIN documents [Pre-Rod19; Pre-Han19-1; Pre-Han19-2]. With respect to the uncertainties, the KATRIN model shows an improved uncertainty in the ionization tail and also in large parts of the excitation peak. How this propagates within neutrino mass inference is investigated in this chapter.

### 6.2.2. Parametrization

In the preceding section 3.2.5, the energy loss function  $f_1(\epsilon)$  is introduced. It denotes the probability density for an energy  $\epsilon$  that an electron loses when scattering once (inelastically in the current context). The KATRIN model is such an energy loss function. It can be divided into two parts. The first part is the phenomenological description of the excitation peak region by the sum of three scaled Gaussian distributions  $\mathcal{N}_i$  ( $i \in \{1, 2, 3\}$ ). This part  $d\sigma_{\text{exit}}^{\text{phen}} / d\epsilon$  can be described by nine parameters  $\boldsymbol{\pi}_{\text{eloss}}$  which comprise the scales  $A_i$ , means  $m_i$  and standard deviations  $s_i$  of the three Gaussian distributions [Pre-Han19-2]

$$\boldsymbol{\pi}_{\text{eloss}} = (A_1, m_1, s_1, A_2, m_2, s_2, A_3, m_3, s_3)^T \quad (6.1)$$

$$\frac{d\sigma_{\text{exit}}^{\text{phen}}(\epsilon | \boldsymbol{\pi}_{\text{eloss}})}{d\epsilon} = \sum_{i=1}^3 A_i \cdot \mathcal{N}(\epsilon, \mu = m_i, \sigma = s_i). \quad (6.2)$$

The second part, the ionization tail, follows a modified version of the binary-encounter-dipole (BED) model. For a full formula, the reader is referred to [KR94]. Here, this part will be denoted

$$\frac{d\sigma_{\text{ion}}^{\text{BED}}(\epsilon)}{d\epsilon}. \quad (6.3)$$

The BED model is valid for hydrogen molecules. Therefore, it depends on the ionization energy of hydrogen. The corresponding value was exchanged for the one of deuterium  $E_{\text{ion},D_2} = 15.467 \text{ eV}$  [Shi+93]. Whether further modifications with regard to the difference in isotopologues are necessary is currently under investigation. Furthermore, the constant normalization factor of the BED model was removed for the following reason: The transition between the two parts, the phenomenological peak and the BED tail, is introduced at the ionization energy of deuterium  $E_{\text{ion},D_2}$ . In order for the transition to be continuous a scaling factor for the ionization tail is introduced

$$c = \left( \frac{d\sigma_{\text{exit}}^{\text{phen}}(E_{\text{ion},D_2} | \boldsymbol{\pi}_{\text{eloss}})}{d\epsilon} \right) \Bigg/ \left( \frac{d\sigma_{\text{ion}}^{\text{BED}}(E_{\text{ion},D_2})}{d\epsilon} \right). \quad (6.4)$$

Then, the full parametrization for the KATRIN model reads [Pre-Han19-1]

$$f_1^{\text{KATRIN}}(\epsilon \mid \boldsymbol{\pi}_{\text{eloss}}) = \begin{cases} \frac{d\sigma_{\text{exit}}^{\text{phen}}(\epsilon \mid \boldsymbol{\pi}_{\text{eloss}})}{d\epsilon} & \text{if } \epsilon \leq E_{\text{ion},D_2} \\ c \cdot \frac{d\sigma_{\text{ion}}^{\text{BED}}(\epsilon)}{d\epsilon} & \text{if } \epsilon > E_{\text{ion},D_2} \end{cases}. \quad (6.5)$$

### 6.2.3. Nuisance Parameters

The uncertainties of the KATRIN model as evaluated at the time of writing this thesis can be divided into two sets: The KATRIN model itself comprises nine parameters. However, it was obtained in a 15-parameter fit. The other six fit parameters are correlated with the parameters of the KATRIN model and hence are not necessarily negligible with regard to uncertainties. In the scope of this thesis they were incorporated in the statistical treatment of the uncertainties. Whether they may be neglected in future studies needs further investigation.

For a detailed description of the full fit of the KATRIN model to the recorded data, the reader is referred to [Pre-Han19-1], but a description of the essentials is given in the following. An overview of the used data sets is required in order to describe the further six fit parameters. Four integral spectra were recorded analogously to the described integral  $\beta$  spectrum in chapter 3, but with the electron gun (see section 2.3) as electron source instead of tritium. For each data set a different deuterium column density (see section 2.2) was set in the WGTS: 0 %, 15 %, 50 %, 100 % of the nominal column density of  $\rho d = 5 \times 10^{17}$  molecules/cm<sup>2</sup>. The fit model for the 15 %-measurement was rescaled with respect to the other measurements because the respective data set underwent a different preprocessing than the others. The corresponding scaling factor  $N_{\text{int},15}$  was a free fit parameter. A further scaling factor  $N_K$  for the KATRIN model was introduced in the fit as a free parameter in order for the whole KATRIN model to keep its properties of a probability density and integrate to unity. Additionally, a 5th data set recorded at 15 % column density in a time-of-flight mode [Bon+99] was fitted simultaneously. For each data set a different expected scattering count  $\mu_{\text{toto},15}, \mu_{\text{int},15}, \mu_{\text{int},50}, \mu_{\text{int},100}$  (see equation 3.17) was fitted, which adds four further parameters (there is no scattering for the 0 % measurement). In summary, the additional parameters in the fit of the KATRIN model are

$$\boldsymbol{\pi}_{\text{eloss+}} = (N_K, \mu_{\text{toto},15}, \mu_{\text{int},15}, \mu_{\text{int},50}, \mu_{\text{int},100}, N_{\text{int},15})^\top. \quad (6.6)$$

The best best-fit values, the standard deviations and the correlation matrix of the full 15-parameter set ( $\boldsymbol{\pi}_{\text{eloss}}$  and  $\boldsymbol{\pi}_{\text{eloss+}}$ ) can be found in appendix C. The aim of this chapter is to study the impact of the model uncertainties from these 15 parameters on KATRIN's sensitivity to the neutrino mass.

### 6.3. Scope of the Presented Analysis

This section lists considerations that should be kept in mind with regard to the study presented in this chapter.

First, it should be noted that the KATRIN model as presented is still preliminary and may be subject to change because the analysis of recent measurements is still ongoing.

Furthermore, during a neutrino mass measurement, the nominal tritium purity in the WGTS is planned to be above 95 % [KAT05]. Here, an energy loss model for deuterium is used. Two different, but similar energy loss models are expected for the two different gas species (compare [Abd+17] and [Ase+00]). Within the scope of this thesis, the impact on KATRIN's sensitivity from the reduction of uncertainties on the energy loss model are of primary

interest. As long as the KATRIN model for scattering off deuterium molecules is sufficiently similar to the model for scattering off tritium molecules, it is a plausible approach to use it for simulations of KATRIN neutrino mass measurements. (For the similarity, see figure 6.1.) In that regard, the results for KATRIN’s sensitivity derived in this chapter are expected to be meaningful at least as a proof of concept.

Furthermore, the KATRIN model does not yet incorporate systematic uncertainties. Corresponding efforts for their incorporation are made at the time of writing this thesis. A future version of the KATRIN model may exhibit larger uncertainties than the version used in this thesis.

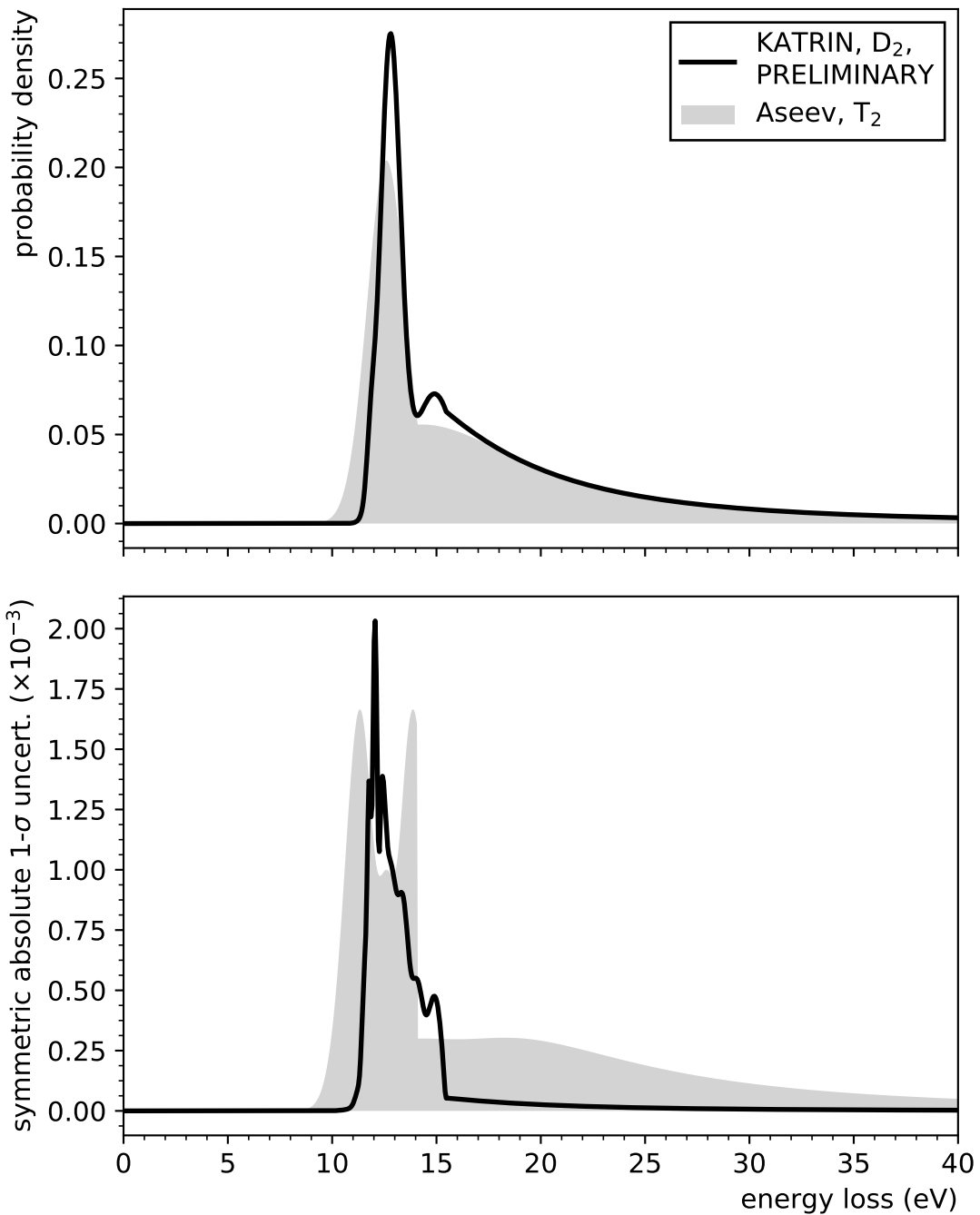


**Figure 6.1.: The preliminary KATRIN energy loss model for electrons scattering off deuterium molecules.** The black line shows the KATRIN energy loss model as established by a dedicated subgroup of the KATRIN collaboration for electrons scattering off deuterium molecules (KATRIN model). The corresponding model for scattering off tritium molecules as established by [Ase+00] (Aseev model) is shown for comparison as a shaded area. (That the latter is plotted as area instead of as a line solely serves readability as the two functions overlap strongly.) The top panel shows the probability densities of the energy loss and the bottom panel shows the corresponding absolute symmetric  $1-\sigma$  uncertainties. The uncertainties were obtained through uncertainty propagation via derivatives from the uncertainties of the model parameters (see figure 3.3 for the Aseev model and appendix C for the KATRIN model). Correlations are respected for the KATRIN model. However, there are no published correlations for the Aseev model. The KATRIN model shows particularly improved uncertainties in the ionization tail region in comparison to the Aseev model. (KATRIN model adapted from [Pre-Han19-1].)

## 6.4. Statistical Prerequisites

This section develops the statistical tools used in the scope of this thesis in order to evaluate the impact of the KATRIN energy loss model on KATRIN's sensitivity to the neutrino mass. The methods are described in a general manner (and could be applied to study model uncertainties in general) and then related to the KATRIN energy loss model. Section 6.4.1 presents a concept for the combination of a neutrino mass and a calibration measurement in parameter inference. Section 6.4.2 explains the profile-likelihood method for the treatment of nuisance parameters. And section 6.4.3 introduces the idea behind an Asimov data set and how it relates to ensemble testing.

### 6.4.1. Combination of a Calibration and a Neutrino Mass Measurements

If two measurements share a set of parameters  $\boldsymbol{\theta}_s$  and, additionally, have an individual set of parameters  $\boldsymbol{\theta}_1$  and  $\boldsymbol{\theta}_2$  and different sets of observations a combined likelihood  $L$  is given by the product of the likelihoods  $L_1$  and  $L_2$  of each measurement [Tan+18]

$$\begin{aligned} -2 \ln L(\boldsymbol{\theta}_s, \boldsymbol{\theta}_1, \boldsymbol{\theta}_2) &= -2 \ln L_1(\boldsymbol{\theta}_s, \boldsymbol{\theta}_1) - 2 \ln L_2(\boldsymbol{\theta}_s, \boldsymbol{\theta}_2) \\ &\equiv -2 \ln L_1(\boldsymbol{\theta}_{s,1}) - 2 \ln L_2(\boldsymbol{\theta}_{s,2}), \end{aligned} \quad (6.7)$$

where, for ease of notation, the combined parameter vectors  $\boldsymbol{\theta}_{s,1} \equiv (\boldsymbol{\theta}_s, \boldsymbol{\theta}_1)$  and  $\boldsymbol{\theta}_{s,2} \equiv (\boldsymbol{\theta}_s, \boldsymbol{\theta}_2)$  are introduced. In the scope of this thesis, it makes sense to identify the first measurement with a KATRIN neutrino mass measurement and the second with the measurement of the KATRIN energy loss model. In order to emphasize generality, this identification is postponed until the end of this section and the second measurement is called a calibration measurement throughout this section. Combining the likelihoods of a KATRIN neutrino mass and a calibration measurement incorporates the uncertainties of the latter into neutrino mass inference.

#### Approximated Combination of Likelihoods

For practicality, in this thesis, an approximation is applied: The calibration measurement is treated as evaluated independently (which is the case for the evaluation of the measurement of the KATRIN energy loss model). Hence, there are estimates  $\hat{\boldsymbol{\theta}}_{s,2}$ , and an estimated covariance matrix  $\hat{V}_{s,2}$  for the parameters of the calibration measurement. These can in turn be used to approximate the likelihood  $L_2$ . A choice that stands to reason for the approximation of  $L_2$  is a multivariate normal distribution  $\mathcal{N}$ . For the purpose of parameter inference through the maximum likelihood method  $-2 \ln L_2$  needs only to be accurately approximated within the contour, that is needed to extract confidence intervals. The choice of a multivariate normal distribution corresponds a symmetric approximation in second order of  $-\ln L_2$  around its minimum. The combined likelihood (6.7) then reads

$$\begin{aligned} -2 \ln L(\boldsymbol{\theta}_s, \boldsymbol{\theta}_1, \boldsymbol{\theta}_2) &\approx \chi^2(\boldsymbol{\theta}_{s,1}) - 2 \ln \mathcal{N}(\boldsymbol{\theta}_{s,2}, \hat{\boldsymbol{\theta}}_{s,2}, \hat{V}_{s,2}^{-1}) + \text{constants} \\ &= \underbrace{\chi^2(\boldsymbol{\theta}_{s,1})}_{(1)} + \underbrace{(\boldsymbol{\theta}_{s,2} - \hat{\boldsymbol{\theta}}_{s,2})^\top \hat{V}_{s,2}^{-1} (\boldsymbol{\theta}_{s,2} - \hat{\boldsymbol{\theta}}_{s,2})}_{(2)} + \text{constants} \end{aligned} \quad (6.8)$$

Here, (1) is the chi-square likelihood for a KATRIN neutrino mass measurement (see equation 4.4). And (2) resembles the negative log-likelihood of the calibration measurement approximated by a multivariate normal distribution. Terms having a form like (2) are also sometimes called “pull terms” because in the minimization of the likelihood they “pull” the parameters  $\boldsymbol{\theta}_{s,2}$  towards the corresponding values in  $\hat{\boldsymbol{\theta}}_{s,2}$ .

## Chi-Square Characteristics

The chi-square term (1) in (6.8) is assumed to be a sum of  $n$  standard normal distributed random variables as discussed in section 4.2. Hence, a likelihood only composed of the chi-square term (1) offers a goodness-of-fit criteria via the Pearson chi-square statistic. Whether the same criteria can be applied to the combined likelihood has to be investigated individually from case to case.

## Implementation in the KaFit Software Framework

The KaFit software module (see section 4.5) had allowed to use one-dimensional Gaussian “pull terms” (term (2) in equation 6.8). In the scope of this thesis the software was extended to allow for arbitrary dimensions with corresponding correlations by using a multivariate normal distribution. Albeit not of particular interest in this chapter, for completeness, the following shall be mentioned: By comparing equations (4.5) and (6.8) it becomes apparent that such “pull terms” take the same mathematical form as Bayesian priors. For that reason, further term forms apart from the multivariate normal distribution were implemented in order to be used as priors in a Bayesian analysis. For a documentation of the software features see appendix B.

## Application to the Energy Loss Model

With regard to the study presented in this chapter, the following identification can be made:  $\boldsymbol{\theta}_1$  comprises the parameter of a nominal four-parameter KATRIN neutrino mass fit (see section 4.3). Furthermore, the calibration measurement can be identified with the measurement of the KATRIN energy loss model  $\boldsymbol{\theta}_s = \boldsymbol{\pi}_{\text{eloss}}$ ,  $\boldsymbol{\theta}_2 = \boldsymbol{\pi}_{\text{eloss+}}$ ,  $\hat{\boldsymbol{\theta}}_s = \hat{\boldsymbol{\pi}}_{\text{eloss}}$ ,  $\hat{\boldsymbol{\theta}}_2 = \hat{\boldsymbol{\pi}}_{\text{eloss+}}$  (see equations 6.1 and 6.6 for  $\boldsymbol{\pi}_{\text{eloss}}$  and  $\boldsymbol{\pi}_{\text{eloss+}}$ ) and the corresponding estimator for the covariance matrix  $\hat{V}_{s,2} = \hat{V}_{\text{eloss},\text{eloss+}}$ . The numerical values for the three estimators can be found in the form of the means, the standard deviations and the correlation matrix in appendix C. In the same manner, the calibration measurement could instead be identified with the measurement of the Aseev model  $\boldsymbol{\theta}_s = (A_1, A_2, \epsilon_2, \omega_1, \omega_2)^\top$  without additional nuisance parameters  $\dim \boldsymbol{\theta}_2 = 0$  and a diagonal estimated variance matrix  $\hat{V}_{s,2} \equiv \hat{V}_{\text{Aseev}}$ . See equation (3.21) for the meaning of the parameters of the Aseev model and see the caption of figure 3.3 for their values.

### 6.4.2. Nuisance Parameters and the Profile-Likelihood Method

Apart from the parameters of interest  $\boldsymbol{\theta}$ , the KATRIN likelihood can depend on further nuisance parameters  $\boldsymbol{\pi}$ . With regard to the study presented in this chapter, the parameter of interest is the squared neutrino mass and the nuisance parameters are the further three parameters of a nominal four-parameter KATRIN neutrino mass fit as well as the parameters of the energy loss model (KATRIN or Aseev). The dimensionality (15+4 parameters in the case of the KATRIN model in a nominal KATRIN neutrino mass fit) may cause long run times when deriving a confidence region for the combined parameter set. Furthermore, as indicated by the naming conventions, the dimensions of the nuisance parameters in the confidence region are not of interest. Hence, in order to construct a confidence interval with just one dimension, a test statistic, similar to the one in equation 4.6, but solely depending on the parameters of interest, has to be found. The following paragraph outlines, how a corresponding test statistic can be constructed using the profile-likelihood method.

First, the profile likelihood is defined. It only depends on the parameters of interest  $\boldsymbol{\theta}$  and is independent of the nuisance parameters  $\boldsymbol{\pi}$ . Its values correspond the likelihood values evaluated at  $\boldsymbol{\theta}$  in the dimensions of the parameters of interest and maximized in the dimensions of the nuisance parameters [Tan+18]

$$L_p(\boldsymbol{\theta}) = L(\boldsymbol{\theta}, \hat{\boldsymbol{\pi}}(\boldsymbol{\theta})) , \quad (6.9)$$

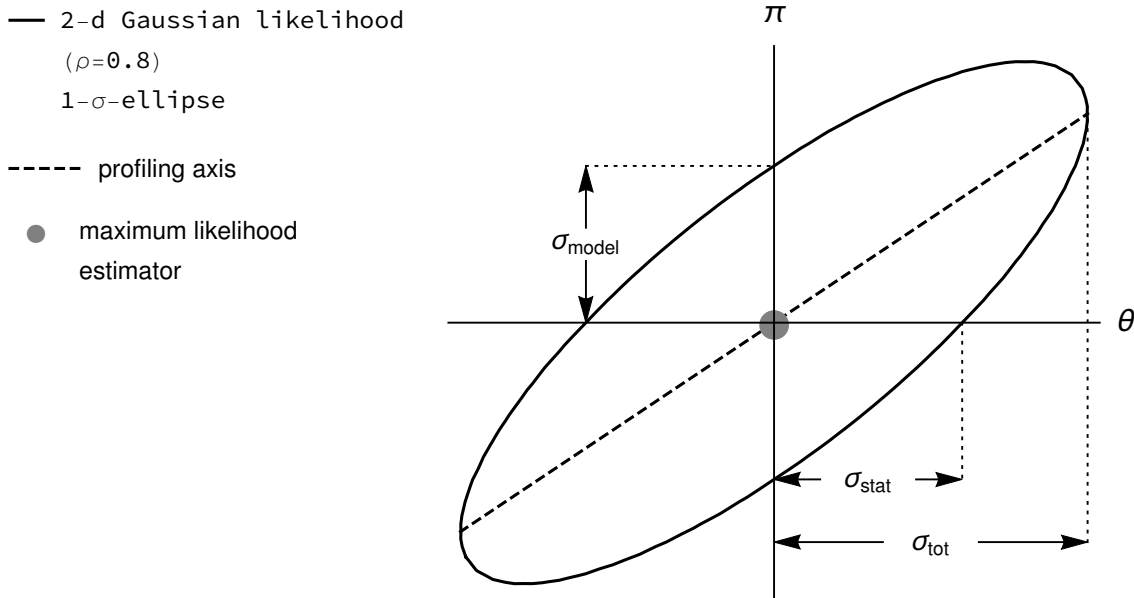


**Figure 6.2.: Illustration of the profile-likelihood method.** The graph illustrates the extraction of a confidence interval from the likelihood in a two-dimensional scenario, where there is only one nuisance parameter  $\pi$  and one parameter of interest  $\theta$ . The graph is a contour plot of an exemplary two-dimensional likelihood of Gaussian shape with a correlation between  $\pi$  and  $\theta$  of  $\rho = 0.8$ . The contour encloses a  $1\sigma$ -confidence region as per equation (4.7). Its width in the dimension of  $\pi$  is indicated as “model”-uncertainty with reference to an uncertainty stemming from a model established by a calibration measurement as described in section 6.4.1. The width in the dimension of  $\theta$  stems from the statistical uncertainty. The dashed line contains the points  $(\theta, \hat{\pi}(\theta))$  as per equation (6.10). It always intersects the contour at the point furthest right and left in the dimension of  $\theta$  independently of  $\rho$ ,  $\sigma_{\text{stat}}$  and  $\sigma_{\text{model}}$ . The point of intersection determines  $\sigma_{\text{tot}}$ . For example MINOS of the ROOT software framework is an algorithm that numerically tries to find the intersection of the dashed line and the contour [S-MIN]. Under the conditions stated in the main text, the interval of width  $2 \cdot \sigma_{\text{tot}}$  on the  $\theta$  axis around the maximum likelihood estimator is per construction a confidence interval (68 % C.L.) for the true value of  $\theta$ . A feature that can intuitively be deduced from the graph is the following: No matter how much  $\sigma_{\text{model}}$  is reduced, the total uncertainty  $\sigma_{\text{tot}}$  can never shrink below  $\sigma_{\text{stat}}$ . Likewise, whether a longer measurement, that decreases  $\sigma_{\text{stat}}$ , can improve  $\sigma_{\text{tot}}$  depends on  $\sigma_{\text{model}}$  and the correlation  $\rho$ .

where the double-hat indicates the maximization respectively the “profiling”. Also, the profile-likelihood ratio can be defined [Tan+18]

$$\lambda_p(\boldsymbol{\theta}) = \frac{L_p(\boldsymbol{\theta})}{L_p(\hat{\boldsymbol{\theta}})} . \quad (6.10)$$

According to Wilks’ theorem [Wil38], the distribution of  $-2 \ln \lambda_p(\hat{\boldsymbol{\theta}})$ , where  $\hat{\boldsymbol{\theta}}$  is the MLE (see section 4.1), approaches a chi-square distribution in the limit of a large data sample, independently of the values of the nuisance parameters  $\pi$  [Tan+18]. Hence, the profile-likelihood ratio offers a test statistic, from which a confidence interval for the parameters of interest can be derived. In other words, the profile-likelihood method is a constructive approach on how to derive a confidence interval. Whether all the conditions are met for its application to be valid can either be verified by a theoretical argument or put to the test. For the latter, many experiments can be simulated. The application of the profile-likelihood method then yields an ensemble of confidence intervals. How many of them cover the simulation truth determines the confidence level of the confidence interval. This approach is chosen in the scope of this thesis.

Figure 6.2 illustrates the profile-likelihood method for the case where  $\theta$  and  $\pi$  are one-dimensional.

#### 6.4.3. Ensemble Tests in Relation to an Asimov Data Set in Sensitivity Studies

If one were to repeat the KATRIN experiment many times, one would obtain an ensemble of confidence intervals for the neutrino mass (see section 4.4.2 about confidence intervals and also see table 4.1 with sensitivity studies from former works where the statistical portion of the sensitivity is listed with an uncertainty, which implies a distribution of statistical uncertainties). KATRIN's sensitivity can be deduced from a confidence interval (see section 4.6.1 about KATRIN's sensitivity). In that sense, if many KATRIN measurements are simulated, one also obtains an ensemble respectively a distribution of sensitivities. One way to obtain this distribution is to simulate many KATRIN neutrino mass measurements and fluctuate the measured electron counts according to Poissonian statistics (or Gaussian statistics as an approximation). The expectation value for KATRIN's sensitivity can than be extracted from the obtained distribution. This approach was for example applied within the scope of the KATRIN Design Report [KAT05]. It should be noted that such a distribution of sensitivities is narrow compared to its expectation value (see for example table 4.1 where the spread of the statistical uncertainty on the squared neutrino mass is smaller than the mean value by three orders of magnitude).

Instead of simulating many experiments, the median of KATRIN's sensitivity might be obtained from one simulation. Simulating a KATRIN neutrino mass measurement can be time-consuming depending on its level of detail. In that regard, using only one simulation is more practical. The median for KATRIN's sensitivity might be retrieved from one simulation, by replacing the electron count rates with their expectation value instead of fluctuating them according to Poissonian statistics [Cow+11]. This reasoning is based on Walt's theorem [Wal44]. Such a simulated data set is called an Asimov<sup>1</sup> data set. However, whether Walt's theorem is applicable may be hard to verify without doing an ensemble test, which would nullify its practicality here.

In the scope of this thesis, both approaches, using an Asimov data set and simulating an ensemble, were applied. The outcome verifies that an Asimov data set would be representative in the study presented in this chapter and indeed yields the median sensitivity.

### 6.5. Results

This section lists the results of the study on the impact from the uncertainties of the KATRIN model on KATRIN's sensitivity. The results are compared to the impact of the uncertainties from the Aseev model. The sensitivity study was conducted using a mathematical model of a KATRIN neutrino mass measurement as described in chapter 3 using a nominal configuration according to the KATRIN Design Report [KAT05] with a neutrino mass of 0 eV and a measurement time of three years. Correspondingly, the SSC and KaFit modules were used (see section 4.5). The full configuration of the study can be found in appendix D. The uncertainties of the KATRIN respectively the Aseev model were respected as described in section 6.4.1 about the combination of a neutrino mass and a calibration measurement. The confidence interval for the squared neutrino mass was extracted via the profile-likelihood method as described in section 6.4.2.

Section 6.5.1 presents the study using an Asimov data set. And section 6.5.2 presents the same results as obtained through an ensemble test (for the relation of these two approaches see section 6.4.3).

---

<sup>1</sup>The name of the Asimov data set is inspired by the short story “Franchise”, by Isaac Asimov. In the story, elections are held by selecting the single most representative voter to replace the entire electorate [Cow+11].

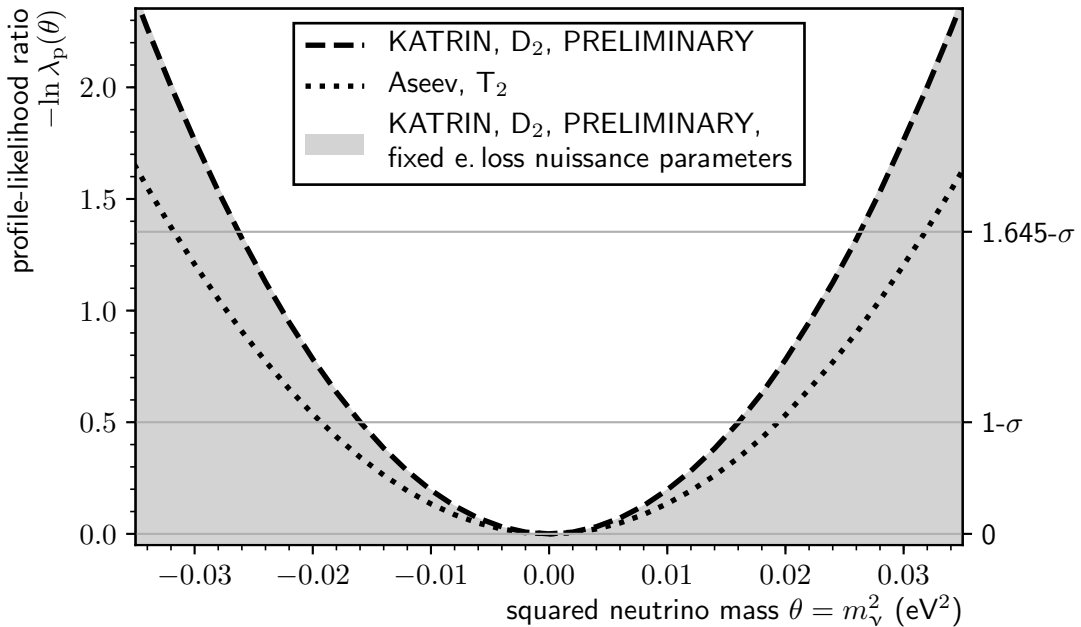


**Figure 6.3.: Profile-likelihood ratio from an Asimov data set.** The graph shows the profile-likelihood ratio  $\lambda_p$  for three models with different uncertainties: the KATRIN model (dashed line), the Aseev model (dotted line) and “statistics only” (shaded area). For a description of the different cases, the reader is referred to the main text. (That the “statistics only” case is plotted as area instead of as a line solely serves readability because a line would overlap with the line for the KATRIN model.) The MLE recovers the true simulated neutrino mass of 0 eV with a corresponding likelihood ratio of 0. The horizontal  $s\sigma$  lines are drawn at  $s^2/2$  as per equation (4.7). Their intersections with  $\lambda_p$  mark the confidence intervals for the neutrino mass at 68 % respectively 90 % confidence level. The width of the two intervals indeed relate through the factor 1.645 due to the parabolic shape of  $\lambda_p$ . It is apparent, that the uncertainties of the KATRIN model are negligible with respect to the “statistics only” case. The corresponding profile likelihoods are almost equal.

### 6.5.1. Sensitivity from an Asimov Data Set

The following three cases were investigated using an Asimov data set:

1. The simulation- and fit-model use the KATRIN energy loss model, but it was assumed to be without uncertainties. In other words, only the four parameters of a nominal KATRIN-neutrino-mass fit (see section 4.3) were treated as free parameters and the parameters of the KATRIN energy loss model were fixed to their best estimates. In the following, this is referred to as the “statistics only” case.
2. The simulation- and fit-model use the KATRIN energy loss model, and all its parameters were treated as free parameters in order to incorporate the uncertainties of the KATRIN model, which results in a 19-parameter fit.
3. The simulation- and fit-model use the Aseev model, and all its parameters were treated as free parameters in order to incorporate the uncertainties of the Aseev model, which results in a nine-parameter fit.

Figure 6.3 shows the corresponding profile-likelihood ratios and table 6.1 lists the extracted confidence intervals and obtained sensitivities. The “statistics only” case can be compared to the results listed in table 4.1. Here, a  $\sim 4 \times 10^{-4} eV^2$  smaller statistical uncertainty on

**Table 6.1.: Confidence intervals and sensitivities obtained from an Asimov data set.** The table lists values that can be extracted from the profile-likelihood ratio depicted in figure 6.3 for the three conducted studies: the “statistics only” case and respecting the uncertainties from the KATRIN and the Aseev model. Listed are the lower bound of the confidence interval (60 % C.L.) on the squared neutrino mass  $l(m_\nu^2)$ , the upper bound  $u(m_\nu^2)$ , half the width of the interval  $\sigma_{\text{tot}}(m_\nu^2)$  and KATRIN’s sensitivity on the neutrino mass as per equation (4.8). For the calculation of the sensitivity an additional systematic budget of 0.017 eV<sup>2</sup> was included (see section 4.6.2).

	$l(m_\nu^2)$ (10 <sup>-2</sup> eV <sup>2</sup> )	$u(m_\nu^2)$ (10 <sup>-2</sup> eV <sup>2</sup> )	$\sigma_{\text{tot}}(m_\nu^2)$ (10 <sup>-2</sup> eV <sup>2</sup> )	$S_{m_\nu}$ (90 %) (meV)
“statistics only”	-1.586	1.592	1.589	196
KATRIN model	-1.598	1.604	1.601	196
Aseev model	-1.931	1.939	1.935	206

the squared neutrino mass is obtained compared to the results by [Kle14; Höt12]. This is mainly due to the fact, that in the study presented in this chapter a detection efficiency of 95 % was used, whereas the other works used 90 %.

Under the restrictions listed in section 6.3, the following conclusions can be drawn:

- Using the KATRIN model at its current stage yields an improvement of 10 meV in sensitivity to the neutrino mass compared with the Aseev model.
- The uncertainties stemming from the KATRIN model are negligible with respect to the statistical uncertainty.
- The logarithm of the profile-likelihood ratio has a parabolic shape, which translates to a Gaussian shape for the likelihood. This hints at the applicability of Wilk’s theorem to verify the usage of the profile-likelihood method and Walt’s theorem to enable the usage of an Asimov data set. It also justifies the usage of the factor 1.645 to convert a confidence interval of 68 % confidence level into one of 90 %.

### 6.5.2. Cross-Check and Extension of the Asimov Data Set via Ensemble Testing

An ensemble of 4046 KATRIN neutrino mass measurements with a true neutrino mass of 0 eV was simulated using the KATRIN energy loss model and incorporating its uncertainties in the same manner as for the Asimov data set described in the last section 6.4.3. Several aspects were investigated as listed below:

#### Test of Coverage

The extraction of a confidence interval via the profile-likelihood method as done in the previous section 6.4.3 for the Asimov data set should per construction yield a coverage probability of 68.2 %. But if all conditions are met for this to hold has to be justified. Either a theoretical argument can be given or it can simply be put to the test. In the scope of this thesis the approach per test was chosen. In other words, 68.2 % of the obtained confidence intervals in the conducted ensemble test should cover the true simulated neutrino mass of 0 eV. The obtained coverage is 67.6 % as illustrated in figure 6.4. The slight undercoverage on the 10<sup>-3</sup> scale may stem from a limited ensemble test size. The difference is negligible within the typical rounding scheme to integer values for percentages in confidence levels.

### Chi-Square Characteristics

The combined likelihood of a neutrino mass and a calibration measurement evaluated at the MLE  $-2 \ln L(\hat{\theta})$  might not follow the chi-square statistic as mentioned in section 6.4.1. Figure 6.5 shows the obtained distribution of  $-2 \ln L(\hat{\theta})$  in the conducted ensemble test. An MTD with 41 retarding potentials was used. Hence, there are 41 summands in the likelihood for the KATRIN neutrino mass measurement. In the combined likelihood there are additional 15 summands to approximate the likelihood of the measurement of the KATRIN energy loss model. In total there are 19 fit parameters, four for the nominal KATRIN neutrino mass fit (see section 4.3) and 15 in order to incorporate the uncertainties of the KATRIN model. Thus, the hypothesis stands to reason that the obtained distribution follows a chi-square distribution with  $41 + 15 - 19 = 37$  degrees of freedom. A corresponding Kolmogorov–Smirnov test yields a  $p$ -value of  $p = 6 \times 10^{-6}$ . In other words, this hypothesis has to be rejected with a significance of  $5\sigma$ . Repeating the test for 38 respectively 39 degrees of freedom yields  $p = 0.14$  respectively  $p = 1 \times 10^{-14}$ . Hence, a chi-square distribution of 38 degrees of freedom can not be rejected at a significance of  $\alpha = 5\%$ . This is important because it means that the chi-square statistic can not necessarily be used as a measure for goodness-of-fit when incorporating the uncertainties of the KATRIN energy loss model into the neutrino mass inference in the way described in this thesis. Or, at least, one has to be careful about the choice of degrees of freedom. However, it must be emphasized that here the likelihood of the measurement of the KATRIN energy loss model is approximated by a multivariate normal distribution and thus does not fluctuate in the presented ensemble test. For the result to have full validity, the measurement of the KATRIN energy loss model has to be simulated along with the KATRIN neutrino mass measurement. This may be the aim of a future analysis.

### Representative Qualities of the Asimov Data Set

The estimated mean and standard deviation of the distribution of the confidence intervals (68 % C.L.) as obtained by the ensemble test is  $\hat{\sigma}_{\text{tot}}(m_\nu^2) = (1.599 \pm 0.013) \times 10^{-2} \text{ eV}^2$  in agreement with the one obtained through the Asimov data set in table 6.1. Furthermore, the median confidence interval  $\tilde{\sigma}_{\text{tot}}(m_\nu^2) = 1.598 \times 10^{-2} \text{ eV}^2$  should recover the one of the Asimov data set [Cow+11], which is indeed the case on the  $10^{-5} \text{ eV}^2$  level. This verifies the Asimov data set as representative for the study on the KATRIN energy loss model presented in this chapter.

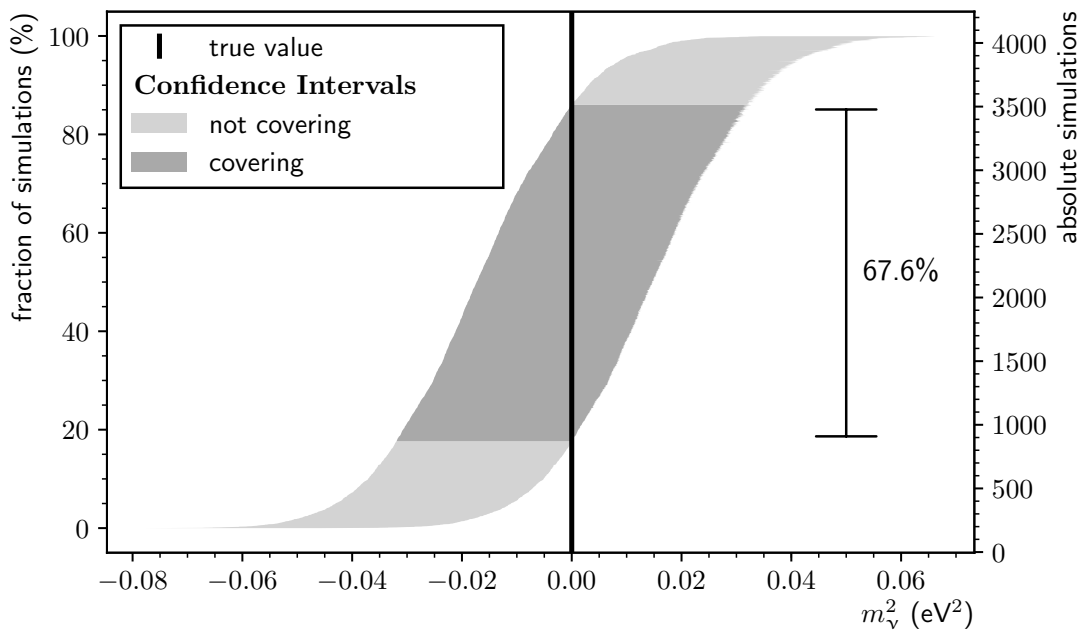


**Figure 6.4.: Test of coverage for the ensemble of confidence intervals obtained in the sensitivity study using the KARTRIN energy loss model.** The graph illustrates the coverage probability. An ensemble of 4046 KATRIN neutrino mass measurements with a true neutrino mass of 0 eV was simulated. For each simulated measurement a confidence interval was constructed using the profile-likelihood method. The obtained confidence intervals were sorted by their lower limit and plotted stacked which yields the gray band. The confidence intervals that cover the true value are depicted in dark gray, while the ones that do not cover the true value are depicted in light gray. In total 67.8 % coverage is obtained. In the limit of an infinite ensemble size a coverage of 68.2 % would be expected per construction. It should also be noted that there is little fluctuation in the width of the confidence intervals, which hints at the representative qualities of an Asimov data set.

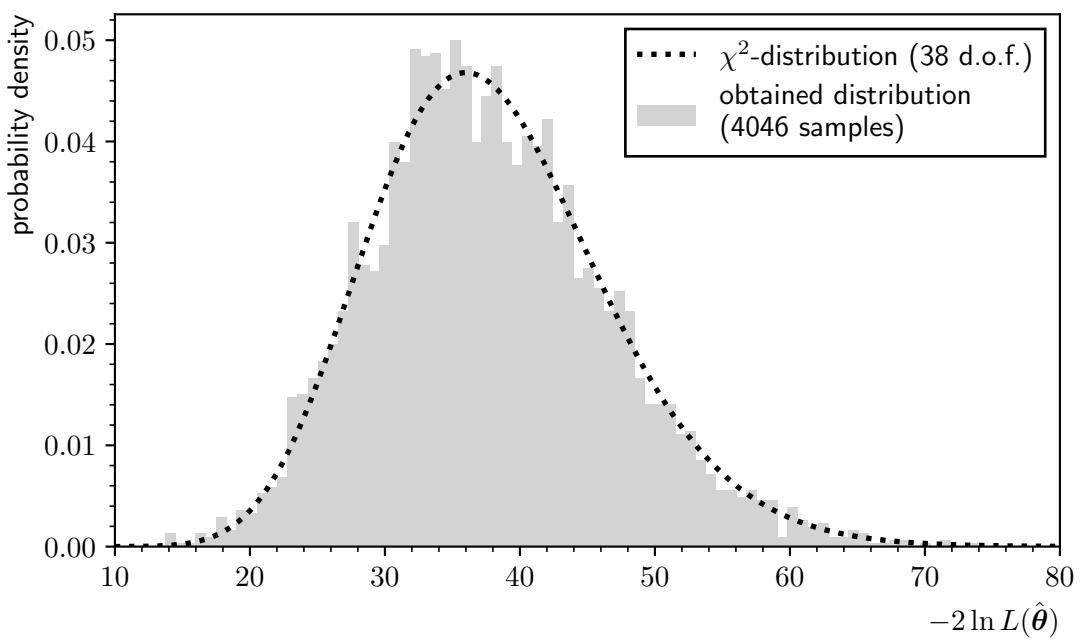


**Figure 6.5.: Chi-square distribution for the simulated ensemble of neutrino mass measurements obtained in the sensitivity study using the KATRIN energy loss model.** An ensemble of 4046 KATRIN neutrino mass measurements was simulated. The histogram shows the obtained distribution of the likelihood  $L$  evaluated at the MLE  $\hat{\theta}$ . The obtained distribution may follow a chi-square distribution with 38 degrees of freedom. For details the reader is referred to the main text.

## 6.6. Conclusion and Outlook

A general statistical framework was developed that enables the incorporation of model uncertainties into parameter inference within a frequentist context. It was used to show that the uncertainties of the KATRIN energy loss model at its current preliminary stage are negligible within neutrino mass interference. Furthermore, it was shown, that Asimov data sets of the presented kind may reasonably be assumed to be representative for an ensemble of neutrino mass measurements. Also, it was shown, that precautions have to be taken, when using the chi-square statistic as a measure for goodness-of-fit at the same time as incorporating “pull terms”.

The paragraphs below present possible follow-up studies as an outlook:

It is recommended to repeat this study once the KATRIN energy loss model is available in its final version and also available for electrons scattering off tritium.

Also, a general routine may be established that derives a test statistic for the goodness-of-fit from simulated ensembles where the chi-square statistic may not hold.

Furthermore, it would be of interest to develop a software framework that can treat a KATRIN electron gun measurement in combination with a KATRIN neutrino mass measurement in order for the presented “pull term”-approximation to become obsolete.

For practicality, it should be investigated whether really the full 15-parameter set is needed to describe the uncertainties of the KATRIN energy loss model or if the nine parameters of the model itself are sufficient.

The presented study investigates the sensitivity on the neutrino mass given an energy loss model. It may be of interest to invert this dependency and deduce a measurement plan for the KATRIN energy loss model given KATRIN’s envisaged design sensitivity.



## **7. Conclusions and Outlook**



# Appendix

## A. Energy-Dependent Model of the Probability for Electron Scattering within the WGTS

Section 5.2 introduces a model for the probability of electron scattering within the WGTS using the Poisson distribution. As explained, depending on the required accuracy, the conditions for using a Poisson distribution might be violated. Section A.1 introduces a model beyond the description via a Poisson distribution. Its evaluation was done numerically which demanded a trade-off between accuracy and run time. The latter is assessed in section A.2.

### A.1. Modeling

In the following, a model for the probability of electron scattering within the WGTS that depends on the electrons energy is derived. The difficulty lies in the fact, that an electron that scatters loses energy and hence its probability to scatter a second time is different from the first time. The presented model is inspired by a model given in [Gro15], that treats a similar effect for a change of an electron's pitch angles due to scattering.

The aim is to derive an expression  $\bar{P}_l^*(E_S)$  that denotes the probability of  $l$ -fold scattering for a  $\beta$  electron with a starting energy  $E_S$  averaged over all starting positions and pitch angles assuming a fixed energy loss  $\epsilon$  per scattering.

The expected amount of scatterings for a  $\beta$  electron when traveling through the whole WGTS volume of length  $d$  filled with a gas of constant density  $\rho$  is (see equation 3.17)

$$\mu(E, \theta_S) = \frac{\sigma(E)\rho d}{\cos \theta_S}, \quad (\text{A.1})$$

where  $E$  denotes the electron's kinetic energy;  $\theta_S$  the starting pitch angle; and  $\sigma(E)$  the energy dependent scattering cross section.

In the developed model, the volume of the WGTS is divided into  $N$  slices of equal width  $w = L/N$ .  $N$  is chosen sufficiently large that the probability for a  $\beta$  electron to scatter twice within one slice is essentially zero. Then, for large  $N$  the probability to scatter within one slice is  $\mu(E, \theta_S)/N$ . The probability not to scatter within  $n \leq N$  slices is

$$p_0(E, \theta_S, n) = \left(1 - \frac{\mu(E, \theta_S)}{N}\right)^n. \quad (\text{A.2})$$

Using the well known limit for the Euler constant, one obtains for  $n = N$  and  $N \rightarrow \infty$  that  $p_0$  is a Poisson distribution with expectation  $\mu$  evaluated at 0

$$\lim_{N \rightarrow \infty} p_0(E, \theta_S, N) = \lim_{N \rightarrow \infty} \left(1 - \frac{\mu(E, \theta_S)}{N}\right)^N = e^{-\mu(E, \theta_S)}. \quad (\text{A.3})$$

In other words, for no scattering, the Poisson model for the scattering probabilities as described in section 5.2 is recovered.

Assuming a constant energy loss per scattering of  $\epsilon$  the probability to scatter  $l$  times within  $n < N$  slices can be expressed recursively

$$p_l(E, \theta_S, n) = \underbrace{\sum_{k=l}^n}_{(4)} \underbrace{p_{l-1}(E, \theta_S, k-1)}_{(1)} \underbrace{(1 - p_0(E - (l-1)\epsilon, \theta_S, 1))}_{(2)} \underbrace{p_0(E - l\epsilon, \theta_S, n-k)}_{(3)}. \quad (\text{A.4})$$

The idea behind this expression is the following: One imagines an electron with an energy  $E$  that travels through  $n$  WGTS slices, scatters  $l$  times in total and once in the  $k$ th slice. Hence, it must have scattered  $l-1$  times in the  $k-1$  slices and must not scatter in the  $n-k$  slices to follow. In that regard, the above terms have the following meaning:

- (1) Probability to scatter  $l-1$  times within  $k-1$  slices with a kinetic energy of  $E$ .
- (2) Probability to scatter once within the  $k$ th slice with a kinetic energy of  $E - (l-1)\epsilon$ .
- (3) Probability not to scatter within the remaining  $N-k$  slices.
- (4) Sum over all slices  $k$  where the electron could scatter the last time. The sum starts at  $l$  because the probability to scatter  $l-1$  times within less than  $k=l-1$  slices (term (1)) is 0 because of the made assumption, that in the limit of large amount of slices  $N$  an electron does not scatter twice within one very narrow slice.

The probability to scatter  $l$  times can be averaged over all starting positions

$$\bar{p}_l(E, \theta_S) = \frac{1}{N} \sum_{n_S=1}^N p_l(E, \theta_S, n_S) \approx \frac{1}{d} \int_0^d p_l(E, \theta_S, \left\lceil N \frac{z_S}{d} \right\rceil) dz_S. \quad (\text{A.5})$$

Here, the averaging sum is approximated by an integral as this helps cutting down on run time in a numerical evaluation. This is due to the fact, that in a numerical evaluation a large number  $N$  ( $\sim 10^5$ ) of slices has to be chosen and the sum would have many terms. However, a numerical integration can achieve an accurate result with a smaller set of supporting points (see subsequent section A.2).

In the formal expression, the limit  $N \rightarrow \infty$  can be applied

$$P_l^*(E_S, \theta_S) = \lim_{N \rightarrow \infty} \bar{p}_l(E_S, \theta_S) \quad (\text{A.6})$$

$P_l^*(E_S, \theta_S)$  denotes the probability for a  $\beta$  electron to scatter  $l$  times when traveling through the whole WGTS with a starting energy  $E_S$  and pitch angle  $\theta_S$  averaged over all starting positions. Finally, this expression can be averaged over all starting pitch angles in order to obtain the energy dependent scattering probabilities

$$\bar{P}_l^*(E_S) = \frac{1}{1 - \cos \theta_{\max}} \int_0^{\theta_{\max}} \sin \theta_S P_l^*(E_S, \theta_S) d\theta_S. \quad (\text{A.7})$$

$\bar{P}_l^*(E_S)$  denotes the probability of  $l$ -fold scattering for a  $\beta$  electron with a starting energy  $E_S$  averaged over all starting positions and pitch angles assuming a fixed energy loss  $\epsilon$  per scattering. To derive such an expression was the aim of this section.

## A.2. Numerical Evaluation and Cross-Check

The energy-dependent probability  $\bar{P}_l^*$  for electrons to scatter  $l$ -fold (extended model) in equation (A.7) was evaluated numerically. Taking the limit  $N \rightarrow \infty$  in equation (A.6) was replaced by choosing a large  $N$ . The averaging integral over the starting positions in equation (A.5) and starting pitch angles in equation (A.7) was computed using Gaussian

quadrature. The extended model was introduced because the preconditions to model the scattering probabilities via a Poisson distribution (Poisson model) do not hold. Hence, the numerical evaluation of the extended model must be sufficiently accurate to show the difference to the Poisson model. How accurate this is, can not be known beforehand and was found out by trial and error. Both,  $N$  and the order of Gaussian quadrature, should be chosen as low as possible to cut down on run time, but sufficiently high for the required accuracy.

Also, a benchmark had to be found, to determine the accuracy of the numerical evaluation. The following idea was used: For an energy loss of  $\epsilon = 0 \text{ eV}$  per scattering, the extended model must recover the Poisson model exactly. This can be used to estimate the numerical accuracy in dependence of the number  $N$  of slices and order of Gaussian quadrature. The estimated accuracy for  $\epsilon = 0 \text{ eV}$  was then assumed for  $\epsilon > 0 \text{ eV}$ . A further cross-check is to look at the convergence of the numerical evaluation with increasing  $N$  and an increasing order of the Gaussian quadrature.

The averaged probability for 1-fold scattering  $\bar{P}_1^*$  of the extended model, was evaluated for  $\epsilon = 0 \text{ eV}$ . The result in dependence of  $N$  and the order of the Gaussian quadrature is shown in the top row of figure A.1. It should recover the Poisson model. For  $N = 5 \times 10^5$  and using Gaussian quadrature of order 5, the Poisson model and the extended model differ less than  $3 \times 10^{-6}$ . Furthermore, the numerical calculation converges from below, which may be interpreted as a one-sided numerical inaccuracy. The calculations for  $\epsilon = 12.6 \text{ eV}$  are shown in the lower row of figure A.1. They also show convergence on the  $10^{-5}$  level. Conclusively, the results make it plausible to assume a one-sided numerical inaccuracy on the  $10^{-5}$  level for  $N = 10^5$  and using Gaussian quadrature of order 5 for the integrals.

The corresponding run time to compute  $\bar{P}_1^*$  is in  $\mathcal{O}(N)$  as it requires a sum over all  $N$  slices in equation A.4. The extended model is defined recursively and therefore, the run time for  $l$ -fold scattering is in  $\mathcal{O}(N^l)$ . Hence, computing the probability for two-fold scattering would take  $5 \times 10^5$  times as long as for one-fold scattering for the same  $10^{-5}$  accuracy. This was not yet found to be feasible.

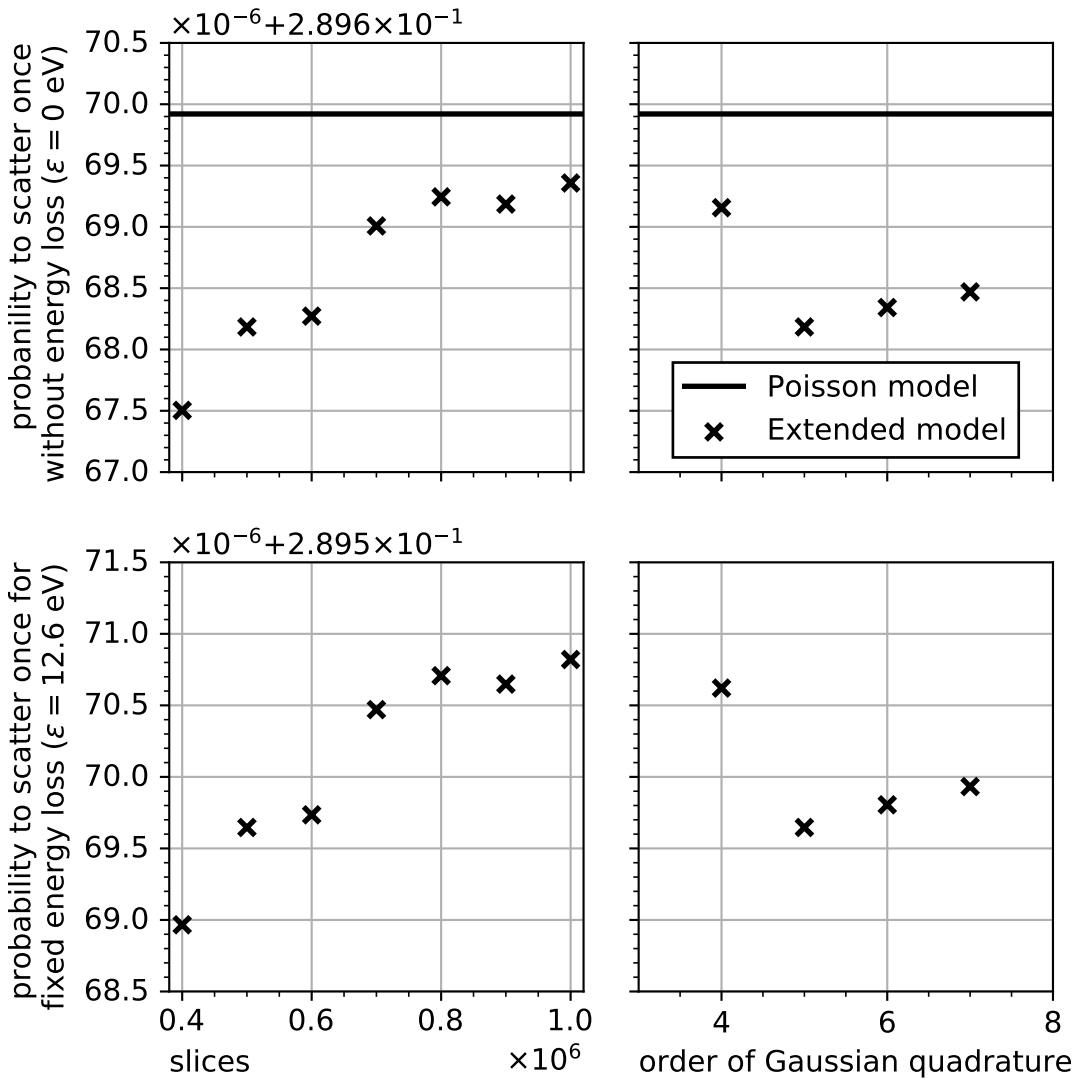


**Figure A.1.: Numerical accuracy of the extended model for the probability of electron scattering within the WGTS.** The extended model is given by (A.7). The Poisson model is given by equation (5.12). For both models the energy of the incident electrons was taken as 18 764.4 eV because for this energy, the Poisson model yields the values already given in table 5.1. The left column shows the dependence on the number  $N$  of slices of the WGTS. The right column shows the dependence on the order of Gaussian quadrature that was used to evaluate the two integrals in the extended model. The Poisson model is independent of these features and can be evaluated exactly. For the left column the order of Gaussian quadrature was fixed to 5. For the right column the number of slices was fixed to  $5 \times 10^5$ . The upper row shows the numerical evaluation of the extended model for no energy loss per scattering (markers). Its exact solution is given by the Poisson model (line). The lower row shows the model for an energy loss of 12.6 eV per scattering. These results make it plausible to assume a one-sided numerical inaccuracy on the  $10^{-5}$  level for  $N = 5 \times 10^5$  and using Gaussian quadrature of order 5 for the numerical evaluation of the extended model.

## B. Documentation of KaFit-Likelihood Extensions

Within this thesis the implementation of the likelihood in the KaFit framework was extended as described in section 6.4.1. The possibility was introduced to multiply the likelihood by different function types that resemble term (2) in equation (6.8).

KaFit is configured using an XML-like syntax. Example excerpts from KaFit-XML-configurations are given below. The documentation is given to a level that enables the usage by a user already familiar with KaFit. **[Double]** is used as a placeholder for a number; and **[Index\*]** for a parameter index. For example, the squared neutrino mass has the parameter index 0. A new **Penalty**-tag was introduced as sub-tag of the already established **LoglikelihoodKatrin**-tag:

```
<LoglikelihoodKatrin
    Name="myKatrinLogL" PDF="Gauss" RunSource="myRunGen"
    SpectrumSimulator="mySpecSim">
    <Penalty>
        <!-- Penalty Type -->
    </Penalty>
</LoglikelihoodKatrin>
```

`<!-- Penalty Type -->` can be substituted by one or more of the following tags:

### Multivariate Normal Distribution

The **Parameter**-tag represents a parameter the likelihood depends on. Its attribute **Mean** specifies the mean of a parameter; **Std** the standard deviation; and one or more **Correlation**-sub-tags the correlations between the parameters.

```
<MultivarNorm>
    <Parameter Index="[Index1]" Mean="[Double]" Std="[Double]" />
    <Parameter Index="[Index2]" Mean="[Double]" Std="[Double]" />
    <!-- ... -->
    <Correlation Index1="[Index1]" Index2="[Index2]" Value="[Double]" />
    <!-- ... -->
</MultivarNorm>
```

### One-Dimensional Gaussian Distribution

Analogously to the multivariate normal distribution, a one-dimensional Gaussian distribution can be used:

```
<Gaussian ParamIndex="[Index]" Mean="[Double]" Std="[Double]" />
```

### Uniform Neutrino Mass Prior

A constant prior on the neutrino mass in a Bayesian analysis can be set via the following tag:

```
<ConstInSqrt ParamIndex="0" />
```

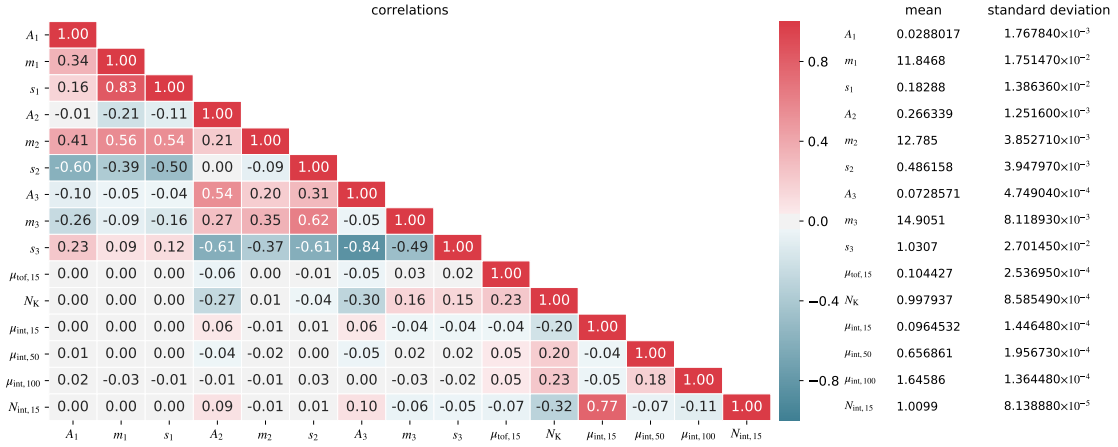
The former implementation within KaFit only allowed for a constant prior on the squared neutrino mass. The following lines derive the form of a prior on  $m_\nu^2$  that resembles a uniform prior on  $m_\nu$ . Let  $f(m_\nu) = C = \text{constant}$  be the prior on  $m_\nu$  and  $g(m_\nu^2)$  be the

prior on  $m_\nu^2$ . Starting from conservation of probability one derives

$$\begin{aligned} f(m_\nu) \mathrm{d}m_\nu &= g(m_\nu^2) \mathrm{d}m_\nu^2 \\ \Rightarrow g(m_\nu^2) &= f(m_\nu) \left( \frac{\mathrm{d}m_\nu^2}{\mathrm{d}m_\nu} \right)^{-1} \\ \Rightarrow g(m_\nu^2) &= C \frac{1}{2\sqrt{m_\nu^2}}. \end{aligned}$$

### C. Parameter Values of the Preliminary KATRIN Energy Loss Model

The best-fit values, standard deviations and correlations of the fit parameters for the KATRIN model for the energy loss of electrons scattering off deuterium molecules as used in this thesis are listed below [Pre-Han19-1]. The parameter names follow section 6.2. The parameters that actually enter into the KATRIN energy loss are the first nine from  $A_1$  to  $s_3$ . Their uncertainties are derived using the HESSE algorithm [S-MIN] of the MINUIT2 software package.



## D. Configuration of the Sensitivity Study using the Empirical KATRIN Energy Loss Model

Listed below, one finds the configuration of the SSC and KaFit modules as used in the sensitivity study in chapter 6.

---

### WGTS

---

gas column density	$5 \times 10^{21}$ molecules/m <sup>2</sup> (constant, no density profile)
slices	1
length	10.082 m
tritium purity	95 %

---

### Differential Spectrum

---

final molecular states	by Saenz, emulating Doppler effect
theo. corrections	screening, radiation (reference energy: molecular final states)
Fermi function	approximately relativistic
endpoint energy	18 575 eV
squared neutrino mass	0 eV

---

### Energy Loss

---

energy loss function	KATRIN or Aseev model
inel. scattering cross section	$3.456 \times 10^{-22}$ m <sup>2</sup>
elas. scattering	neglected

---

### Transmission Function

---

general configuration	relativistic, not detailed
mag. field in analyzing plane	$3 \times 10^{-4}$ T
mag. field of pinch magnet	6 T
mag. field in WGTS	3.6 T

---

### Detector

---

efficiency	95 %
------------	------

---

### MTD

---

voltages	reference MTD from the KATRIN Design Report
range	$[E_0 - 30 \text{ eV}, E_0 + 5 \text{ eV}]$
duration	3 years

---



# Acronyms

**BIXS** beta-induced X-ray spectroscopy.

**CKrS** condensed  $^{83m}\text{Kr}$  source.

**CPS** cryogenic pumping section.

**DPS** differential pumping section.

**EMCS** Earth magnetic field compensation system.

**FBM** forward beam monitor.

**FPD** focal plane detector.

**FT** KATRIN First Tritium measurement campaign.

**KNM1** KATRIN neutrino mass measurement campaign 1.

**LARA** laser Raman system.

**LEP** Large Electron Positron Collider.

**LFCS** low-field correction system.

**MAC-E** magnetic adiabatic collimation with electrostatic filtering.

**MLE** maximum likelihood estimator.

**MTD** measurement time distribution.

**PULCINELLA** precision ultra-low current integrating normalization electrometer for low-level analysis.

**RMMS** radial magnetic measuring system.

**RS** rear section.

**SDS** spectrometer and detector section.

**SM** Standard Model of Particle Physics.

**SSC** source and spectrum calculation.

**SSM** standard solar model.

**STS** source and transport section.

**TLK** Tritium Laboratory Karlsruhe.

**VMMS** vertical magnetic measuring system.

**WGTS** windowless gaseous tritium source.

# Bibliography

## References

- [Abd+09] J. N. Abdurashitov et al. “Measurement of the solar neutrino capture rate with gallium metal. III. Results for the 2002–2007 data-taking period”. *Phys. Rev. C* **80**.1 (2009), 015807. DOI: [10.1103/PhysRevC.80.015807](https://doi.org/10.1103/PhysRevC.80.015807).
- [Abd+17] D. N. Abdurashitov et al. “Electron scattering on hydrogen and deuterium molecules at 14–25 keV by the ‘Troitsk nu-mass’ experiment”. *Phys. Part. Nuclei Lett.* **14**.6 (2017), 892–899. DOI: [10.1134/S1547477117060024](https://doi.org/10.1134/S1547477117060024).
- [Abe+16] Y. Abe et al. “Measurement of  $\theta_{13}$  in Double Chooz using neutron captures on hydrogen with novel background rejection techniques”. *J. High Energ. Phys.* **2016**, 163 (2016), 163. DOI: [10.1007/JHEP01\(2016\)163](https://doi.org/10.1007/JHEP01(2016)163).
- [Acc+98] M. Acciarri et al. “Determination of the number of light neutrino species from single photon production at LEP”. *Phys. Lett.* **431**.1 (1998), 199–208. DOI: [10.1016/0370-2693\(89\)90704-1](https://doi.org/10.1016/0370-2693(89)90704-1).
- [Agh+18] N. Aghanim et al. “Planck 2018 results. VI. Cosmological parameters”. (2018). arXiv: [1807.06209 \[astro-ph.CO\]](https://arxiv.org/abs/1807.06209).
- [Ago+18] M. Agostini et al. “Improved limit on neutrinoless double- $\beta$  decay of  $^{76}\text{Ge}$  from GERDA phase II”. *Phys. Rev. Lett.* **120**.13 (2018), 132503. DOI: [10.1103/PhysRevLett.120.132503](https://doi.org/10.1103/PhysRevLett.120.132503).
- [Agu+09] A. A. Aguilar-Arevalo et al. “The MiniBooNE detector”. *Nucl. Instrum. Meth. A* **599**.1 (2009), 28–46. DOI: [doi.org/10.1016/j.nima.2008.10.028](https://doi.org/10.1016/j.nima.2008.10.028).
- [Aha+13] B. Aharmim et al. “Combined analysis of all three phases of solar neutrino data from the Sudbury Neutrino Observatory”. *Phys. Rev. C* **88**.2 (2013), 025501. DOI: [10.1103/PhysRevC.88.025501](https://doi.org/10.1103/PhysRevC.88.025501).
- [Alt+05] M. Altmann et al. “Complete results for five years of GNO solar neutrino observations”. *Phys. Lett. B* **616**.3 (2005), 174–190. DOI: [doi.org/10.1016/j.physletb.2005.04.068](https://doi.org/10.1016/j.physletb.2005.04.068).
- [Ams+15] J. Amsbaugh et al. “Focal-plane detector system for the KATRIN experiment”. *Nucl. Instrum. Methods Phys. Res. A* **778** (2015), 40–60. ISSN: 0168-9002. DOI: [10.1016/j.nima.2014.12.116](https://doi.org/10.1016/j.nima.2014.12.116).
- [Are+16] M. Arenz et al. “Commissioning of the vacuum system of the KATRIN main spectrometer”. *J. Instrum.* **11**.04 (2016), P04011. DOI: [10.1088/1748-0221/11/04/p04011](https://doi.org/10.1088/1748-0221/11/04/p04011).
- [Are+18a] M. Arenz et al. “First transmission of electrons and ions through the KATRIN beamline”. *J. Instrum.* **13**.04 (2018), P04020–P04020. DOI: [10.1088/1748-0221/13/04/p04020](https://doi.org/10.1088/1748-0221/13/04/p04020).

- [Are+18b] M. Arenz et al. “The KATRIN superconducting magnets: overview and first performance results”. *J. Instrum.* **13**.08 (2018), T08005. DOI: 10.1088/1748-0221/13/08/t08005.
- [Ase+00] V. Aseev et al. “Energy loss of 18 keV electrons in gaseous T and quench condensed D films”. *Eur. Phys. J. D* **10**.1 (2000), 39–52. DOI: 10.1007/s100530050525.
- [Ase+11] V. N. Aseev et al. “An upper limit on electron antineutrino mass from Troitsk experiment”. *Phys. Rev. D* **84** (2011), 112003. DOI: 10.1103/PhysRevD.84.112003.
- [Ass+96] K. Assamagan et al. “Upper limit of the muon-neutrino mass and charged-pion mass from momentum analysis of a surface muon beam”. *Phys. Rev. D* **53**.11 (1996), 6065–6077. DOI: 10.1103/PhysRevD.53.6065.
- [Bab+12] M. Babutzka et al. “Monitoring of the operating parameters of the KATRIN windowless gaseous tritium source”. *New J. Phys.* **14**.10 (2012), 103046. DOI: 10.1088/1367-2630/14/10/103046.
- [Bab14] M. Babutzka. “Design and development for the rearsection of the KATRIN experiment”. PhD thesis. KIT (2014). DOI: 10.5445/IR/1000045598.
- [Bah96] J. N. Bahcall. “Solar neutrinos: Where we are, where we are going”. *Astrophys. J.* **467** (1996), 475. DOI: 10.1086/177624.
- [Bar+98] R. Barate et al. “An upper limit on the tau-neutrino mass from three-prong and five-prong tau decays”. *Eur. Phys. J. C* **2** (1998), 395–406. DOI: 10.1007/s100520050149.
- [Bau14] S. Bauer. “Energy calibration and stability monitoring of the KATRIN experiment”. PhD thesis. WWU (2014). URL: <https://miami.uni-muenster.de/Record/da3d6759-9202-4b68-bb80-711f52b208d8>.
- [BC38] H. A. Bethe and C. L. Critchfield. “The formation of deuterons by proton combination”. *Phys. Rev.* **54**.4 (1938), 248–254. DOI: 10.1103/PhysRev.54.248.
- [Bec00] H. Becquerel. “Contribution à l’étude du rayonnement du radium”. *J. Phys. Theor. Appl.* **9**.1 (1900), 190–199.
- [Bec95] H. Becquerel. “Sur les Radiations Invisibles Émises par les Corps Phosphorescents”. *C. R. Acad. Sci.* **122** (1895), 501–503.
- [Bet39] H. A. Bethe. “Energy production in stars”. *Phys. Rev.* **55**.5 (1939), 434–456. DOI: 10.1103/PhysRev.55.434.
- [Boh32] N. Bohr. “Faraday lecture. Chemistry and the quantum theory of atomic constitution”. *J. Chem. Soc.* 0 (1932), 349–384. DOI: 10.1039/JR9320000349.
- [Bon+99] J. Bonn et al. “A high resolution electrostatic time-of-flight spectrometer with adiabatic magnetic collimation”. *Nucl. Instrum. Methods Phys. Res.* **421**.1 (1999), 256–265. DOI: 10.1016/S0168-9002(98)01263-7.
- [BPB01] J. N. Bahcall, M. H. Pinsonneault, and S. Basu. “Solar models: current epoch and time dependences, neutrinos, and helioseismological properties”. *Astrophys. J.* **555**.2 (2001), 990–1012. DOI: 10.1086/321493.
- [BPR15] L. I. Bodine, D. S. Parno, and R. G. H. Robertson. “Assessment of molecular effects on neutrino mass measurements from tritium  $\beta$  decay”. *Phys. Rev. C* **91**.3 (2015), 035505. DOI: 10.1103/PhysRevC.91.035505.

- [BPT80] G. Beamson, H. Q. Porter, and D. W. Turner. “The collimating and magnifying properties of a superconducting field photoelectron spectrometer”. *J. Phys. E* **13**.1 (1980), 64–66. DOI: [10.1088/0022-3735/13/1/018](https://doi.org/10.1088/0022-3735/13/1/018).
- [Cha14] J. Chadwick. “Intensitätsverteilung im magnetischen Spectrum der  $\beta$ -Strahlen von Radium B + C”. *Verhandl. Dtsch. Phys. Ges.* **16** (1914), 383.
- [Cle+98] B. T. Cleveland et al. “Measurement of the solar electron neutrino flux with the Homestake chlorine detector”. *Astrophys. J.* **496** (1998), 505–526. DOI: [10.1086/305343](https://doi.org/10.1086/305343).
- [Cow+11] G. Cowan et al. “Asymptotic formulae for likelihood-based tests of new physics”. *Eur. Phys. J. C* **71** (2011), 1554. DOI: [10.1140/epjc/s10052-011-1554-0](https://doi.org/10.1140/epjc/s10052-011-1554-0).
- [Cow+56] C. L. Cowan et al. “Detection of the free neutrino: a confirmation”. *Science* **124**.3212 (1956), 103–104. DOI: [10.1126/science.124.3212.103](https://doi.org/10.1126/science.124.3212.103).
- [Dan+62] G. Danby et al. “Observation of high-energy neutrino reactions and the existence of two kinds of neutrinos”. *Phys. Rev. Lett.* **9** (1962), 36–44. DOI: [10.1103/PhysRevLett.9.36](https://doi.org/10.1103/PhysRevLett.9.36).
- [Dor+04] A. Doroshkevich et al. “Large scale structure in the SDSS galaxy survey”. *Astron. Astrophys.* **418** (2004), 7–23.
- [Dos+06] N. Doss et al. “Molecular effects in investigations of tritium molecule beta decay endpoint experiments”. *Phys. Rev. C* **73** (2006), 025502. DOI: [10.1103/PhysRevC.73.025502](https://doi.org/10.1103/PhysRevC.73.025502).
- [Dyb19] S. Dyba. “Background reduction by the inner wire electrode and set-up of the condensed krypton source at the neutrino mass experiment KATRIN”. PhD thesis. WWU (2019).
- [Ell+17] E. Ellinger et al. “Monitoring the KATRIN source properties within the beamline”. *J. Phys. Conf. Ser.* **888** (2017), 012229. DOI: [10.1088/1742-6596/888/1/012229](https://doi.org/10.1088/1742-6596/888/1/012229).
- [Ell19] E. Ellinger. “Development and investigation of the Forward Beam Monitor for the KATRIN experiment”. To be published. PhD thesis. Bergische Universität Wuppertal (2019).
- [Erh+14] M. Erhard et al. “High-voltage monitoring with a solenoid retarding spectrometer at the KATRIN experiment”. *J. Instrum.* **9**.06 (2014), P06022–P06022. DOI: [10.1088/1748-0221/9/06/p06022](https://doi.org/10.1088/1748-0221/9/06/p06022).
- [Erh+18] M. Erhard et al. “Technical design and commissioning of the KATRIN large-volume air coil system”. *J. Instrum.* **13**.02 (2018), P02003. DOI: [10.1088/1748-0221/13/02/p02003](https://doi.org/10.1088/1748-0221/13/02/p02003).
- [Est+19] I. Esteban et al. “Global analysis of three-flavour neutrino oscillations: synergies and tensions in the determination of  $\theta_{23}$ ,  $\delta_{\text{CP}}$ , and the mass ordering”. *J. High Energy Phys.* **2019**.1 (2019), 106. DOI: [10.1007/JHEP01\(2019\)106](https://doi.org/10.1007/JHEP01(2019)106).
- [EW27] C. D. Ellis and W. A. Wooster. “The average energy of disintegration of radium E”. *Proc. Royal Soc. Lond. A* **117** (1927), 109. DOI: [10.1098/rspa.1927.0168](https://doi.org/10.1098/rspa.1927.0168).
- [FC98] G. J. Feldman and R. D. Cousins. “Unified approach to the classical statistical analysis of small signals”. *Phys. Rev. D* **57**.7 (1998), 3873–3889. DOI: [10.1103/PhysRevD.57.3873](https://doi.org/10.1103/PhysRevD.57.3873).

- [Fer34] E. Fermi. “Versuch einer Theorie der  $\beta$ -Strahlen”. *Z. Phys.* **88**.3 (1934), 161–177. DOI: [10.1007/BF01351864](https://doi.org/10.1007/BF01351864).
- [Frä10] F. M. Fränkle. “Background investigations of the KATRIN pre-spectrometer”. PhD thesis. KIT (2010). DOI: [10.5445/IR/1000019392](https://doi.org/10.5445/IR/1000019392).
- [Fuk+98] Y. Fukuda et al. “Evidence for oscillation of atmospheric neutrinos”. *Phys. Rev. Lett.* **81** (1998), 1562–1567. DOI: [10.1103/PhysRevLett.81.1562](https://doi.org/10.1103/PhysRevLett.81.1562).
- [Gan+16] A. Gando et al. “Search for Majorana neutrinos near the inverted mass hierarchy region with KamLAND-Zen”. *Phys. Rev. Lett.* **117**.8 (2016), 082503. DOI: [10.1103/PhysRevLett.117.082503](https://doi.org/10.1103/PhysRevLett.117.082503).
- [Ger75] D. E. Gerhart. “Comprehensive optical and collision data for radiation action. I. H<sub>2</sub>”. *J. Chem. Phys.* **62**.3 (1975), 821–832. DOI: [10.1063/1.430533](https://doi.org/10.1063/1.430533).
- [Gla61] S. L. Glashow. “Partial symmetries of weak interactions”. *Nucl. Phys.* **22** (1961), 579–588. DOI: [10.1016/0029-5582\(61\)90469-2](https://doi.org/10.1016/0029-5582(61)90469-2).
- [Gol+58] M. Goldhaber et al. “Helicity of neutrinos”. *Phys. Rev.* **109**.3 (1958), 1015–1017. DOI: [10.1103/PhysRev.109.1015](https://doi.org/10.1103/PhysRev.109.1015).
- [Gro+08] S. Grohmann et al. “Cryogenic design of the KATRIN source cryostat”. *AIP Conf. Proc.* **985**.1 (2008), 1277–1284. DOI: [10.1063/1.2908483](https://doi.org/10.1063/1.2908483).
- [Gro15] S. Groh. “Modeling of the response function and measurement of transmission properties of the KATRIN experiment”. PhD thesis. KIT (2015). DOI: [10.5445/IR/1000046546](https://doi.org/10.5445/IR/1000046546).
- [Har15] F. T. Harms. “Characterization and minimization of background processes in the KATRIN main spectrometer”. PhD thesis. KIT (2015). DOI: [10.5445/IR/1000050027](https://doi.org/10.5445/IR/1000050027).
- [Hig64] P. W. Higgs. “Broken symmetries and the masses of gauge bosons”. *Phys. Rev. Lett.* **13** (1964), 508–509. DOI: [10.1103/PhysRevLett.13.508](https://doi.org/10.1103/PhysRevLett.13.508).
- [Höt12] M. Hötzl. “Simulation and analysis of source-related effects for KATRIN”. PhD thesis. KIT (2012). DOI: [10.5445/IR/1000031259](https://doi.org/10.5445/IR/1000031259).
- [Jac75] J. Jackson. “Classical electrodynamics”. Wiley, Hoboken, 1975. ISBN: 9780471431329.
- [Jan15] A. Jansen. “The cryogenic pumping section of the KATRIN experiment - design studies and experiments for the commissioning”. PhD thesis. KIT (2015). DOI: [10.5445/IR/1000047146](https://doi.org/10.5445/IR/1000047146).
- [Käf12] W. Käfer. “Sensitivity studies for the KATRIN experiment”. PhD thesis. KIT (2012). DOI: [10.5445/IR/1000026021](https://doi.org/10.5445/IR/1000026021).
- [KAT05] J. Angrik et al. “KATRIN design report 2004”. *Wissenschaftliche Berichte / Forschungszentrum Karlsruhe* **7090** (2005).
- [Kir98] T. Kirsten. “GALLEX solar neutrino results”. *Prog. Part. Nucl. Phys.* **40** (1998), 85–99. DOI: [doi.org/10.1016/S0146-6410\(98\)00013-1](https://doi.org/10.1016/S0146-6410(98)00013-1).
- [Kle+19] M. Kleesiek et al. “ $\beta$ -decay spectrum, response function and statistical model for neutrino mass measurements with the KATRIN experiment”. *Eur. Phys. J. C* **79**.3 (2019), 204. DOI: [10.1140/epjc/s10052-019-6686-7](https://doi.org/10.1140/epjc/s10052-019-6686-7).
- [Kle14] M. Kleesiek. “A data-analysis and sensitivity-optimization framework for the KATRIN experiment”. PhD thesis. KIT (2014). DOI: [10.5445/IR/1000043301](https://doi.org/10.5445/IR/1000043301).

- [Klein19] M. Klein. “Tritium ions in KATRIN: blocking, removal and detection”. PhD thesis. KIT (2019). DOI: [10.5445/IR/1000093526](https://doi.org/10.5445/IR/1000093526).
- [Kod+01] K. Kodama et al. “Observation of tau neutrino interactions”. *Phys. Lett. B* **504** (2001), 218–224. DOI: [10.1016/S0370-2693\(01\)00307-0](https://doi.org/10.1016/S0370-2693(01)00307-0).
- [Kos12] A. Kosmider. “Tritium retention techniques in the KATRIN transport section and commissioning of its DPS2-F cryostat”. PhD thesis. KIT (2012). DOI: [10.5445/IR/1000028959](https://doi.org/10.5445/IR/1000028959).
- [KR94] Y.-K. Kim and M. E. Rudd. “Binary-encounter-dipole model for electron-impact ionization”. *Phys. Rev. A* **50** (5 1994), 3954–3967. DOI: [10.1103/PhysRevA.50.3954](https://doi.org/10.1103/PhysRevA.50.3954).
- [Kra+05] C. Kraus et al. “Final results from phase II of the Mainz neutrino mass search in tritium decay”. *Eur. Phys. J. C* **40** (2005), 447–468.
- [Kuc+18] L. Kuckert et al. “Modelling of gas dynamical properties of the KATRIN tritium source and implications for the neutrino mass measurement”. *Vacuum* **158** (2018), 195–205. DOI: [10.1016/j.vacuum.2018.09.036](https://doi.org/10.1016/j.vacuum.2018.09.036).
- [Kuc16] L. Kuckert. “The windowless gaseous tritium source of the KATRIN experiment - characterisation of gas dynamical and plasma properties”. PhD thesis. KIT (2016). DOI: [10.5445/IR/1000065077](https://doi.org/10.5445/IR/1000065077).
- [Let+18] J. Letnev et al. “Technical design and commissioning of a sensor net for fine-meshed measuring of the magnetic field at the KATRIN spectrometer”. *J. Instrum.* **13.08** (2018), T08010. DOI: [10.1088/1748-0221/13/08/t08010](https://doi.org/10.1088/1748-0221/13/08/t08010).
- [Liu73] J. W. Liu. “Total inelastic cross section for collisions of H<sub>2</sub> with fast charged particles”. *Phys. Rev. A* **7.1** (1973), 103–109. DOI: [10.1103/PhysRevA.7.103](https://doi.org/10.1103/PhysRevA.7.103).
- [Liu87] J. W. Liu. “Total cross sections for high-energy electron scattering by H<sub>2</sub> (<sup>1</sup>Σ<sub>g</sub><sup>+</sup>), N<sub>2</sub> (<sup>1</sup>Σ<sub>g</sub><sup>+</sup>), and O<sub>2</sub> (<sup>3</sup>Σ<sub>g</sub><sup>-</sup>)”. *Phys. Rev. A* **35.2** (1987), 591–597. DOI: [10.1103/PhysRevA.35.591](https://doi.org/10.1103/PhysRevA.35.591).
- [LL02] T. J. Loredo and D. Q. Lamb. “Bayesian analysis of neutrinos observed from supernova SN 1987A”. *Phys. Rev. D* **65.6** (2002), 063002. DOI: [10.1103/PhysRevD.65.063002](https://doi.org/10.1103/PhysRevD.65.063002).
- [LY56] T. D. Lee and C. N. Yang. “Question of parity conservation in weak interactions”. *Phys. Rev.* **104.1** (1956), 254–258. DOI: [10.1103/PhysRev.104.254](https://doi.org/10.1103/PhysRev.104.254).
- [Mer+19] S. Mertens et al. *J. Phys. G* **46.6** (2019), 065203. DOI: [10.1088/1361-6471/ab12fe](https://doi.org/10.1088/1361-6471/ab12fe).
- [MNS62] Z. Maki, M. Nakagawa, and S. Shoichi. “Remarks on the unified model of elementary particles”. *Progress of Theoretical Physics* **28.5** (1962), 870–880. DOI: [10.1143/PTP.28.870](https://doi.org/10.1143/PTP.28.870).
- [MS86] S. P. Mikheev and A. Y. Smirnov. “Resonant amplification of neutrino oscillations in matter and solar neutrino spectroscopy”. *Nuovo Cim. C* **9** (1986), 17–26. DOI: [10.1007/BF02508049](https://doi.org/10.1007/BF02508049).
- [Mye+15] E. G. Myers et al. “Atomic masses of tritium and helium-3”. *Phys. Rev. Lett.* **114.1** (2015), 013003. DOI: [10.1103/PhysRevLett.114.013003](https://doi.org/10.1103/PhysRevLett.114.013003).
- [Ney37] J. Neyman. “Outline of a theory of statistical estimation based on the classical theory of probability”. *Philos. Trans. Royal Soc. A* **236.767** (1937), 333–380.

- [Noe18] E. Noether. “Invarianten beliebiger Differentialausdrücke” (1918). In: “Nachrichten von der Gesellschaft der Wissenschaften zu Göttingen, Mathematisch-Physikalische Klasse”, 37–44.
- [OW08] E. W. Otten and C. Weinheimer. “Neutrino mass limit from tritium beta decay”. *Rep. Prog. Phys.* **71** (2008), 086201. DOI: [10.1088/0034-4885/71/8/086201](https://doi.org/10.1088/0034-4885/71/8/086201).
- [Pau30] W. Pauli. Published in: “Wissenschaftlicher Briefwechsel mit Bohr, Einstein, Heisenberg u.a. Band II: 1930–1939” by V.F. Weisskopff et al. (1985). Springer Berlin Heidelberg. 1930. ISBN: 9783540788010.
- [Pon58] B. Pontecorvo. “Inverse beta processes and nonconservation of lepton charge”. *Sov. Phys. JETP* **7** (1958), 172–173.
- [PSB15] F. Priester, M. Sturm, and B. Bornschein. “Commissioning and detailed results of KATRIN inner loop tritium processing system at Tritium Laboratory Karlsruhe”. *Vacuum* **116** (2015), 42–47. DOI: [10.1016/j.vacuum.2015.02.030](https://doi.org/10.1016/j.vacuum.2015.02.030).
- [Röll15] M. Röllig. “Tritium analytics by beta induced X-ray spectrometry”. PhD thesis. KIT (2015). DOI: [10.5445/IR/1000054050](https://doi.org/10.5445/IR/1000054050).
- [Röt19] C. Röttele. “Tritium suppression factor of the KATRIN transport section”. To be published. PhD thesis. KIT (2019).
- [Rut99] E. Rutherford. “VIII. Uranium radiation and the electrical conduction produced by it”. *The London, Edinburgh, and Dublin Philosophical Magazine and Journal of Science* **47**.284 (1899), 109–163. DOI: [10.1080/14786449908621245](https://doi.org/10.1080/14786449908621245).
- [Sal68] A. Salam. “Weak and electromagnetic interactions”. *Proceedings of the Eighth Nobel Symposium* (1968), 367–377.
- [Sch13] M. Schlosser. “Accurate calibration of the Raman system for the Karlsruhe Tritium Neutrino Experiment”. PhD thesis. KIT (2013). DOI: [10.5445/IR/1000034967](https://doi.org/10.5445/IR/1000034967).
- [Sch19] W. Schmitz. “Particles, Fields and Forces : A Conceptual Guide to Quantum Field Theory and the Standard Model”. 1st ed. Springer International Publishing, 2019. ISBN: 9783030128784.
- [Sei19] H. Seitz-Moskaliuk. “Characterisation of the KATRIN tritium source and evaluation of systematic effects”. PhD thesis. KIT (2019). DOI: [10.5445/IR/1000090748](https://doi.org/10.5445/IR/1000090748).
- [Shi+93] D. Shiner et al. “H<sub>2</sub>, D<sub>2</sub>, and HD ionization potentials by accurate calibration of several iodine lines”. *Phys. Rev. A* **47**.5 (1993), 4042–4045. DOI: [10.1103/PhysRevA.47.4042](https://doi.org/10.1103/PhysRevA.47.4042).
- [Sim81] J. J. Simpson. “Measurement of the  $\beta$ -energy spectrum of <sup>3</sup>H to determine the antineutrino mass”. *Phys. Rev. D* **23**.3 (1981), 649–662. DOI: [10.1103/PhysRevD.23.649](https://doi.org/10.1103/PhysRevD.23.649).
- [Tan+18] M. Tanabashi et al. “Review of particle physics”. *Phys. Rev. D* **98**.3 (2018), 030001. DOI: [10.1103/PhysRevD.98.030001](https://doi.org/10.1103/PhysRevD.98.030001).
- [Tho97] J. J. Thomson. “XL. Cathode rays”. *The London, Edinburgh, and Dublin Philosophical Magazine and Journal of Science* **44**.269 (1897), 293–316. DOI: [10.1080/14786449708621070](https://doi.org/10.1080/14786449708621070).
- [Thü+09] T. Thümmler et al. “Precision high voltage divider for the KATRIN experiment”. *New J. Phys.* **11**.10 (2009), 103007. DOI: [10.1088/1367-2630/11/10/103007](https://doi.org/10.1088/1367-2630/11/10/103007).

- [Ubi+09] M. Ubieto-Díaz et al. “A broad-band FT-ICR penning trap system for KATRIN”. *Int. J. Mass Spectrom.* **288**.1 (2009), 1–5. DOI: 10.1016/j.ijms.2009.07.003.
- [Val04] K. Valerius. “Elektromagnetisches Design für das Hauptspektrometer des KATRIN Experiments”. Diploma thesis. WWU (2004). URL: [https://www.uni-muenster.de/Physik.KP/AGWeinheimer/Files/theses/Diplom\\_Kathrin\\_Valerius.pdf](https://www.uni-muenster.de/Physik.KP/AGWeinheimer/Files/theses/Diplom_Kathrin_Valerius.pdf).
- [Val09] K. Valerius. “Spectrometer-related background processes and their suppression in the KATRIN experiment”. PhD thesis. WWU (2009). URL: <http://repositorium.uni-muenster.de/document/miami/93137705-73f4-404a-a438-09d487cbff63/>.
- [Wal44] A. Wald. “On cumulative sums of random variables”. *Ann. Math. Stat.* **15** (1944), 283–296.
- [Wei38] C. F. Weizäcker. “Über Elementumwandlungen im Innern der Sterne”. *Phys. Zeit.* **39**.633 (1938), 46.
- [Wei67] S. Weinberg. “A model of leptons”. *Phys. Rev. Lett.* **19**.21 (1967), 1264–1266. DOI: 10.1103/PhysRevLett.19.1264.
- [Wil38] S. S. Wilks. “The large-sample distribution of the likelihood ratio for testing composite hypotheses”. *Ann. Math. Statist.* **9**.1 (1938), 60–62. DOI: 10.1214/aoms/1177732360.
- [Wol78] L. Wolfenstein. “Neutrino oscillations in matter”. *Phys. Rev. D* **17** (1978), 2369–2374. DOI: 10.1103/PhysRevD.17.2369.
- [Wu+57] C. S. Wu et al. “Experimental test of parity conservation in beta decay”. *Phys. Rev.* **105**.4 (1957), 1413–1415. DOI: 10.1103/PhysRev.105.1413.
- [Yèc+17] C. Yèche et al. “Constraints on neutrino masses from Lyman-alpha forest power spectrum with BOSS and XQ-100”. *J. Cosmol. Astropart. Phys.* **1706**.06 (2017), 047. DOI: 10.1088/1475-7516/2017/06/047.
- [Zbo11] M. Zboril. “Feste Elektronenquellen für die Energieskalaüberwachung im KATRIN Experiment”. PhD thesis. WWU (2011). URL: [http://repositorium.uni-muenster.de/document/miami/79b74253-2dc4-493b-a08d-4eeb5a10b8c1/diss\\_zboril.pdf](http://repositorium.uni-muenster.de/document/miami/79b74253-2dc4-493b-a08d-4eeb5a10b8c1/diss_zboril.pdf).
- [Zee03] A. Zee. “Quantum Field Theory in a Nutshell”. Princeton University Press, Princeton, 2003. ISBN: 9780691010199.
- [ZJH12] S. Zhang, G. Ji, and J. Han. “The positional and angular distribution of molecules flowing through cylindrical tube in free molecular flow”. *Phys. Procedia* **32** (2012), 513–524. DOI: 10.1016/j.phpro.2012.03.595.
- [Zub11] K. Zuber. “Neutrino Physics”. 2nd ed. CRC Press, Boca Raton, 2011. ISBN: 9781420064711.

## Preliminary

- [Pre-Han19-1] V. Hannen et al. “Global fit of parametrized energy loss function to measured integral and t.o.f. data”. GIT-Repository, 2019. URL: [https://nuserv.uni-muenster.de:8443/afulst/KATRIN-eloss/blob/master/code/STS3a/global\\_eloss\\_fit-v10.ipynb](https://nuserv.uni-muenster.de:8443/afulst/KATRIN-eloss/blob/master/code/STS3a/global_eloss_fit-v10.ipynb).
- [Pre-Han19-2] V. Hannen. “New energy loss parametrization”. 36th KATRIN Collaboration Meeting, 2019. URL: <https://fuzzy.fzk.de/bscw/bscw.cgi/1254307>.

- [Pre-Rod19] C. Rodenbeck and R. Sack. “Measurement of KATRIN’s energy loss function using a time of flight method”. DPG-Frühjahrstagung, 2019. URL: <https://fuzzy.fzk.de/bscw/bscw.cgi/1256746>.

## Software

- [Ant+09] I. Antcheva et al. “ROOT — A C++ framework for petabyte data storage, statistical analysis and visualization”. *Comput. Phys. Commun.* **180**.12 (2009), 2499–2512. DOI: <https://doi.org/10.1016/j.cpc.2009.08.005>.
- [S-KAS] KATRIN collaboration. “KATRIN Analysis and Simulations Package (KASPER)”. 2019. URL: [userv.uni-muenster.de:8443/katrin-git/kasper](http://userv.uni-muenster.de:8443/katrin-git/kasper).
- [S-KF] M. Kleesiek et al. “KaFit”. Based on [Kle19+; Kle14] and others, URL: [userv.uni-muenster.de:8443/katrin-git/kasper](http://userv.uni-muenster.de:8443/katrin-git/kasper).
- [S-MIN] F. James. “MINUIT: Function Minimization and Error Analysis Reference Manual” (1998). CERN Program Library Long Writeups. URL: <https://cds.cern.ch/record/2296388>.
- [S-SSC] KATRIN collaboration. “Source and spectrum calculation (SSC)”. Based on [Kle19+; Kle14; Höt12; Gro15; Käf12] and others, URL: [userv.uni-muenster.de:8443/katrin-git/kasper](http://userv.uni-muenster.de:8443/katrin-git/kasper).